The Charm Cross Section and Atomic Number Dependence in π^-N Collisions

by

Colin W. Gay

A Thesis submitted in conformity with the requirements
for the Degree of Doctor of Philosophy in the
University of Toronto

Abstract

Using the Tagged Photon Spectrometer at Fermi National Accelerator Lab. the fixed-target experiment E769 collected 370 M events induced by a 250 GeV hadron beam. The beam consisted of pions. kaons. and protons: 150 M of the events were taken with a negative beam. and 220 M with a positive beam. The target was comprised of 26 foils of four materials — Beryllium. Aluminum. Copper. and Tungsten. Signals in the decay modes $D^+ \rightarrow K^-\pi^+\pi^+$ and $D^0 \rightarrow K^-\pi^+$ [1] were used to determine the atomic number (A) dependence of charm production. as well as the total charm cross section. for incident π^-'s. The A-dependence exponent was measured to be $\alpha_- = 1.02 \pm 0.06 \pm 0.02$. With this value of α_-. the charm cross section for a single nucleon target was measured to be $15.2 \pm 3.5 \pm 2.0$ μb. Using next-to-leading order cross section calculations. the charm quark mass was determined to be 1.48 ± 0.15(exper.) ± 0.2(theor.) GeV.

[1] Throughout the thesis. the charge conjugate states are implicitly included

Contents

List of Figures

List of Tables

Chapter 1

Introduction

This thesis presents a measurement of the total charm quark cross section in $\pi^- N$ collisions. Recently, new predictions for the value of this cross section have been made using perturbative Quantum Chromodynamics (QCD). Before presenting these predictions, we briefly review the evidence for the existence of the charm quark and the colour charge of QCD. Also, the current experimental status of charm hadroproduction is described.

1.1 Historical Background

In 1947, there were six known fundamental particles: the electron and proton, the neutron (discovered in 1932 by Chadwick [Cha 32]), the positron (discovered in 1933 by Anderson [And 33]), and two muons (μ^+ and μ^-, discovered in 1937 by Street and Stevenson [Str 37]). There were two well understood forces known, gravity and electromagnetism, as well as the less understood weak force, which is responsible for beta decay. Furthermore, it was clear that a fourth force (now called the strong force), responsible for the binding of nucleons into nuclei, must exist, though its nature was relatively unknown. However, in 1947, the observation of the pion by Lattes *et al.* [Lat 47] began a period which saw a seemingly endless rise in the number of known particles. These particles were classified into two main groups, according to which interactions they experience.

The *leptons* consist of all particles which do not interact via the strong force. These include the electron and positron, the muons and the taus (discovered in 1975 [Per 75]), as well as the accompanying neutrinos. The electron neutrino was first observed in 1953 [Cow 53] and the muon neutrino in 1962 [Dan 62]. The tau neutrino has not yet been directly observed.

Most of the new particles observed were *hadrons* (strongly interacting particles), some with half-integral angular momentum (baryons) and some with integral angular momentum (mesons).

1.2 The Invention and Discovery of Quarks

After over a decade of cataloguing the properties of these new hadrons, patterns began to appear. For example, the mesons seemed to divide up into singlets and octets with similar quantum numbers and masses. The baryons divided into singlets, octets and decimets. The quark model was first proposed in 1964 by Gell-Mann [Gel 64] and Zweig [Zwe 64], mostly as a means of keeping track of this multiplet structure. The idea was that hadrons could be considered to comprise some combination of 3 spin 1/2 particles (quarks) and their antiparticles (antiquarks). The 3 quarks formed an SU(3) triplet, and the 3 antiquarks would transform according to the complex conjugate $\mathbf{3}^*$ representation. Mesons were considered to be $q\bar{q}$ pairs and hence divide up as $\mathbf{3} \otimes \mathbf{3}^* = \mathbf{1} \oplus \mathbf{8}$. Baryons would be made up of three quarks, qqq, or three antiquarks, $\bar{q}\bar{q}\bar{q}$, and thus naturally divide up as $\mathbf{3} \otimes \mathbf{3} \otimes \mathbf{3} = \mathbf{1} \oplus \mathbf{8} \oplus \mathbf{8} \oplus \mathbf{10}$, as observed. The 3 quarks were called up, down and strange. Later that year, Bjorken and others [Bjo 64] postulated the existence of a larger symmetry, SU(4), which required a fourth quark that they called charm.

In 1970, Glashow, Iliopoulos, and Maiani (GIM) [Gla 70] revived the charm quark idea as a way to explain the low $K_L \rightarrow \mu^+\mu^-$ branching ratio. The three quark model contains a (left-handed) weak isospin doublet:

$$\psi_1 = \begin{pmatrix} u \\ d_c \end{pmatrix},$$

where $d_c = d\cos\theta_c + s\sin\theta_c$, as well as a left-handed strange quark, and the right-handed singlets u_r, d_r, and s_r. θ_c is the Cabbibo angle ([Cab 63]), introduced because the weak eigenstates are not flavour eigenstates. If the Weak Lagrangian (used to calculate decay rates) is invariant under weak isospin rotations, there must be a neutral current of the form $g(u\bar{u} - d_c\bar{d}_c)$, and

$$d_c\bar{d}_c = d\bar{d}\cos^2\theta_c + s\bar{s}\sin^2\theta_c + (d\bar{s} + s\bar{d})\sin\theta_c\cos\theta_c.$$

The last term clearly represents a strangeness-changing neutral current. However, the $\mathrm{BR}(K_L \rightarrow \mu^+\mu^-) = 6.3 \times 10^{-9}$, compared to, for example, the charged-current

decay BR($K^+ \to \mu^+\nu$) = 63.5%. This means that to lowest order there should be no $s\bar{d}$ coupling. GIM proposed a second weak isospin doublet:

$$w_2 = \begin{pmatrix} c \\ s_c \end{pmatrix},$$

consisting of the new charm quark and $s_c = s\cos\theta_c - d\sin\theta_c$. The neutral current now becomes $g(u\bar{u} - d_c\bar{d}_c + c\bar{c} - s_c\bar{s}_c)$, and

$$\begin{aligned} d_c\bar{d}_c + s_c\bar{s}_c &= d\bar{d}\cos^2\theta_c + s\bar{s}\sin^2\theta_c + (d\bar{s} + s\bar{d})\sin\theta_c\cos\theta_c \\ &+ s\bar{s}\cos^2\theta_c + d\bar{d}\sin^2\theta_c - (d\bar{s} + s\bar{d})\sin\theta_c\cos\theta_c \\ &= d\bar{d} + s\bar{s}. \end{aligned}$$

The strangeness-changing neutral current has now dropped out. Furthermore, they managed to put a bound on the charm quark mass of $m_c \sim 1 - 3$ GeV based on the branching ratio limits.

Meanwhile, in 1967, a SLAC-MIT collaboration started inelastic ep scattering experiments with beam energies up to 20 GeV. The differential cross section in the lab frame for the scattering of an electron with energy E to a state with energy E' into solid angle Ω is calculated to be:

$$\frac{d\sigma}{dE'd\Omega} = \frac{\alpha^2}{4E^2\sin^4\frac{\theta}{2}}\{W_2(\nu, Q^2)\cos^2\frac{\theta}{2} + 2W_1(\nu, Q^2)\sin^2\frac{\theta}{2}\}, \tag{1.1}$$

where $\nu = E - E'$, Q^2 is the momentum transfer, and θ is the azimuthal scattering angle relative to the beam direction. In 1969, Bjorken and Paschos [Bjo 69] predicted that if the proton were made up of point-like constituents (called partons by Feynman), then the form factors W_1 and W_2, at large Q^2, should satisfy Bjorken scaling:

$$\begin{aligned} MW_1(\nu, Q^2) &\to F_1(x) \\ \nu W_2(\nu, Q^2) &\to F_2(x), \end{aligned} \tag{1.2}$$

where $x = Q^2/2M\nu$, and M is the proton mass. Thus one expects a Rutherford-type $\sin^{-4}\frac{\theta}{2}$ dependence of the cross section at large Q^2. Observation of this effect would reveal the point-like nature of the scattering, just as it revealed the substructure of the atom in Rutherford's original experiment. Bjorken scaling was observed by the SLAC-MIT collaboration [SL 72], and explained by Feynman's parton model [Fey 72] in which x is identified with the fraction of the proton's momentum carried by the

parton. Further experiments showed that the partons had the same quantum numbers as quarks, leading to the identification of the two.

This quark-as-parton postulate was strengthened in 1974 when the J/ψ meson, a narrow state of mass 3.097 GeV, was observed at SLAC [Aug 74] and Brookhaven [Aub 74], and interpreted as a $c\bar{c}$ bound state. This interpretation was shown to be correct when open charm mesons (particles with a single charm quark) were observed at SLAC in 1976 [Gol 76]. In 1977, yet another quark, called beauty or bottom, was observed in $b\bar{b}$ bound states (the Υ states) at FNAL [Her 77, Inn 77]. Searches for the expected top quark have not yet been successful — however, its mass has been constrained to be above 90 GeV by the CDF Collaboration at FNAL [Sli 90].

Further evidence for the existence of quarks comes from the famous ratio

$$R(\sqrt{s}) \equiv \frac{\sigma(e^+e^- \rightarrow \text{hadrons})}{\sigma(e^+e^- \rightarrow \mu^+\mu^-)}. \tag{1.3}$$

The expected value of this ratio is $3\sum_i e_i^2$, where i runs over all quark flavours whose mass is small enough that they are able to be produced at the given centre of mass energy $\sqrt{s}$. Thus, as $\sqrt{s}$ is increased, the ratio undergoes discrete jumps at energies corresponding to the production thresholds of charm, beauty, and (eventually) top quarks. The ratio should be 2 at energies below the charm production threshold, 10/3 just above this threshold, and 11/3 above the bottom quark threshold. This has been confirmed by a combination of many experiments at SLAC, DESY, Cornell, and KEK (see, for example, [PDG 90]). The factor of 3 in the expression for R is evidence of quark colour, and will be discussed in the next section.

1.3 Quantum Chromodynamics

The Δ^{++} baryon, discovered in 1951 posed yet another problem. The quark content of the baryon was clearly uuu, its spin was 3/2 and its orbital angular momentum was 0. Hence, if we write the wavefunction as:

$$\psi = \alpha(\text{space})\beta(\text{spin}),$$

we see that since $L = 0$ and $S = 3/2$, both α and β are symmetric under the interchange of any two quarks. This clearly violates Fermi-Dirac statistics since any wavefunction must be antisymmetric under the exchange of identical fermions. A new quantum number is needed, which is called colour. The Δ^{++} wavefunction is then:

$$\psi = \alpha(\text{space})\beta(\text{spin})\gamma(\text{colour}),$$

with the requirement that γ is antisymmetric under particle exchange. This implies that quarks must come in at least 3 colours. Convincing evidence that there are exactly 3 colours comes from the ratio R (Eqn.(1.3)). If quarks come in N_c colours. R should be given by:

$$R(\sqrt{s}) = N_c \sum_i e_i^2,$$

where i runs over all quark species above threshold. Experiments (see above) support the value $N_c = 3$. Further evidence for the 3 colour assignment comes from the π^0 lifetime. The decay rate $\Gamma(\pi^0 \rightarrow \gamma\gamma)$ is proportional to N_c^2, and is predicted to be 0.866 eV for $N_c = 1$, and 7.75 eV for $N_c = 3$. The measured rate is 7.74 ± 0.55 eV [PDG 90], clearly favouring 3 colours.

The establishment of quarks as fundamental particles with colour led to the search for a theory of quark dynamics. Bjorken scaling, interpreted within the parton model, implies that at large Q^2 (which by the uncertainty principle corresponds to short distance) the quarks inside the nucleon appear almost free. Hence, this theory must have the property that the force becomes weaker at shorter and shorter distances. It was found that the only gauge theories with this property in 4 dimensions were non-Abelian (i.e. the generators of the gauge group do not commute) [Col 73]. It was natural to suggest that the colour degree of freedom of quarks was associated with the gauge symmetry of the theory. This led to the development of Quantum Chromodynamics (QCD), which was first set forth in its present form in 1973 ([Gro 73, Wei 73, Fri 73]). QCD postulates that each quark can come in any of 3 colour 'charges', Red, Green, and Blue, and that the three coloured quark fields form an SU(3) triplet. Antiquarks come in the anti-colours ($\bar{\mathrm{R}}$,$\bar{\mathrm{G}}$,$\bar{\mathrm{B}}$), which form a triplet which transforms according to the $\mathbf{3}^*$ complex conjugate representation. The (strong) force between coloured objects is mediated by 8 neutral gauge fields, called gluons (8 since there are 8 generators of SU(3)). Each gluon has both a colour and an anti-colour (e.g. $\mathrm{R}\bar{\mathrm{G}}$). One feature of colour is that it has never been directly observed, and in fact it is postulated that all observable particles are colour singlets (i.e. invariant under $\mathrm{SU(3)_c}$ rotations). An easy way to keep track of this is to demand that all real particles be 'white'. For example, $\mathrm{R}\bar{\mathrm{R}}$, $\mathrm{G}\bar{\mathrm{G}}$, RGB, and $\bar{\mathrm{R}}\bar{\mathrm{G}}\bar{\mathrm{B}}$ combinations are all white. This immediately implies that the only possible combinations of quarks and antiquarks which can exist are: $q\bar{q}, qqq, \bar{q}\bar{q}\bar{q}, q\bar{q}q\bar{q}, qqqq\bar{q}$ etc., explaining why no particles seem to be made of, for example, qq.

The QCD Lagrangian is [Che 84]:

$$L_{QCD} = -\frac{1}{4}G^a_{\mu\nu}G^{\mu\nu}_a + \sum_{flavours} \bar{q}(i\gamma^\mu D_\mu - m_q)q,$$

with

$$\begin{aligned} D_\mu &= \partial_\mu + igT_aG^a_\mu \\ G^a_\mu\nu &= \partial_\mu G^a_\nu - \partial_\nu G^a_\mu - gf_{abc}G^b_\mu G^c_\nu, \end{aligned}$$

where the q's are quark fields, the G^a_μ's are gluon fields and the T_a's are the 8 generators of SU(3). The generators satisfy the commutation relations $[T_a, T_b] = if_{abc}T_c$, where f_{abc} are the group's structure constants. As stated above, QCD is a non-Abelian theory, i.e. the generators T_a do not commute. This leads to the conclusion that gluons can interact directly with one another, as is evident from the $gf_{abc}G^b_\mu G^c_\nu$ term in the field-strength tensor. This is in contradistinction with photons, the carriers of the electromagnetic force. Both 3 and 4 gluon vertices arise in QCD.

A consequence of these interactions is that a sort of anti-screening of colour charge occurs. That is, the farther away one is from a (bare) colour charge, the stronger it seems — once again in direct contrast to the screening of QED. QCD, like QED is a renormalisable theory. Solving the Renormalisation Group Equation to third order in the coupling constant g gives the following expression:

$$\alpha_s(Q^2) = \frac{g^2}{4\pi} = \frac{4\pi}{(11 - \frac{2}{3}n_f)\ln(Q^2/\Lambda^2)},$$

where n_f is the number of quark flavours (currently believed to be 6) and $\Lambda \sim 200$ MeV, which has been measured by various experiments. (In fact, the value of Λ depends on which renormalisation scheme is used.) This running of the coupling constant with Q^2 leads to the concept of asymptotic freedom; in strong interactions with large momentum transfer (short distances) the coupling constant is relatively small (~ 0.2), as demanded by Bjorken scaling. However for small Q^2 (large distances) the coupling constant can be ~ 1, which makes the application of standard perturbative techniques problematic.

Experimental evidence for the existence of gluons comes from many sources. For example, in the parton model, the structure function F_2 satisfies:

$$\frac{1}{x}F_2(x) = \sum_i e_i^2 f_i(x), \tag{1.4}$$

where i runs over all partons in the proton, e_i is the electric charge of the parton, and $f_i(x)$ is the number density of the parton with momentum fraction x. We define the quark distribution function $u(x)$ to be the number density of u quarks in the proton, $\bar{u}(x)$ the number density for $\bar{u}$ antiquarks, and similarly define $d(x), \bar{d}(x), s(x)$, and $\bar{s}(x)$. These functions can be obtained from deep inelastic scattering off protons and neutrons, along with constraints based on the target's quark content. For example:

$$\begin{aligned}\int_0^1 (u(x) - \bar{u}(x))dx &= 2 \\ \int_0^1 (d(x) - \bar{d}(x))dx &= 1 \\ \int_0^1 (s(x) - \bar{s}(x))dx &= 0.\end{aligned}$$

since the proton is a (uud) state. However, when one sums the total momentum carried by the quarks one gets:

$$\int_0^1 x(u(x) + \bar{u}(x) + d(x) + \bar{d}(x) + s(x) + \bar{s}(x))dx = 0.54 \pm 0.05.$$

showing that approximately half the proton's momentum must be carried by neutral partons, i.e. the gluons.

Furthermore, the explicit Q^2 independence of the structure function F_2 is not exact when one includes QCD effects. The quark distribution functions become slightly dependent on Q^2; this dependence is given by the Altarelli-Parisi equation [Alt 77]:

$$\frac{d}{d\log Q^2} q(x, Q^2) = \frac{\alpha_s}{2\pi} \int_x^1 \frac{dy}{y} q(y, Q^2) P_{qq}(\frac{x}{y}).$$

Here $P_{qq}(\frac{x}{y})$ is the probability that a quark of momentum fraction y emits a gluon of momentum fraction $y - x$. A similar equation holds for gluons. The violations of Bjorken scaling in F_2 were first seen in a μFe scattering experiment at Fermilab [Fox 74].

Direct evidence for the existence of gluons came from the observation of $e^+e^- \rightarrow qq\bar{q} \rightarrow 3$ hadron jets events by the TASSO, PLUTO, MARK J, and JADE collaborations ([Bra 79, Ber 79, Bar 79, Bar 79a]) at the PETRA storage ring at DESY.

Table (1.3) contains a brief summary of our present knowledge of fundamental particles and forces.

1.4 Charm Physics

After the discovery of the J/ψ $c\bar{c}$ bound state in 1974, a search was started for the expected open charm hadrons — particles containing only one charm quark. In 1976

Gen.	Part.	J	Q	B	L_e	L_μ	L_τ	Colour	Flavour	Mass
1^{st}	u	1/2	2/3	1/3	0	0	0	R,G,B	$I = 1/2,\ I_3 = 1/2$	~ 4 MeV
	d	1/2	$-1/3$	1/3	0	0	0	R,G,B	$I = 1/2,\ I_3 = -1/2$	~ 7 MeV
	e	1/2	-1	0	1	0	0	0	0	511 KeV
	ν_e	1/2	0	0	1	0	0	0	0	< 17 eV
2^{nd}	c	1/2	2/3	1/3	0	0	0	R,G,B	$C = 1$	~ 1.5 GeV
	s	1/2	$-1/3$	1/3	0	0	0	R,G,B	$S = -1$	~ 0.3 GeV
	μ	1/2	-1	0	0	1	0	0	0	106 MeV
	ν_μ	1/2	0	0	0	1	0	0	0	< 270 KeV
3^{rd}	t	1/2	2/3	1/3	0	0	0	R,G,B	$T = 1$	$?(> 90)$
	b	1/2	$-1/3$	1/3	0	0	0	R,G,B	$B = -1$	~ 5
	τ	1/2	-1	0	0	0	1	0	0	1.78 GeV
	ν_τ	1/2	0	0	0	0	1	0	0	< 35 MeV

Force	Mediator	Q	Spin	Mass	Coupling Constant	Typical Lifetime
Strong	gluon (g)	0	1	0	$0.2 - 1$	10^{-23} s
Electromagnetic	photon (γ)	0	1	0	1/137	10^{-18} s
Weak	W bosons ($W^\pm$)	± 1	1	$M_W = 81$ GeV	10^{-5}	10^{-8} s
	Z boson (Z^0)	0	1	$M_Z = 91$ GeV		
Gravitational	graviton (G)	0	2	0	-	-

Table 1.1: Summary of elementary particles and forces

two such states, the D^+ and D^0 mesons, were observed at the SPEAR e^+e^- storage ring at SLAC [Gol 76, Per 76]. The accelerator was tuned to a center of mass energy of 3770 MeV, corresponding to the $\psi(3770)$ resonance. About half of these ψ's decay to $D\bar{D}$ pairs, allowing the extraction of clean $D^+ \to K^-\pi^+\pi^+$ and $D^0 \to K^-\pi^+$ (and charge conjugate) signals. However, the produced D's are very nearly at rest, making a lifetime determination difficult. The D mesons were identified as pseudoscalars from the angular distribution of the decay $\psi(3770) \to D\bar{D}$.

Over the next several years, vector mesons with the same quark content as the pseudoscalars were found — these are known as D^*'s [Gol 77, Fel 77]. Later a charm-strange state (now called the D_s) was observed by the CLEO collaboration [Che 83]. This was quickly followed by the observation of the corresponding vector meson (D_s^*) by the ARGUS collaboration and at the PEP storage ring at SLAC [Alb 84, Aih 84]. Table 1.2 lists the properties of the lowest-lying charm states.

While the above e^+e^- experiments continued to research the spectroscopy and

Particle	Quark Content	J^P	Mass (GeV)	Lifetime (s)
$D^0/\bar{D}^0$	$c\bar{u}$	0^-	1.8645	4.21×10^{-13}
$D^\pm$	$c\bar{d}$	0^-	1.8693	10.62×10^{-13}
$D_s^\pm$	$c\bar{s}$	0^-	1.9688	4.45×10^{-13}
$D^{*0}/\bar{D}^{*0}$	$c\bar{u}$	1^-	2.010	$\Gamma < 2.1$ MeV
$D^{*\pm}$	$c\bar{d}$	1^-	2.010	$\Gamma < 1.1$ MeV
$D_s^{*\pm}$	$c\bar{s}$	1^-	2.110	$\Gamma < 4.5$ MeV

Table 1.2: Summary of Lowest Mass Charm Mesons

branching ratios of the charmed particles. fixed target charm experiments were undertaken at FNAL and CERN. These have the advantage that the charmed particle is moving very quickly in the lab frame: it is therefore possible to directly detect the charm decay vertex. The first direct observation of charm decay came from a neutrino emulsion experiment at FNAL [Bur 76], which established that the charm lifetime was $\sim 10^{-12} - 10^{-13}$ s. Other neutrino experiments observed the first charmed baryons [Caz 75, Amm 80].

The first observation of charm produced in hadron-hadron interactions came from pp collisions at the ISR (Intersecting Storage Ring) at CERN [Dri 79]. During the late 1970's and early 1980's, most of the results on the hadroproduction of charm came from either ISR experiments or beam dump experiments. In a beam dump experiment, a particle beam is 'dumped' into a target of metal plates whose average density can be adjusted by changing their spacing. Downstream of this 'dump' is a detector which measures either the neutrino or muon flux at various effective target densities. Extrapolating these measurements to infinite target density allows a measurement of the charm cross section. However, such experiments usually measure neutrinos or muons only in a small forward cone, and with a limited energy range. As a result, there are large errors in extrapolating from the measured flux to the full cross section.

In the mid-1980's the focus of hadroproduction experiments shifted to detectors which allowed the complete reconstruction of the charm decays. Two experiments at CERN dominated this field. The first was the NA16/NA27 LEBC-EHS group. This group used a bubble chamber (the LEBC) with a conventional spectrometer (the EHS) behind it. Their results include measurements of charmed particle lifetimes and branching ratios, as well as D meson cross sections in $\pi^- p$ and pp interactions

at energies of 360 and 400 GeV ([Agu 84, Agu 86, Agu 88]). The other group, the ACCMOR Collaboration (NA11/NA32), obtained results using a spectrometer which was one of the first to use silicon microstrip detectors. They too measured charmed particle lifetimes and masses, as well as the total D meson cross section at energies of 200 and 230 GeV, with incident pions, kaons, and protons on a variety of different targets ([Bar 88, Bar 91]).

Because these experiments are not sensitive to the entire kinematic range in which charm is produced, it is necessary to have a means of extrapolating measurements from the region in which they are sensitive to the full range. This is done by parameterizing the differential cross section as:

$$\frac{d^2\sigma}{dx_F dp_t^2} = A(1-|x_F|)^n e^{-bp_t^2}. \tag{1.5}$$

Here, x_F is the Feynman x variable, defined as $x_F = p_L/p_{L_{max}}$, where p_L is the particle's centre of mass momentum component along the beam direction, and $p_{L_{max}}$ is the maximum possible value for p_L. For particles whose mass is small compared to the centre of mass energy $\sqrt{s}$, we have $x_F = 2p_L/\sqrt{s}$. p_t is defined as the momentum component perpendicular to the beam direction. A is simply a normalisation constant. The experiments fit the constants n and b in the region which they are sensitive, and then use Eqn. 1.5 to extrapolate to the total cross section.

Comparing the cross sections measured by diverse experiments is rather problematic, however, because the target materials range from hydrogen to uranium. In order to convert the measured *per nucleus* cross section from a heavy target, such as tungsten, to a measurement *per nucleon*, the atomic number (A) dependence of the cross section must be known. The usual parameterization of this dependence is $\sigma(\text{nucleus}) = \sigma(\text{nucleon})A^\alpha$. For a hard process such as charm production, the expectation is that $\alpha \sim 1$ (see Sec. 2.2). (For comparison, the total inelastic cross section has $\alpha \sim 0.72$ [Car 79].)

Indirect evidence that $\alpha \sim 1$ comes from comparing the cross sections measured by experiments with different target materials. The values listed below are measurements of the total cross section to produce a D or $\bar{D}$ with $x_F > 0$. If we assume a linear A-dependence, the cross sections for incident protons are:

- CCFRS (350 GeV p-Fe) (beam dump) $\sigma(D/\bar{D}+X) = 11.1 \pm 1.1 \pm 1.8\ \mu$b [Rit 83]
- LEBC-EHS (360 GeV p-p) (bubble chamber) $\sigma(D/\bar{D}+X) = 15.5^{+8.2}_{-4.6}\ \mu$b [Agu 84]
- LEBC-EHS (400 GeV p-p) (bubble chamber) $\sigma(D/\bar{D}+X) = 15.1 \pm 1.7\ \mu$b [Agu 88]
- FNAL E613 (400 GeV p-W) (beam dump) $\sigma(D/\bar{D}+X) = 15.5 \pm 0.8 \pm 2.3\ \mu$b [Duf 86].

For incident pions, the following values have been measured:

- ACCMOR (200 GeV π^--Si) (spectrometer with silicon) $\sigma(D/\bar{D}+X) = 6.7 \pm 0.8 \pm 0.4\ \mu$b [Bar 88]
- ACCMOR (230 GeV π^--Cu) (spectrometer with silicon) $\sigma(D/\bar{D}+X) = 9.5 \pm 0.4 \pm 1.9\ \mu$b [Bar 91]
- CCFRS (278 GeV π^--Fe) (beam dump) $\sigma(D/\bar{D}+X) = 17.5^{+5.4}_{-3.9}\ \mu$b [Rit 84]
- LEBC-EHS (360 GeV π^-p) (bubble chamber) $\sigma(D/\bar{D}+X) = 15.8 \pm 2.7\ \mu$b [Agu 86].

The consistency of these measurements strongly favours a linear A-dependence. However, two beam dump experiments have measured α, and find values significantly lower than 1:

- 300 GeV pN $\alpha = 0.78 \pm 0.07$ $< x_F >= 0.23$ [Cob 88]
- 400 GeV pN $\alpha = 0.75 \pm 0.05$ $< x_F >= 0.45$ [Duf 85]
- 320 GeV π^-N $\alpha = 0.80 \pm 0.05$ $< x_F >= 0.27$ [Cob 87].

If we use a value of 0.75 for α, though, the cross section measurements appear chaotic. For example, the proton beam cross sections per nucleon become: $30.4 \pm 3.0 \pm 4.9\ \mu$b (350 GeV beam), $15.5^{+8.2}_{-4.6}\ \mu$b (360 GeV beam), $15.1 \pm 1.7\ \mu$b, and $57.1 \pm 2.9 \pm 8.5\ \mu$b (400 GeV beam).

With an α of 0.8, the pion beam cross sections become: $13.0 \pm 1.6 \pm 0.8$ μb (200 GeV beam), $21.8 \pm 0.9 \pm 4.4$ μb (230 GeV beam), $39.1^{+12.1}_{-8.7}$ μb (278 GeV beam), and 15.8 ± 2.7 μb (360 GeV beam).

It is possible that this discrepancy can be explained by an x_F dependence of the exponent α. For light quark production, α ranges from $\alpha(x_F = 0) \simeq 0.7$ to $\alpha(x_F = 0.9) \simeq 0.45$ [Bar 83]. Similar results have been found in J/ψ production: several groups observed α decreasing from $\alpha(x_F = 0) \simeq 1$ to $\alpha(x_F = 0.8) \simeq 0.8$ [Ant 78, Cor 82, Bar 83]. However, as stated above, the open charm cross section is found to follow a $(1 - x_F)^n$ parameterization, and $n \sim 5$ at beam energies in the 300–400 GeV range [Agu 88]. The bulk of the cross section is clearly in the central region near $x_F = 0$. Thus, comparing total cross sections from various experiments sets the value of α at $x_F = 0$. Whereas, as listed above, the experiments which measured α directly are sensitive only to the cross section well outside the central x_F region.

Experiments in this early phase of charm physics were plagued by either large correction factors (as in beam dumps), or low statistics (e.g. the π^-–Si result from ACCMOR came from a total of $\sim$ 150 D's). The introduction of silicon microstrip detectors (see Sec.4.1.1) made high statistics experiments with good acceptance possible. In 1985, experiment E691 ran at FNAL's Tagged Photon Lab using a photon beam, and collected more than 10,000 fully reconstructed charm events. This thesis describes results from experiment E769, the follow-on experiment at the same lab. Measurements of the A-dependence and total charm cross section of πN collisions are presented.

Chapter 2

Charm Cross Sections

Calculating hadron-hadron cross sections within the framework of QCD is fraught with difficulties. Because quarks and gluons are confined within hadrons, there are many soft, long-range effects which cannot be calculated by perturbative techniques. The Operator Product Expansion (OPE) provides a method for dealing with these problems. In calculating hadron-hadron scattering amplitudes, a matrix element of a product of currents must be calculated. There is a problem, however, in that the product of two currents at the same spacetime point is not well defined. The OPE ([Wil 64]) gives meaning to the product of two operators by expanding it in a series of well-defined local operators with c-number coefficient functions. The coefficients contain all the singularities. Using the OPE, it has been proven [Col 84] that the expression for the hadron-hadron to heavy lepton pair cross section *factorizes*. That is, it can be broken up into a short-distance part, which is in principle calculable by perturbative techniques, and a long-range, non-perturbative part.

The translation of this result into the familiar language of the parton model results in a particularly simple form for the cross sections. For example, in the interaction of the hadrons A and B, the cross section for the production of a heavy lepton pair factorizes as:

$$\sigma_{l^+l^-}(s) = \int dx \int dy \Big(\sum_{i,j=partons} G_{p_i/A}(x) G_{p_j/B}(y) \hat{\sigma}_{p_i p_j \to l^+l^-}(\hat{s} = xys) \Big). \qquad (2.1)$$

Here:

- The sum runs over all parton types p_i (e.g. u, d, g) in hadron A, and types p_j in hadron B, which can interact to form a l^+l^- pair:
- $G_{p_i/A}(x)$ is the number density of partons of type p_i in particle A with a fraction x of the parent's momentum (similarly for $G_{p_j/B}(y)$). $G_{p_i/A}(x)$ is known as a

structure function. These structure functions contain long-range effects and are not calculable, but are experimentally obtained quantities:

- $s = E_{cm}^2$ is the usual Mandelstam variable:
- $\hat{s} = xys$ is the corresponding variable for the parton subsystem;
- $\hat{\sigma}_{p_ip_j \to l^+l^-}(\hat{s})$ is the short-distance $p_ip_j \to l^+l^-$ cross section. It is this part which can be calculated using perturbative QCD.

Also, in the parton model the masses of the interacting partons are taken to be zero, and mass singularities occur in the full expression for the cross section. Factorization allows one to absorb these singularities into the definition of the structure functions $G_{p_i/A}(x)$.

The proof of factorization in QCD has been extended to include heavy quark production [Col 86]; however, there may be additional corrections of $\mathcal{O}(\Lambda_{QCD}/M_Q)$, where M_Q is the heavy quark mass [Bro 87]. These are known as higher-twist effects. The size of these effects is unknown at present, and current theoretical estimates of heavy quark cross sections use the factorized formula.

2.1 The Charm Cross Section

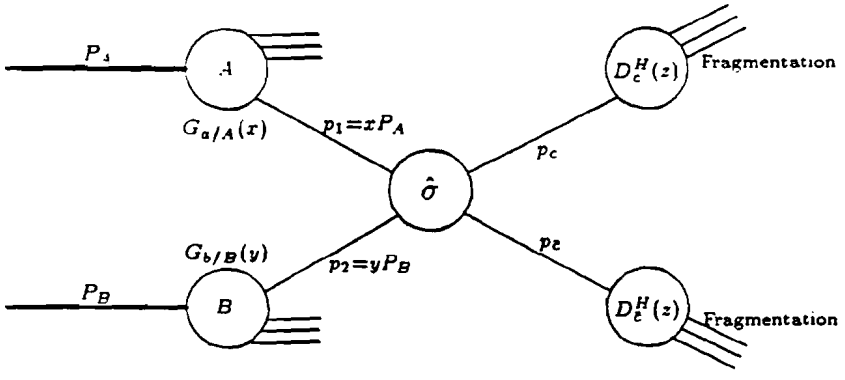

Figure 2.1: Kinematics of collision process

In this section we outline the current state of theoretical predictions for the total charm cross section in hadron-hadron collisions. Figure 2.1 shows the relevant kinematics. Note that the production process has been divided into three parts. The

diagram depicts a collision between the incident hadron A and the target hadron B, with an overall centre of mass energy $\sqrt{s}$. The sub-collision which produces the charm quarks takes place between two partons; either two gluons or a quark-antiquark pair. Hence, as above, we factorize the $c\bar{c}$ cross section into two parts, one described by the structure functions G, and the other describing the hard interaction, $\hat{\sigma}$. The fractions of the parent particles' momenta carried by the partons are defined to be x (from A) and y (from B), and are distributed according to the parents' gluon/quark distribution functions.

To calculate the total $c\bar{c}$ cross section, we only need to know the structure functions, G, and the parton-parton cross sections, $\hat{\sigma}$. However, because free quarks are not observable, experiments cannot directly measure the $c\bar{c}$ cross section. After the quarks are produced, they must *hadronize* (also known as *fragment*) into real mesons and/or baryons. The functions which describe this behaviour are called *fragmentation functions*. This process is represented by the functions $D_c^H(z)$ in Figure 2.1. Because fragmentation is a soft process, these functions are not calculable, but are given instead by phenomenological fits to data. Fragmentation does not alter the value of the total cross section, but it does affect, for example, the open charm cross section, or the D^+ meson cross section. This is particularly important for this thesis as we measured the total D meson cross section and then used a Monte Carlo of the fragmentation process to extrapolate to the total open charm cross section. We did not measure the cross section for the production of any bound-state charm mesons, and so it is not relevant to compare our data to the entire $c\bar{c}$ cross section.

With this in mind, we write the formula for the total charm cross section for high energy AB collisions as:

$$\sigma_{c\bar{c}}(s) = \int_{x_{min}}^{1} dx \int_{\frac{x_{min}}{x}}^{1} dy \Big(\sum_{i,j=partons} G_{p_i/A}(x) G_{p_j/B}(y) \hat{\sigma}_{p_i p_j \to c\bar{c}}(\hat{s} = xys) \Big), \quad (2.2)$$

where:

- $G_{p_i/A}(x)$ and $G_{p_j/B}(y)$ are the structure functions of partons of type p_i in hadron A, and p_j in hadron B;
- x and y are the momentum fractions carried by the two partons;
- $\hat{s} = xys$ is the square of the centre of mass energy for the parton-parton subsystem;

- x_{min} is the minimum momentum fraction kinematically allowed. In the case of charm production, $\hat{s}_{min} = 4m_c^2 = x_{min}s$, so $x_{min} = 4m_c^2/s$;
- $\hat{\sigma}_{p_ip_j \to c\bar{c}}(\hat{s})$ is the short-distance $p_ip_j \to c\bar{c}$ cross section.

To make the formulae clearer, we will concentrate on only one process, $\sigma_{gg\to c\bar{c}}(s)$. There are similar formulae for each of the possible parton subprocesses $u\bar{u} \to c\bar{c}$, $d\bar{d} \to c\bar{c}$, and $s\bar{s} \to c\bar{c}$. The total cross section is just the sum of these: $\sigma_{c\bar{c}}(s) = \sigma_{gg\to c\bar{c}}(s) + \sum_i \sigma_{q_i\bar{q}_i}(s)$.

By introducing the variable $\tau = xy$ we can rewrite the gluon-gluon part of Eqn. 2.2 as

$$\sigma_{gg\to c\bar{c}}(s) = \int_{\tau_{min}}^{1} d\tau \int_{\tau}^{1} \frac{dx}{x} G_{g/A}(x) G_{g/B}(\frac{\tau}{x}) \hat{\sigma}_{gg\to c\bar{c}}(\tau s) \tag{2.3}$$

or

$$\sigma_{gg\to c\bar{c}}(s) = \int_{\tau_{min}}^{1} d\tau \frac{d\mathcal{L}_{gg}}{d\tau} \hat{\sigma}_{gg\to c\bar{c}}(\tau s), \tag{2.4}$$

where

$$\frac{d\mathcal{L}_{gg}}{d\tau} = \int_{\tau}^{1} \frac{dx}{x} G_{g/A}(x) G_{g/B}(\frac{\tau}{x}) \tag{2.5}$$

is called the *gluon luminosity*. It is a measure of the number density of parton pairs with a given τ (or $\hat{s}$). Its derivation is described below.

2.1.1 The Parton Luminosities

In order to calculate the gluon luminosity function (cf. Eqn. 2.5) as well as the appropriate quark-antiquark luminosities, we need to know the structure functions $G_{g/A}$ and $G_{g/B}$ for all types of beam and target particles. These include pions, protons, and neutrons. Many sets of structure functions are available; common choices are Duke and Owens (sets DO1 and DO2), EHLQ, Morfin-Tung, etc. In our analysis, we use the Duke and Owens parameterization for protons and neutrons [Duk 84], and the Owens parameterization for pions [Owe 84], since these are the only sets which treat all three particles consistently. Figure 2.2 and Figure 2.3 show the parton distribution functions for protons and pions in the DO1 parameterization.

In these plots, $g(x)$ is the gluon distribution function, $u_v(x)$ and $d_v(x)$ are the valence u and d quark distributions, and $S(x)$ is the sea quark distribution, which is

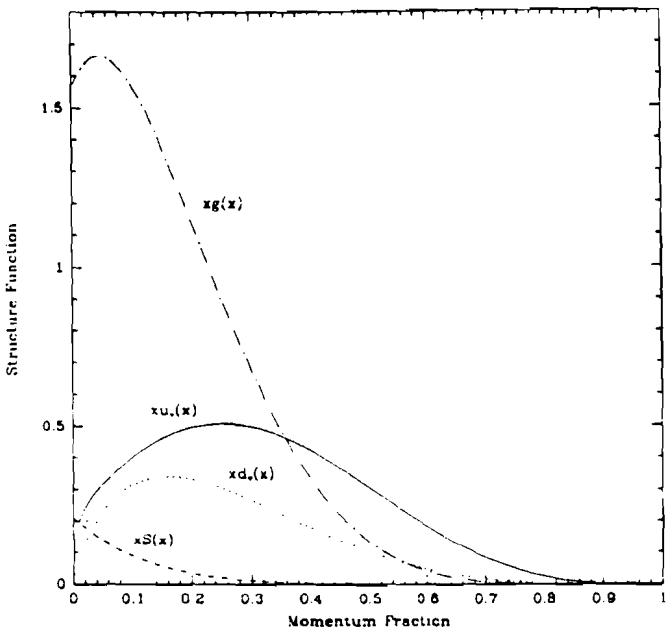

Figure 2.2: Parton Structure Functions for Protons (DO1 set)

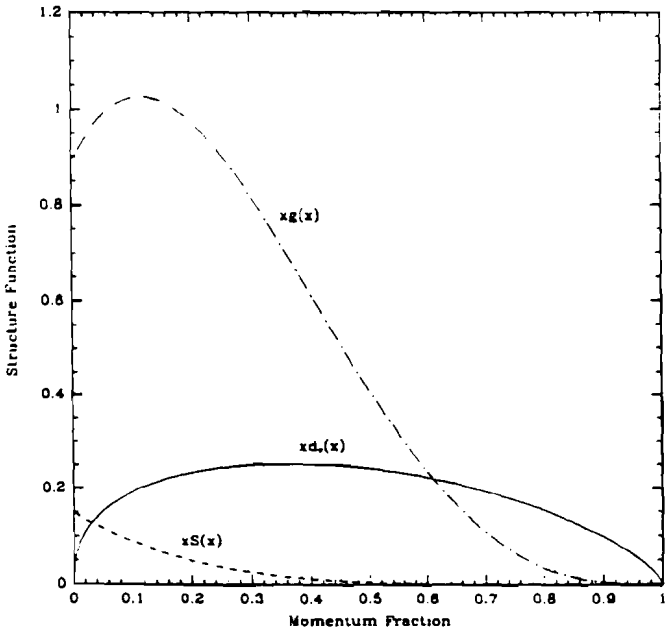

Figure 2.3: Parton Structure Functions for Pions (DO1 set)

assumed to be made up of equal numbers of $u\bar{u}$, $d\bar{d}$, and $s\bar{s}$. The charm quark content is too small to appear on the plot.

The quark distribution functions were extracted from deep inelastic neutrino, electron, and muon scattering experiments. The gluon distribution, to which the charm cross section is most sensitive, comes from fits to the x_F distribution of J/ψ production.

The distribution functions are specified at $Q_0^2 = 4(GeV/c)^2$, and then evolved to higher values of Q^2 using the Altarelli-Parisi equations. At higher values of Q^2 the distributions are shifted towards lower x. The plots show the distribution functions at Q_0^2.

Figure 2.4 shows the gluon and quark luminosities for a fixed target π^- beam with an energy of 250 GeV incident on a proton target. Note that they are strongly peaked at low values of τ.

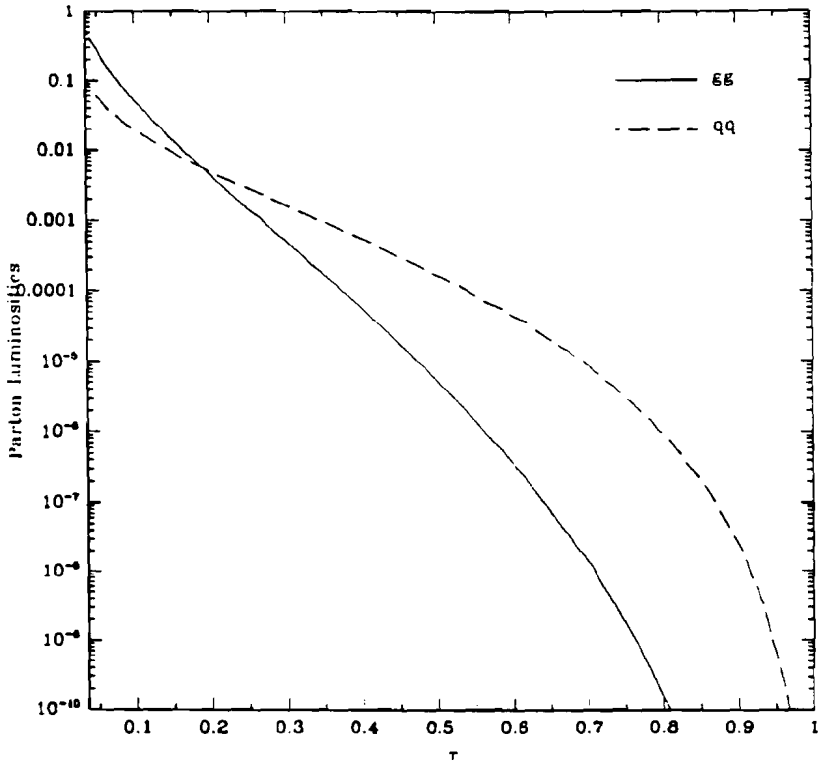

Figure 2.4: Parton Luminosity Functions

2.1.2 The Parton-Parton Cross Section

The only part of the total charm cross section which is calculable by perturbative techniques is the short-distance parton-parton interaction. This was first calculated to lowest (second) order in α_s by Babcock *et al.* in 1978 [Bab 78]. The processes of quark-antiquark annihilation and gluon-gluon fusion contribute at this order. The appropriate Feynman diagrams are shown in Figure 2.5.

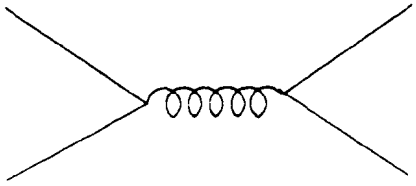

(a)

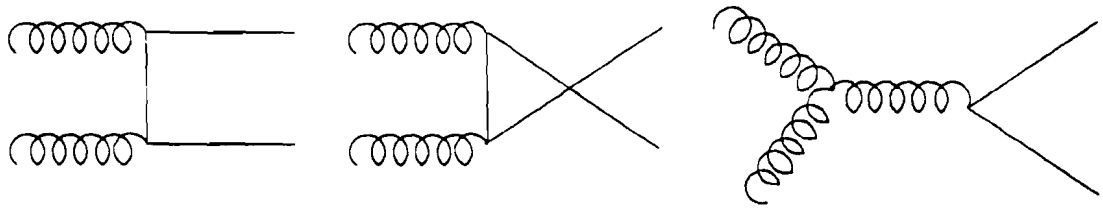

(b)

Figure 2.5: Lowest Order Diagrams for (a) $q\overline{q}$ and (b) gg

Recently, Nason, Dawson and Ellis (NDE) [Nas 88] extended this calculation to third order. Third order effects include diagrams in which there is an emission of a real gluon, and interference effects between second order diagrams and fourth order diagrams that involve virtual gluon exchange. Also, gluon-quark fusion diagrams can occur at this order; however, since their contribution to the cross section is completely negligible at the E769 beam energy, we omit them from the following discussion. Examples of relevant diagrams for $q\overline{q}$ annihilation are shown in Figure 2.6, and for gg fusion in Figure 2.7.

The presence of loops in these diagrams requires the selection of regularization and renormalisation schemes. NDE use dimensional regularization and a modified $\overline{\rm MS}$ renormalisation (see [Nas 89] for details on this). A consistent treatment involv-

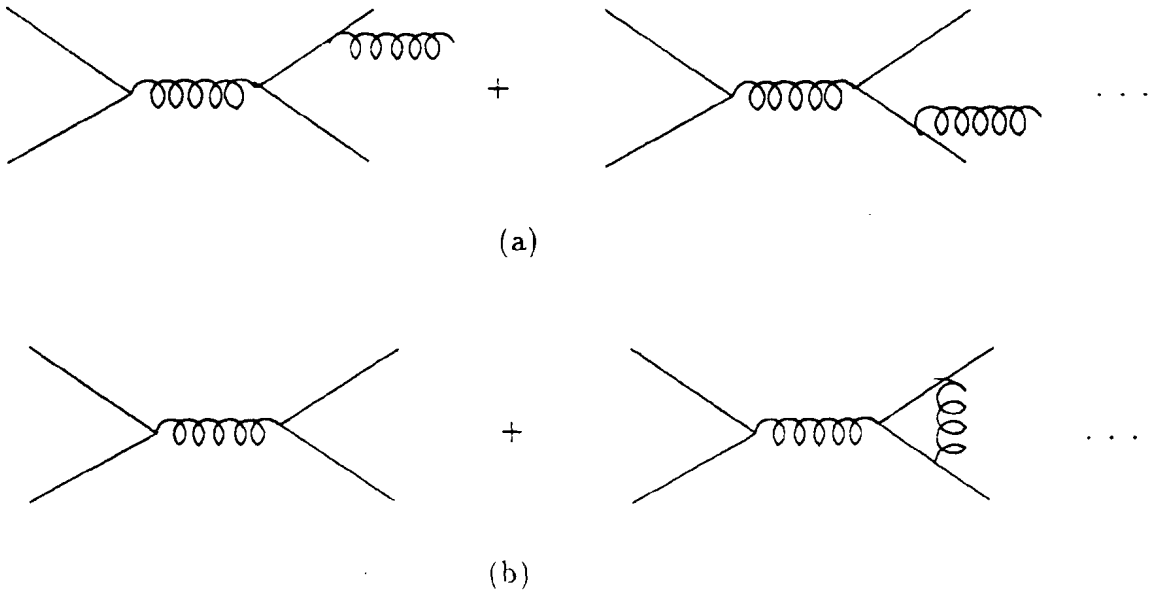

Figure 2.6: Examples of diagrams which contribute to third order in α_s for $q\bar{q}$ annihilation. (a) Real emission diagrams and (b) Virtual emission diagrams which interfere with the lowest order diagram.

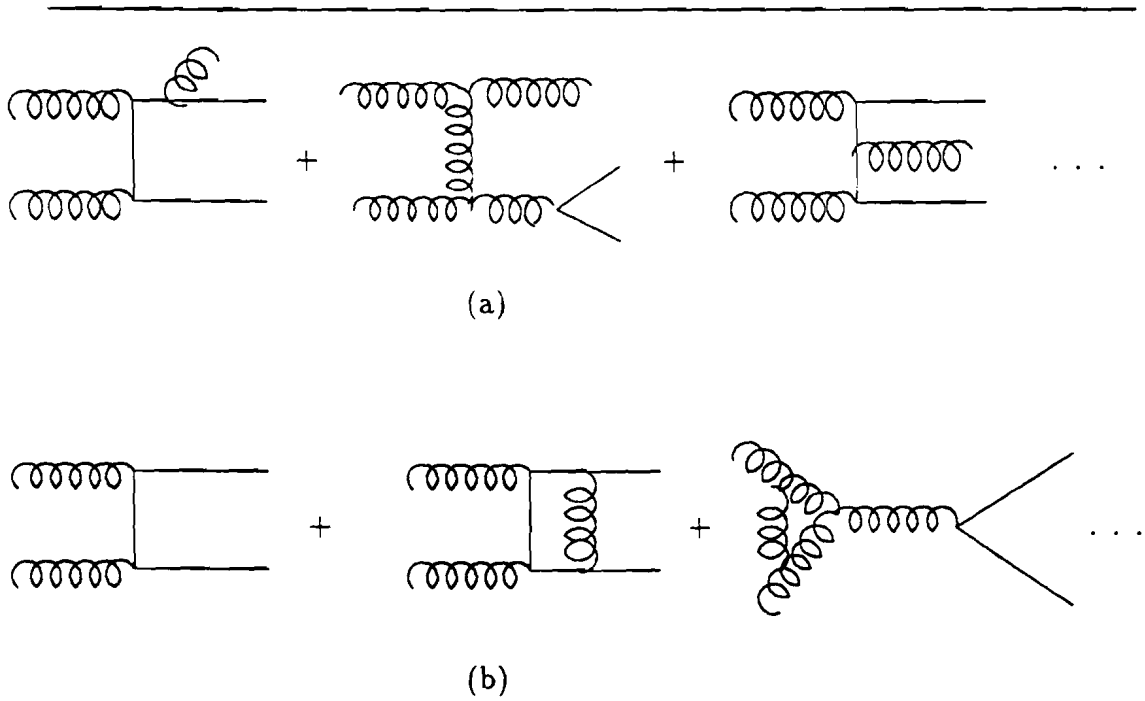

Figure 2.7: Example diagrams which contribute to third order in α_s for gg fusion. (a) Real emission diagrams and (b) Virtual emission diagrams which interfere with the lowest order diagram.

ing evaluation of the coupling constant and structure functions to third order was necessary.

NDE break up the short-distance cross section into three parts:

$$\hat{\sigma}_{c\bar{c}}(\hat{s}) = \hat{\sigma}_{c\bar{c}}^{(0)}(\hat{s}) + \hat{\sigma}_{c\bar{c}}^{(1)}(\hat{s}) + \hat{\sigma}_{c\bar{c}}^{(\bar{1})}(\hat{s}) \ln(\frac{\mu^2}{m_c^2}). \tag{2.6}$$

where:

- μ is the renormalisation scale:
- $\hat{\sigma}_{c\bar{c}}^{(0)}(\hat{s})$ is the leading (second) order parton-parton cross section:
- $\hat{\sigma}_{c\bar{c}}^{(1)}(\hat{s}) + \hat{\sigma}_{c\bar{c}}^{(\bar{1})}(\hat{s}) \ln(\mu^2/m_c^2)$ is the next-to-leading (third) order parton-parton cross section. It has been broken up into two parts — one which depends on μ only through $\alpha_s(\mu^2)$, and one with an explicit $\ln(\mu^2/m_c^2)$ dependence as well.

Figure 2.8 shows the three functions for $q\bar{q}$ annihilation, and Figure 2.9 shows those for gg fusion. The charm quark mass was chosen to be 1.5 GeV. To convert these to actual cross sections, we must convolute the parton-parton cross sections shown with the parton luminosities, as per Eqn. 2.4.

In the following we consider the particular case of $\pi^- p$ collisions. After performing the convolution, it is found that charm produced by gluon-gluon fusion constitutes 95% of the cross section, primarily because the gluon luminosity is much larger than the quark-antiquark luminosity. Also, (as the plots indicate) the next-to-leading order (NLO) cross section is larger than the leading order (LO) cross section. In fact, at the E769 beam energy of 250 GeV, the ratio of the $\pi^- p \rightarrow c\bar{c}$ cross section calculated to NLO to the cross section calculated to LO is $\sigma(\alpha_s{}^3 + \alpha_s{}^2)/\sigma(\alpha_s{}^2) \simeq 3$. This would seem to indicate that a perturbative expansion of the cross section was unreliable. However, most of the increase in the cross section comes from the new gluon-emission diagrams. The one-loop corrections to the lowest order diagrams are small compared to the LO diagrams. At higher orders, there are no fundamentally new types of diagrams — just ones with more radiated gluons, and more loops. Hence there is reason to believe that there is a large jump in cross section only between second and third order — subsequent orders are expected to have smaller and smaller contributions [Ell 90, Ber 88].

There are many sources of error in the prediction of the total charm cross section. The largest effects are due to the uncertainty in the charm quark mass, the higher

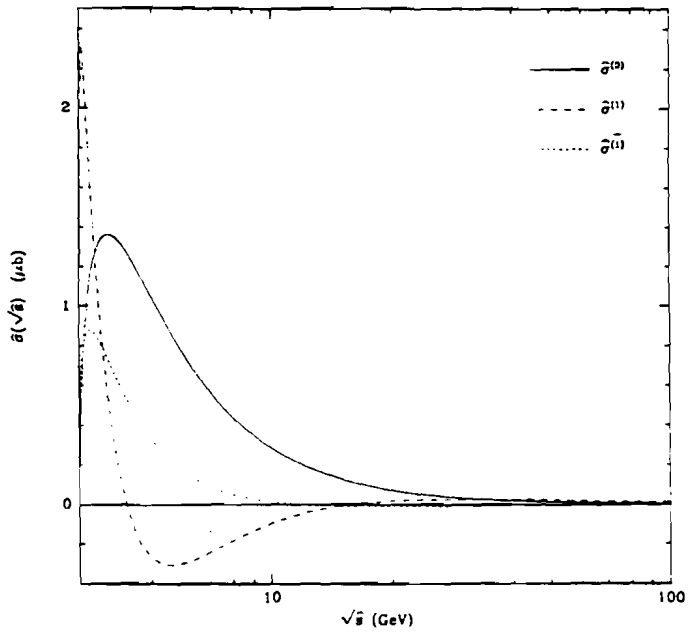

Figure 2.8: Quark-quark contributions to the cross section

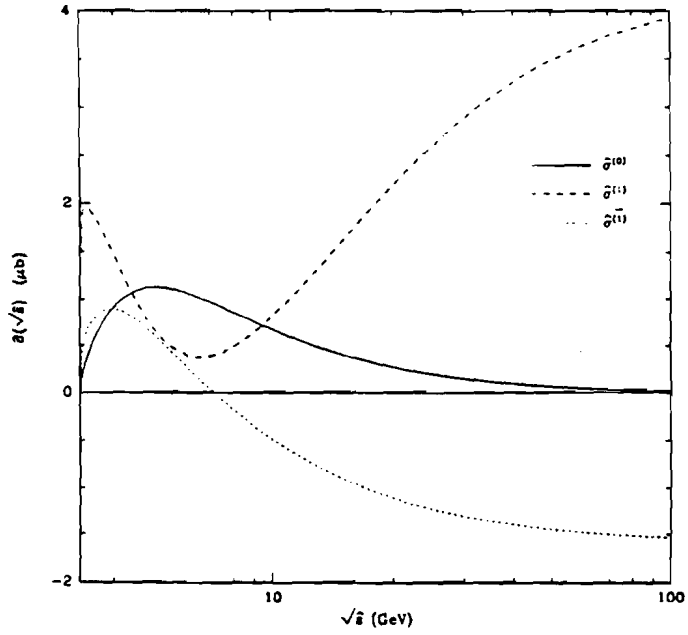

Figure 2.9: Gluon-gluon contributions to the cross section

order terms (or alternately the choice of renormalisation scale), and the pion and proton structure functions.

One way to estimate the error due to neglecting higher order terms is to examine the μ-dependence of the result. If the calculation was done to all orders in perturbation theory, the resulting cross section must be independent of the renormalisation scale μ. The variations in the finite order result as μ is varied over some reasonable range must be compensated by the higher order terms. The common choice among theorists is to choose μ to be the typical momentum scale of the process. For charm production, the average p_t^2 of a charm quark is $\sim m_c^2$ [Ell 89, Bar 88], so the typical $Q^2 \sim 2m_c^2$. Figure 2.10 shows the total $\pi^- p \rightarrow c\bar{c}$ cross section for $\mu^2 = m_c^2$ and $\mu^2 = 4m_c^2$, with $m_c = 1.5$ GeV. Note that there is approximately a factor of 2 difference in the predictions. Figure 2.10 also shows the predicted cross section using the EHLQ [Eic 84] structure functions for the proton.

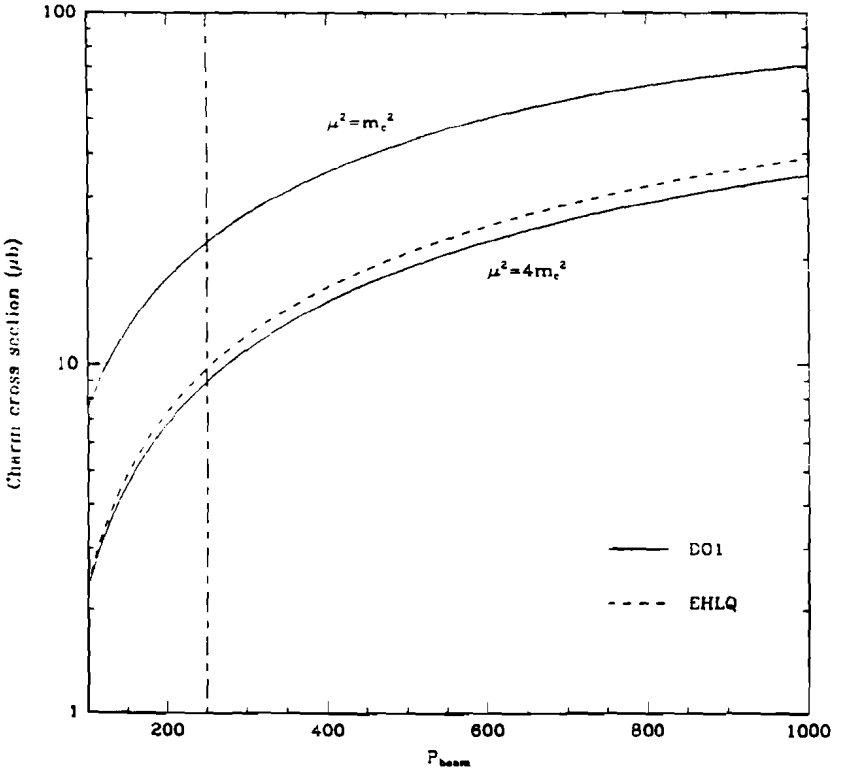

Figure 2.10: Third order estimates of the charm cross section for various renormalisation scales.

The uncertainty in the charm cross section due to the charm quark mass is shown

in Figure 2.11. Again, there is approximately a factor of 2 difference in the predictions as the mass is varied over its range.

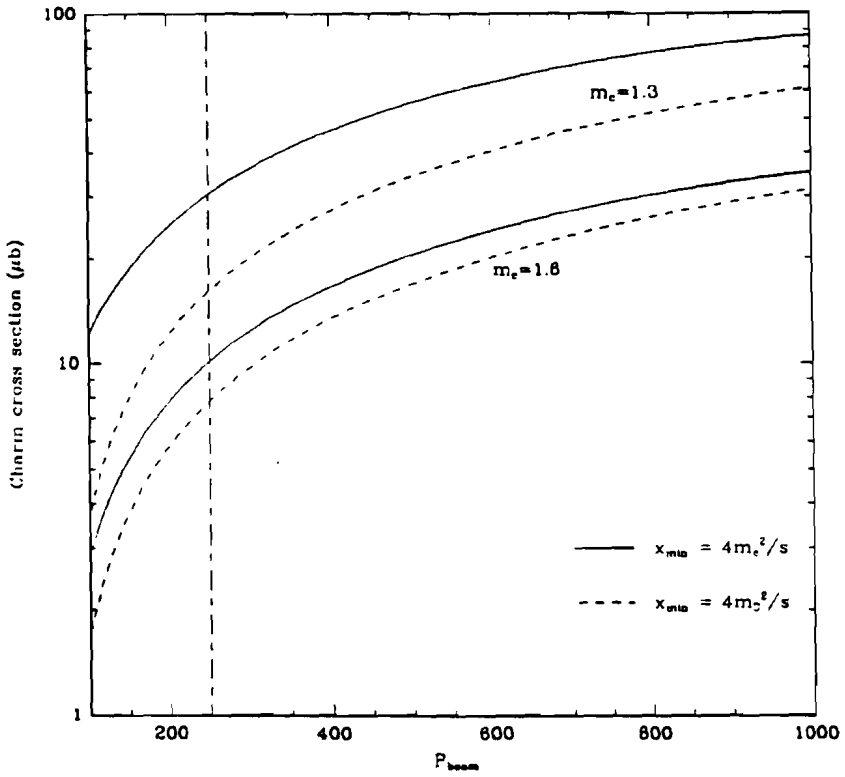

Figure 2.11: Third order estimates of the charm cross section for various charm quark masses.

2.1.3 Fragmentation

As stated above, fragmentation has no effect on the total $c\bar{c}$ cross section, but does affect the cross section for any particular product. The fragmentation function $D_c^H(z)dz$ shown in Figure 2.1 is defined as the probability of finding a hadron of type H in the range z to $z + dz$ among the products produced by the fragmenting c quark. There are several choices for the definition of z. The most common are:

z	=	E_H/E_c	(Energy Fraction)
z	=	p_{LH}/p_{Lc}	(Longitudinal momentum Fraction)
z	=	$(E_H + p_{LH})/(E_c + p_{Lc})$	(Light-cone variable Fraction).

The fragmenting of quarks is usually treated in a Monte Carlo program. Instead

of a vast number of D_c^H's (one for each possible hadron H), several approaches using only one, or just a few, functions have been developed. These can be categorized into three main types: independent fragmentation, cluster fragmentation, and string fragmentation.

As an example, in independent fragmentation each quark or gluon is assumed to fragment in isolation from all the others. A function $f(z)$ is given which defines the probability that a quark will radiate a fraction $(1 - z)$ of its momentum. A Monte Carlo of the fragmentation of quark q_0 with momentum p_0 proceeds roughly as follows [Bar 87]:

- z_1 is selected according to the distribution $f(z)$.
- A $q_1\overline{q}_1$ pair is selected (the different flavours can have different probabilities of occurring). The pair is given an energy fraction $(1 - z_1)E_0$ (or longitudinal momentum instead of energy, etc.), and the initial quark is now assigned a momentum of $z_1 p_0$.
- A small amount of p_t is added to the new quark, with the opposite amount going to the antiquark.
- The hadron $q_0\overline{q}_1$ is formed, and its mass and spin selected according to some fixed probabilities.
- The process is repeated for quark q_1, and so on, until the fragmenting quark's momentum becomes lower than a cutoff value.

One problem with independent fragmentation models is that at the end of the procedure there are loose quarks dangling around. Some prescription for combining them must be followed. They also do not conserve energy and momentum.

String fragmentation models do not have these problems. The quarks and gluons are arranged into colour singlets at the initial stage. A colour flux tube, or string, is set up to connect coloured partons. (It is thought that in QCD the lines of force connecting a quark and an antiquark are concentrated into a thin tube. This flux tube has a constant energy density per unit length, and so behaves like a string with constant tension.) In general, the partons at the ends of a flux tube will move apart. As they separate, the energy stored in the string increases, until there is enough to form a $q\overline{q}$ (or $qq\overline{q}\overline{q}$) pair from the vacuum. The string is split into two, with the new quark and antiquark placed at the ends of the new strings. This process is continued

until no more fragmentations are energetically allowed. The Lund group has a Monte Carlo based on this technique [And 83] which has proven to be the most successful of all models at fitting the observed fragmentation data.

All of the experiments mentioned in Chapter 1 which published charm cross section measurements have measured (or extrapolated to) the total D meson cross section. That is, they only detected open charm particles. When comparing this to a theoretical prediction, it is important to determine how much of the total $c\bar{c}$ cross section goes into open charm. We make the reasonable assumption that in any charm event which is produced with $\hat{s} < 4m_{D^0}^2$, the charm will form some sort of bound state (the D^0 is the lightest open charm meson).

If one uses an independent fragmentation model this is strictly true, because the charm quarks can only lose energy in the fragmentation process. If $\hat{s}$ is below the threshold given, the charm quarks will have energies less than m_{D^0}, and will not be able to fragment. The only recourse is to have the $c\bar{c}$ pair form a bound state.

This assumption is not strictly true for string fragmentation models. If a charm quark with less energy than is needed to form a D meson is coupled with a fast-moving light quark, it can be accelerated by the pull from the faster quark. Hence it is possible to boost a quark over the threshold so that it has enough energy to form a D. On the other hand, a quark just above the D threshold can be slowed so that it no longer has enough energy to form a D. Studies using the Lund Monte Carlo showed these effects to be negligible, and so we assume, as stated above, that the charm produced below the D threshold form bound states. Figure 2.11 shows both the predicted total $c\bar{c}$ cross section (solid line) and the total open charm cross section (dotted line) for $\pi^- p$ collisions.

2.2 The A-Dependence

The cross sections predicted by NDE are for hadrons incident on targets of single protons or neutrons. Most experiments use a nuclear target, however, and so a method of converting between a per nucleon cross section and a per nucleus cross section is necessary.

There is evidence that the structure functions of nucleons inside nuclei change slightly. This is known as the EMC effect [Ash 88]. Qualitatively, the change in the structure functions is shown in Figure 2.12. The plot shows the ratio of the structure function F_2^A for a nucleon inside a nucleus to that of a free nucleon, F_2^N. $F_2^N(x)$ (or

$F_2^A(x)$) is the experimentally measured quantity; its relation to the quark distribution functions is given in Eqn. 1.4.

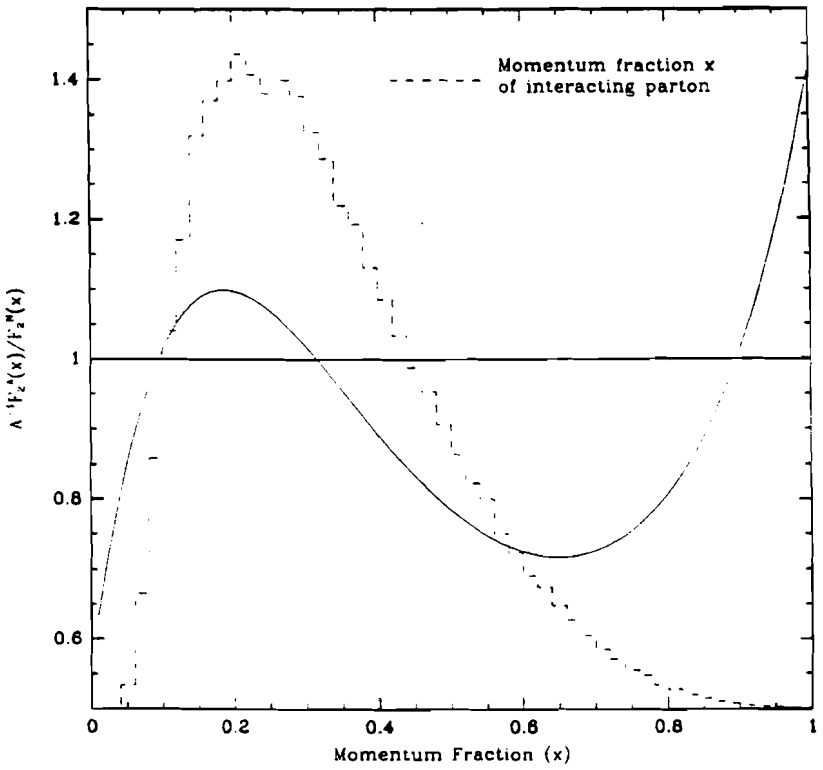

Figure 2.12: Schematic behaviour of $A^{-1}F_2^A(x)/F_2^N(x)$. (After Close [Clo 88].) The dotted curve is a Monte Carlo of the x of the interacting parton in $c\bar{c}$ production.

Models which describe this behaviour also predict a similar shape for the ratios of gluon distribution functions [Clo 89]. The depletion of the gluon and quark distribution functions at very low x leads to the prediction of *shadowing* for collisions dominated by this x region. That is, the cross sections for such hadron-nucleus (atomic number A) collisions are lower than are predicted by simply scaling the hadron-nucleon cross section up by a factor of A. The nucleons in the nucleus can be thought of as partially obstructing the beam from reaching nucleons behind them — hence the term shadowing. The lowest value of x at which the structure function ratio crosses through 1 moves to the right as the A of the material increases, and the shadowing becomes more pronounced.

Instead of using modified structure functions for each possible target material and then calculating a cross section for each, the effect is taken into account by introducing

an A-dependence parameter α. The cross section is calculated for collisions with a single nucleon, and then the *per nucleus* cross section is given by $\sigma_N = \sigma_0 A^\alpha$. Here σ_N is the per nucleus cross section, and σ_0 is the per nucleon cross section.

The total hadronic cross section at high energy is a process which is dominated by partons at very low x, and it is found that the exponent α is much less than 1 [Car 79]. For heavy quark production this is no longer true. The region of x which dominates depends on the beam energy. Superimposed on Fig 2.12 is the momentum fraction of the interacting parton from the target proton, obtained from a Monte Carlo of the $\pi^- p \rightarrow c\bar{c}$ interaction. At the beam energy used (250 GeV — the E769 beam energy) the typical x of an interacting parton in the target is ~ 0.2. Comparing the generated distribution with the structure function ratio leads to an expectation that α should be near 1 for charm production at this energy. If only a fraction of the charm cross section is selected, that at large x_F for example, then the parton distribution curve will be skewed, and values well below 1 can be obtained.

Chapter 3

The Beam

Fermilab experiment E769 took data during the fixed-target running period of 1987–88, using the Tagged-Photon Spectrometer (TPS) at the Proton East (PE) beamline. 400 million hadron-beam induced events were written to 10,000 9-track magnetic tapes, and then reconstructed over the course of two years. This chapter will describe the beamline, target, and tagging detectors which were used.

3.1 The Hadron Beam

The Tagged-Photon Spectrometer was fed by a 250 GeV hadron beam; this beam was created in two main steps. The first step was accomplished in the following way. Protons were accelerated to 800 GeV as follows: protons were accelerated to 750 KeV with a Cockroft-Walton, and then to 200 MeV with a linear accelerator (LINAC). They were then sent to the booster ring which increased their energy to 8 GeV, and then injected into the main ring which brought their energy up to 150 GeV. Finally, the protons were injected into the superconducting Tevatron, which accelerated them to 800 GeV. This whole process took about 40 seconds. Due to the structure of the RF cavities in the Tevatron, these primary protons were grouped into buckets about 2 ns long, with a separation between successive buckets of 19 ns. In the second stage, the protons were extracted and sent off to the various beamlines (Figure 3.1) during a 22 second spill. The PE beamline, on which the TPS was located, had a typical allocation of 1×10^{12} protons out of a total of $\sim 1 \times 10^{13}$.

These primary protons struck a 30 cm long Beryllium target located upstream of the spectrometer. Bending magnets and collimators selected out 250 GeV hadrons of a particular charge while the rest of the produced particles went into a beam dump. The estimated momentum spread of this secondary beam was ± 10 GeV. Approximately

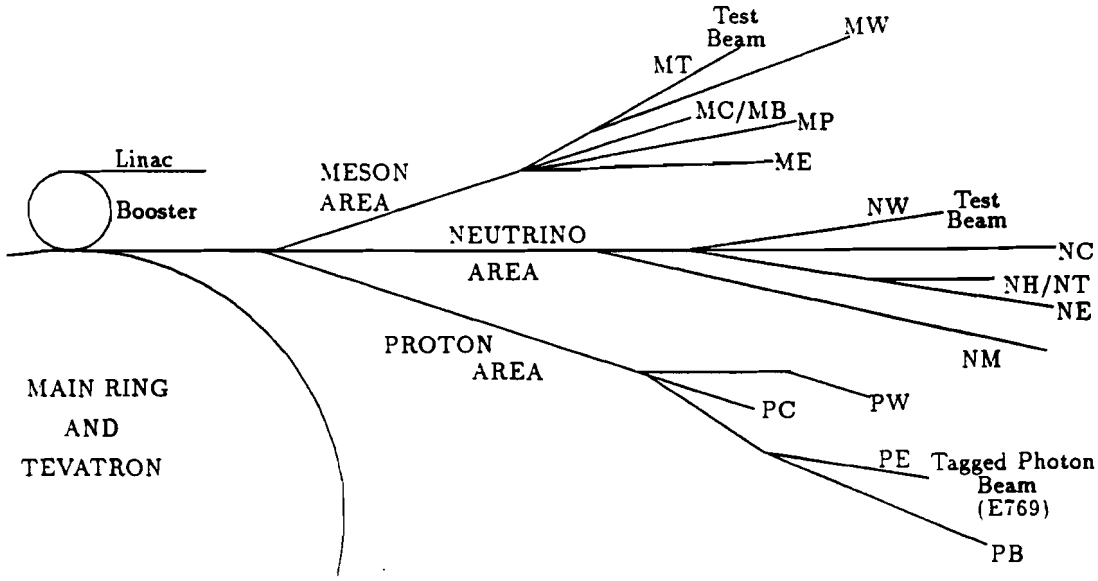

Figure 3.1: The Fixed target areas at Fermilab

150 M triggers were recorded with a negative hadron beam, and 215 M with a positive beam. The compositions of the beams were as follows. The negative beam contained 93% π^-'s, 5.2% K^-'s, and 1.5% $\bar{p}$'s. The positive beam was composed of 61% π^+'s, 34% p's, and 4.4% K^+'s. However, as will be described in Sec. 3.4, the fraction of kaon events written to tape was significantly larger than the fraction of kaons in the beam. The beam rate through the spectrometer ranged from $\sim 0.5 \times 10^6$ particles/sec for the negative beam to $\sim 2 \times 10^6$ particles/sec for the positive beam. The beam was far from uniform over the whole spill, however, and instantaneous rates were estimated to be as high as 4×10^6 particles/sec. The positive beam rate was higher than the negative simply because the primary particle was positive (proton), so more high energy positive particles were produced in the first interaction.

3.2 The Target

There are many factors which go into designing a good target. It must be thick enough to produce a reasonable number of interactions for the given beam rate, while representing as few radiation lengths as possible to reduce multiple scattering. For many experiments, the target's size is very constrained due to the geometric acceptance of the spectrometer. And, of course, the choice of materials directly affects

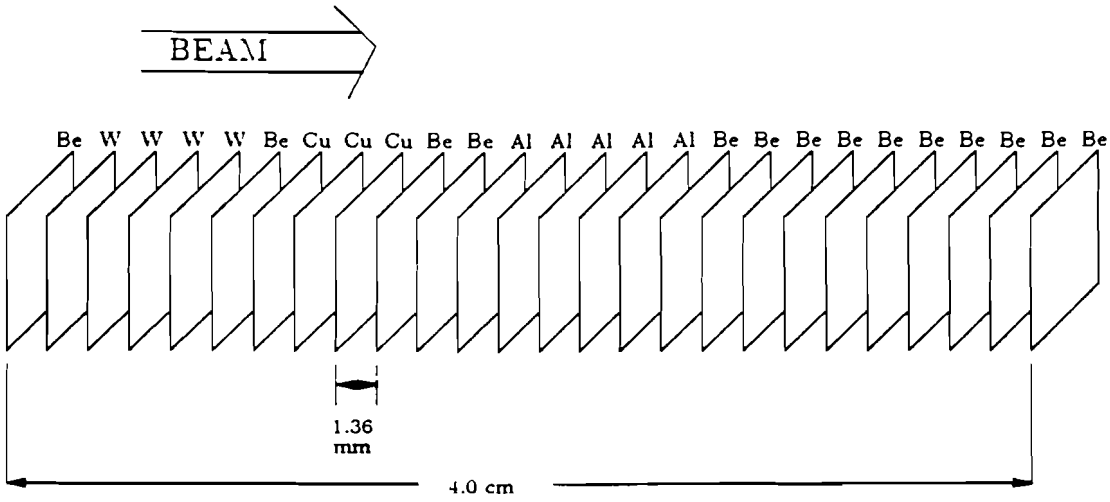

Figure 3.2: The E769 segmented foil target

the physics one can do. The E769 target was designed with the measurement of the atomic number (A) dependence of charm production in mind. It was constrained to be ≤ 4 cm long to maximize the acceptance of the Silicon Microstrip system (see Sec. 4.1.1), and about 5 cm wide due to the beam width. It consisted of 26 thin foils making a rough cube (2.5 cm $\times$ 2.5 cm $\times$ 4.0 cm). Four different target materials were used — beryllium, aluminum, copper, and tungsten. The foils ranged in thickness from $\sim$ 100 μm to $\sim$ 250 μm, and were separated by 0.136 cm thick annular paper washers. Figure 3.2 shows the arrangement of the foils. Since, for a given foil thickness, the typical multiple scattering angle increases with Z, the high-Z material was placed at the upstream end of the target. Target foils, as opposed to solid blocks, were chosen in an attempt to increase the resolution on the longitudinal (z) location of the primary interaction point in an event. The typical resolution in z of an event's interaction point is about 100–150 μm from the silicon telescope (Sec. 4.1.1), allowing the isolation of the foil in which the interaction occurred. Using the centre of the foil as the interaction point increases the resolution to *(foil width)*$/\sqrt{12}$, i.e. 30–70 μm. The typical z-resolution of a downstream decay was found to be 300–400 μm. The foil spacing was chosen to be about four times this value. It was hoped that any candidate for a downstream decay which occurred inside a target foil could be discarded as a probable secondary interaction. A larger foil separation would have been desirable, but would have meant lengthening the target past the acceptable limit.

All the analyses involved the longitudinal error on both the interaction vertex and any downstream decay vertex — and the latter always dominated, as explained above. Hence there was no real gain from assigning an interaction vertex to a specific foil; all that mattered was in which material it was located. For this reason the targets were grouped into target blocks for analysis purposes. That is, we consider all the tungsten foils as one target, all the copper foils as another, etc.; except for the beryllium. There were four Be foils placed next to tungsten and/or copper foils. Because the number of interactions in the adjacent high-A foils was so much larger than in these foils, the probability of misassigning the material in which the interaction occurred is quite large. To be safe, only the downstream Be was used in the A-dependence and cross section measurements. Table 3.1 shows the thicknesses, interaction lengths, and radiation lengths downstream of the centre, for each target material type.

Material	Total Thickness (cm)	Int. lengths	Avg. downstream % rad. len.
W	0.03829 ± 0.00079	0.00397	13.1
Cu	0.07607 ± 0.00030	0.00506	4.97
Al	0.12602 ± 0.00054	0.00321	1.45
Be	0.26041 ± 0.00249	0.00640	0.37

Table 3.1: Measured target parameters for foils used

3.3 Beam Counters

Plastic scintillators were used to define and count acceptable beam particles. Far upstream of the target were two 10 cm× 10 cm paddle counters (known as the TRD paddle counters after the detector they bracketed). Immediately upstream of the target were the Beam Spot and Halo counters, which were arranged as shown in Figure 3.3. There was a 9.5 mm radius hole in the Halo counter through which the beam was meant to pass. Light from these counters was collected by photomultipliers, whose output was sent to discriminators with thresholds set to be efficient for single particle detection. The trigger required that in-time signals were present from both the TRD paddle counter discriminators and the Beam Spot discriminator, with no signal present from the Halo counter. This ensured that the beam particle passed through the beam tagging devices, the centre of the target, and the silicon microstrip

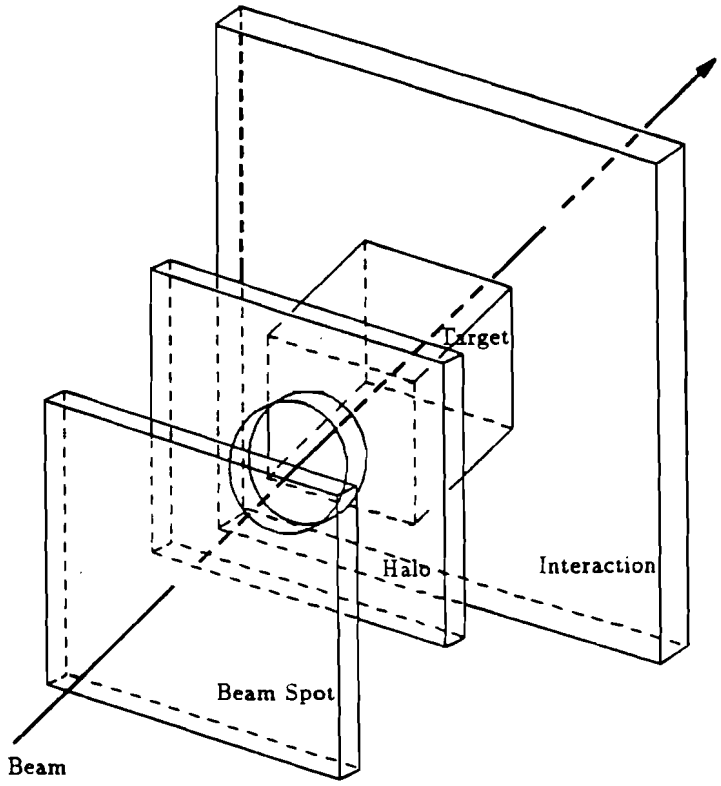

Figure 3.3: The Target Area Scintillators

system. A particle passing this criterion was called TRD Good Beam (TRDGB). A scaler with a resolution of 20 ns counted these particles, and formed the basic beam normalisation for all cross section measurements.

Just downstream of the target was another larger scintillator of area 11.5 cm^2, called the interaction (INT) counter, which was used to determine if the beam particle interacted in the target. Light from this scintillator was collected by a photomultiplier, and the signal was discriminated; but the threshold was set at the typical signal from three particles. All our physics triggers required an in-time signal from the INT counter along with TRDGB.

3.4 Beam Tagging

A question of some interest is what the relative charm cross sections are for various flavours of incident particles. This informs one about the gluon content of the particles and can also, as in the case of $K \rightarrow D_s$ vs. $\pi \rightarrow D_s$ at high x_F, be a signature for

leading-particle effects. To address this question, E769 added two detectors which allowed the flavour tagging of the beam particles. One was a Čerenkov counter called the DISC (for Differential Isochronous Self-focusing Čerenkov), and the other a transition radiation detector (TRD). The DISC was used to tag whether or not the beam particle was a kaon, while the TRD determined whether or not it was a pion. Particles not tagged as pions or kaons were identified as protons.

3.4.1 The DISC

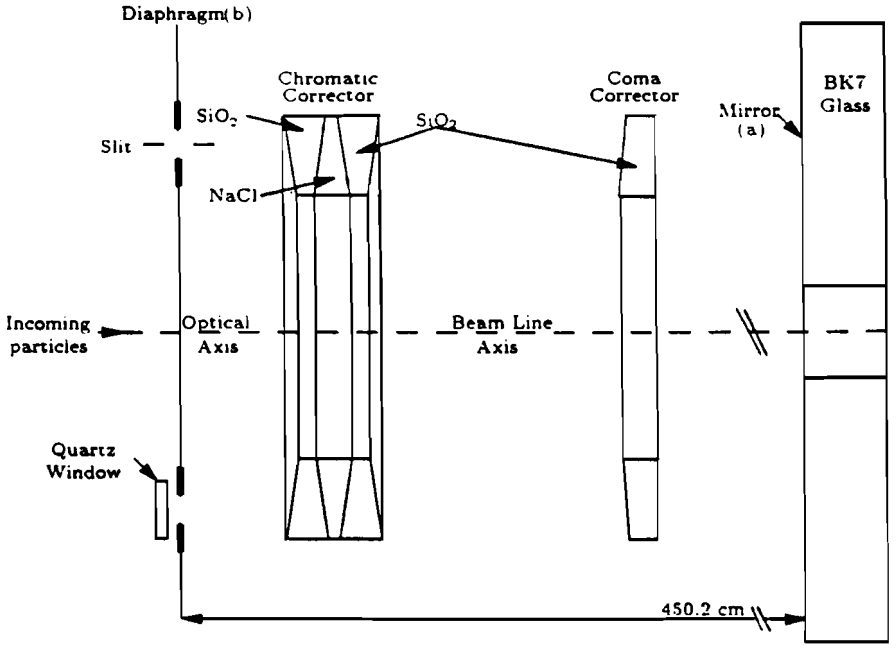

Figure 3.4: The DISC

The DISC (see Figure 3.4) is a precision device designed and built at CERN [Ben 73], which can distinguish particle types by the angle of emitted Čerenkov radiation. It was filled with helium, typically at 25°C and a pressure of ~123 psi. Recall that when a particle moves through a medium at a velocity which exceeds the speed of light in that medium, it emits Čerenkov light at a characteristic angle. This angle is given by $\theta_c = \cos^{-1}(1/\beta n)$, where β is the velocity of the particle, and n is the refractive index of the medium. Because of the mass difference between π's, K's and p's, at the given beam momentum of 250 GeV/c, the different particles have slightly different velocities, though all are very nearly 1. The difference in velocity between

K's and π's is $\sim 1.8 \times 10^{-6}$, while the K–p difference is $\sim 5.8 \times 10^{-6}$. These velocity separations cause each type of particle to emit Čerenkov light at slightly different angles, and the DISC exploits this small difference to distinguish between them. A beam particle travelling along the DISC's axis (see Figure 3.4) emits Čerenkov radiation at its characteristic angle. It is then reflected off the spherical mirror (a) and imaged onto the surface (b). The mirror images light emitted anywhere along the path to points with a fixed distance from the axis — thus the light from the particle forms an annulus on the surface (b). An annular slit with adjustable width is placed in this surface, which allows only light emitted at a specific Čerenkov angle through. Any light emitted with a different angle will hit the surface (b) either inside or outside of this annular slit. The geometry of the DISC is such that this accepted angle is 24.5 mrad. The Čerenkov angle for the particle to be tagged is tuned by changing the refractive index n of the helium. This is done by controlling the pressure: the higher the pressure, the higher n is. The relationship between the pressure of the gas p, the refractive index at STP n_0, the Čerenkov angle θ_c, and γ for the particle is:

$$(n_0 - 1)p = \frac{\theta^2}{2} + \frac{1}{2\gamma^2}.$$

Since θ is fixed by the geometry, one can see that higher pressure corresponds to lower γ, i.e. for a fixed energy beam to higher mass. The width of the annular slit can be adjusted to tune the efficiency/contamination ratio. The wider the slit, the more efficient the device is, but there is also more contamination from other types of particles. The light passing through the slit was collected by eight PMT's evenly spaced around the annulus. The signal was then amplified and discriminated. A particle was deemed to have a positive tag if at least four PMT's fired, with at least one from each of the four quadrants.

Two corrective lenses were also used by the DISC, as shown in Figure 3.4. The chromatic corrector compensates for the fact that the index of refraction of the gas varies with the frequency of the Čerenkov radiation. The coma corrector corrects for aberrations introduced by the mirror.

Periodically, special runs (called pressure curves) were taken, in which the pressure was slowly increased and the number of positive beam tags recorded. Figure 3.5 shows one of these curves. The very large peak at low pressure corresponds to the device tagging pions, the shoulder on this to kaons, and the isolated peak at high pressure to tagging protons. The pressure was usually set a small fraction higher than that of the kaon peak to reduce pion contamination. Using fits to these curves, along with

knowledge of the beam composition and temperature and pressure information, the efficiency for correctly tagging a kaon, and the contamination in the tagged sample, were calculated on a spill-by-spill basis. Typically, the tagging efficiency was 50% and the contamination was 1%.

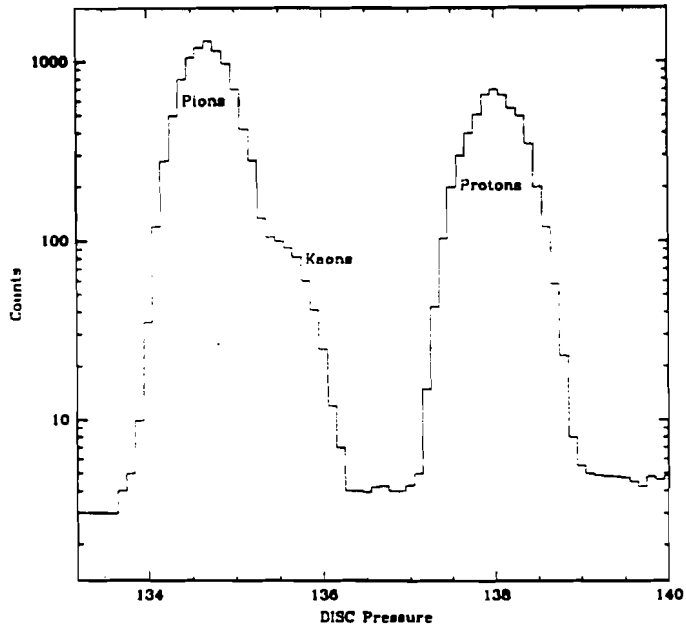

Figure 3.5: A DISC pressure curve

3.4.2 The Transition Radiation Detector

The second beam tagging device was the TRD, which was used during the positive beam run. It was not necessary during the negative run because its main function was to separate π's from p's, and the fraction of the negative beam which was $\overline{p}$ was very small.

Transition radiation (TR) is the radiation emitted when a charged particle traverses a boundary between two media with different dielectric constants. Since the electric field of the particle differs in the two media, an abrupt rearrangement of the field takes place when the particle crosses the boundary, which causes the particle to radiate [Jac 75]. The amount of transition radiation is given by $2\alpha\omega_p\gamma/3$, where $\gamma = 1/\sqrt{1-\beta^2}$, β is the velocity of the particle, and ω_p is the plasma frequency of

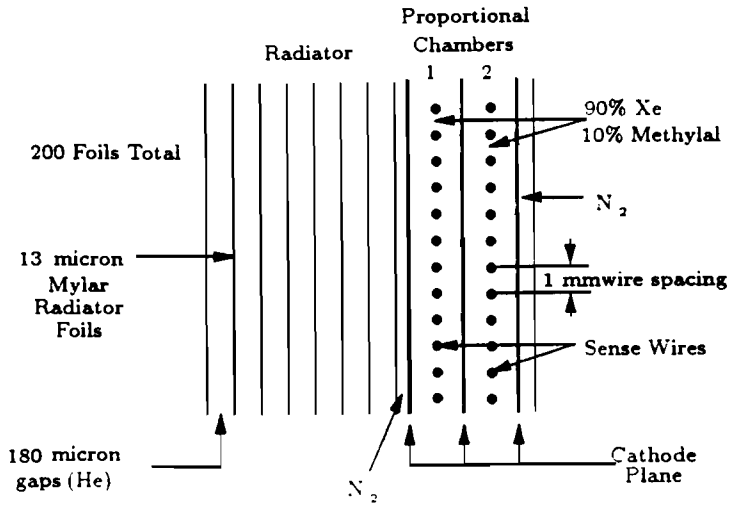

Figure 3.6: The TRD

the medium. At 250 GeV, $\gamma = 1791$ for pions, 506 for kaons, and 266 for protons; so pions emit the most TR, while protons emit the least.

The E769 TRD was made up of 24 identical modules, one of which is shown in Figure 3.6. Each module consisted of 200 13 μm foils of aluminized mylar which acted as radiators. The foils had a separation of 200 μm, which was maintained by sheets of bridal veil with holes cut in the middle to allow the beam to pass unhindered. The gaps between the foils were filled with helium. The TR emitted when a particle passes from the helium into the radiator foils is very forward, and tends to be in the X-ray region. Downstream of the radiator section of the module were two proportional wire chambers filled with a 90–10 mixture of Xenon and Methylal. Xenon was chosen, as opposed to a more common gas such as argon-ethane, because it has a very large absorption cross section for X-rays. The space between radiators and chambers was filled with N_2. Each module had 64 wires in the proportional chambers, whose signals were combined and sent to an amplifier-shaper-discriminator. The threshold was set to pass photons with energies above 4 KeV. In addition to TR, there is a background signal from energetic knock-on δ-ray electrons. The efficiency for detecting such δ-rays was found to be about 10%/plane in studies using a Ru_{106} source. Since γ_{proton} is so low, the protons produce very little TR, and any signals detected are of the background δ-ray type. The particle tagging was based simply on the number of planes which fired. Since protons only produce δ-rays, and the efficiency for

detecting this kind of ray is relatively small, only a few planes should fire. However, pions also produce TR, which the detector has a much higher efficiency for detecting, so many more planes fire. Figure 3.7 shows the plane count distribution for beam particles which were not tagged as kaons by the DISC. Both distributions are clearly present. This technique was checked by setting the DISC to tag protons: in these runs only the peak at low plane count was present. Table 3.2 gives the pion and proton tagging efficiencies and contaminations vs. various plane count cuts for a specific run. Similar plane count histograms were made for every run, and fitted with two binomial distributions. From these histograms, particle ID probabilities, efficiencies, and contaminations were computed, along with the accompanying errors.

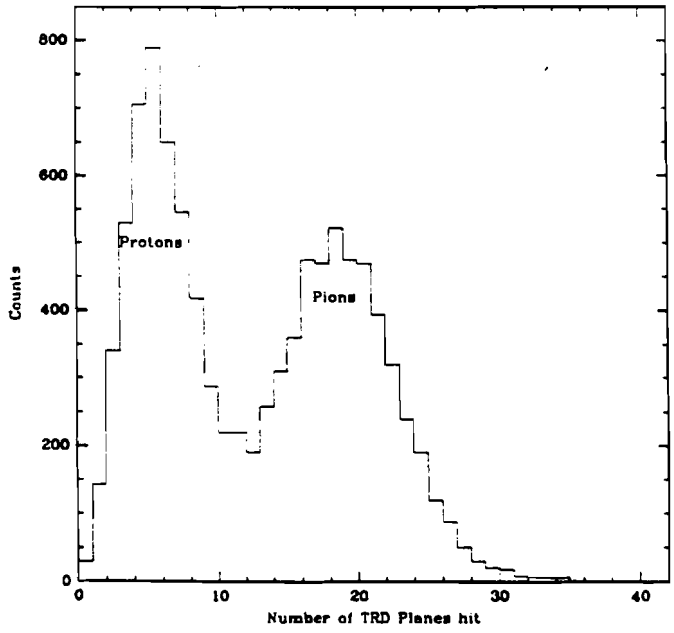

Figure 3.7: TRD plane count distribution

3.5 Beam Tracking

Since the incident beam was made up of charged particles, it was possible to measure the trajectory of each individual beam particle. It was hoped that this would help identify the location of the primary interaction vertex in the case of multiple vertex candidates, and also reduce the transverse error on the vertex position by including

No. of TRD planes which fired	Pion Efficiency	Proton Contamination	Proton Efficiency	Pion Contamination
≥ 8	94.6%	3.0%	-	-
≥ 10	86.8%	2.0%	-	-
≥ 12	73.3%	1.9%	-	-
≤ 6	-	-	86.5%	3.5%
≤ 7	-	-	92.4%	5.7%
≤ 8	-	-	95.1%	9.7%

Table 3.2: TRD efficiencies and contaminations

it in the vertex fit. To this end, ten new planes were added upstream of the target. There were eight Proportional Wire Chambers (PWC's) grouped in two assemblies located ~31 m upstream of the target, and two 25 μm pitch silicon planes located 13 cm upstream of the target. The PWC assemblies consisted of X, Y, X', and W view planes, where X' also measured in the X-direction, but was offset by 1/2 a wire spacing from the first X plane. The W axis was at 30° relative to the X axis. Each plane consisted of 64 wires with a separation of 1 mm, and were filled with Argon-CO_2. The two silicon planes (see Sec. 4.1.1 for details on the planes) measured X and Y views. The PWC's provided two points on the beam particle's trajectory which, along with the silicon's very accurate (~7 μm resolution) x and y positions and long lever arm, meant that good position and angle information was available. Unfortunately, there was a problem with the grounding of the silicon planes, which tended to make them very noisy. To combat this the gain was turned down, making them fairly inefficient (~70%). This meant we only had tracking information with both x and y hits ~50% of the time. Further, there was still a significant amount of noise, so there were often multiple hit candidates in the silicon. The PWC tracking did not have sufficient resolution to distinguish between silicon candidates, giving rise to many possible beam track trajectories. It was felt that the extra complication of using beam track or partial beam tracking information outweighed the gains, and so it is not used in the analysis presented here.

Chapter 4

The Spectrometer

The Tagged-Photon Spectrometer (TPS) is a typical two-magnet, large-acceptance, general purpose spectrometer, shown schematically in Figure 4.1.

It consists of 11 silicon microstrip planes, 35 drift chamber planes, two large-aperture magnets, two threshold Čerenkov counters, an electromagnetic calorimeter, a hadronic calorimeter, and a muon detector. This chapter will briefly describe these components.

4.1 Tracking

The two main advantages that fixed target experiments have over collider experiments are their high luminosity and the fact that the produced particles are usually moving very fast in the lab frame. One of the salient characteristics of heavy quark events is the appearance of two vertices — the primary, or interaction vertex, and a secondary, or decay vertex, at which the particle with the heavy quark decayed. Typically, $c\tau$ for the decaying particle is $\sim 100-300$ μm. However, since in a fixed target environment they have a high momentum (typically 50 GeV for E769), their path length in the lab frame, $\gamma c\tau$, is often several millimeters. This allows one to reject events which do not have a well separated secondary vertex; this cut is, in fact, the most powerful. Of course, in gaining these benefits, the high centre of mass energy of colliders is lost, and the tracking region is much more congested.

4.1.1 The Silicon Microstrip Detectors

The importance of the advent of silicon microstrip detectors (SMD's) to heavy quark physics can hardly be overstated. Before their use, charm experiments with several tens of events were common; now samples of several thousand are the norm. These

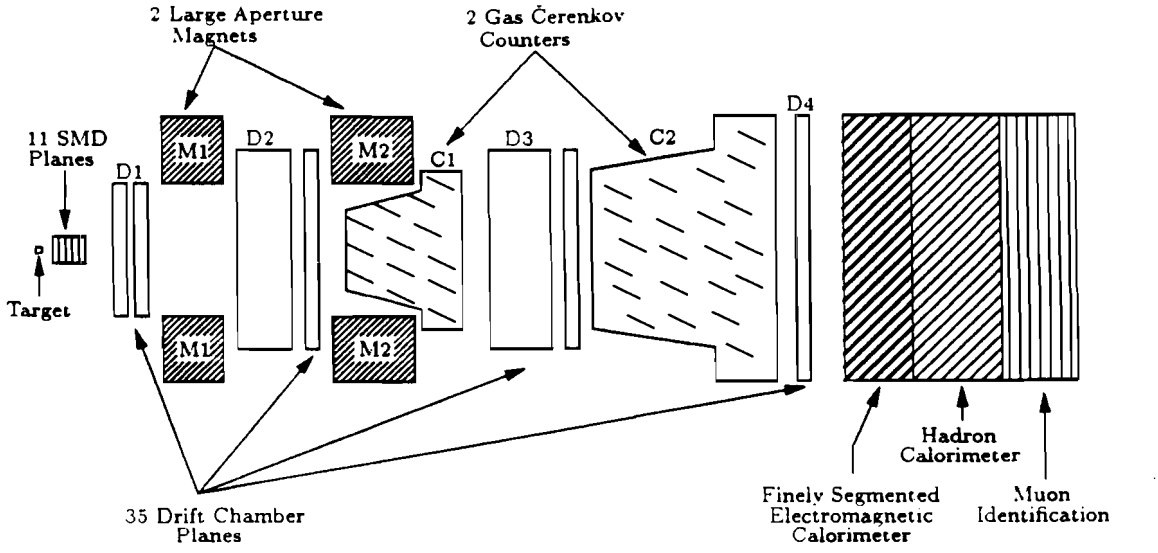

Figure 4.1: The Tagged Photon Spectrometer

detectors were developed during the 1980's by Kemmer *et al.* [Kem 80], and used successfully by NA11 at CERN. The SMD system is what enables one to resolve the two vertices which occur in charm events, as described above.

SMD Principles

An SMD, shown in Figure 4.2, consists of a substrate of Aluminum, on which is a thin layer of arsenic, followed by a relatively thick (300 μm) wafer of silicon. On top of this are strips of boron alternating with SiO_2. On each of the boron strips is another strip of aluminum. The silicon detectors used by E769 had a strip spacing, or pitch, of either 50 μm or 25 μm. Each of the aluminum-boron-silicon-arsenic-aluminum strips is turned into a reverse bias p-i-n diode. When a negative voltage is applied to the boron (p-type material), holes in the n-type silicon wafer drift towards the boron, while electrons move towards the n-type arsenic. This creates a volume of net positive charge in the silicon due to the left-over immobile lattice atoms. This zone is depleted of all free charge carriers, and is therefore called the depletion zone (see Figure 4.3).

When a minimum ionizing particle passes through the detector, it excites electron-hole pairs. Because of the small band gap in silicon, the average energy needed to make such a pair is only ~3.6 eV, compared to, for example, 30 eV to make an

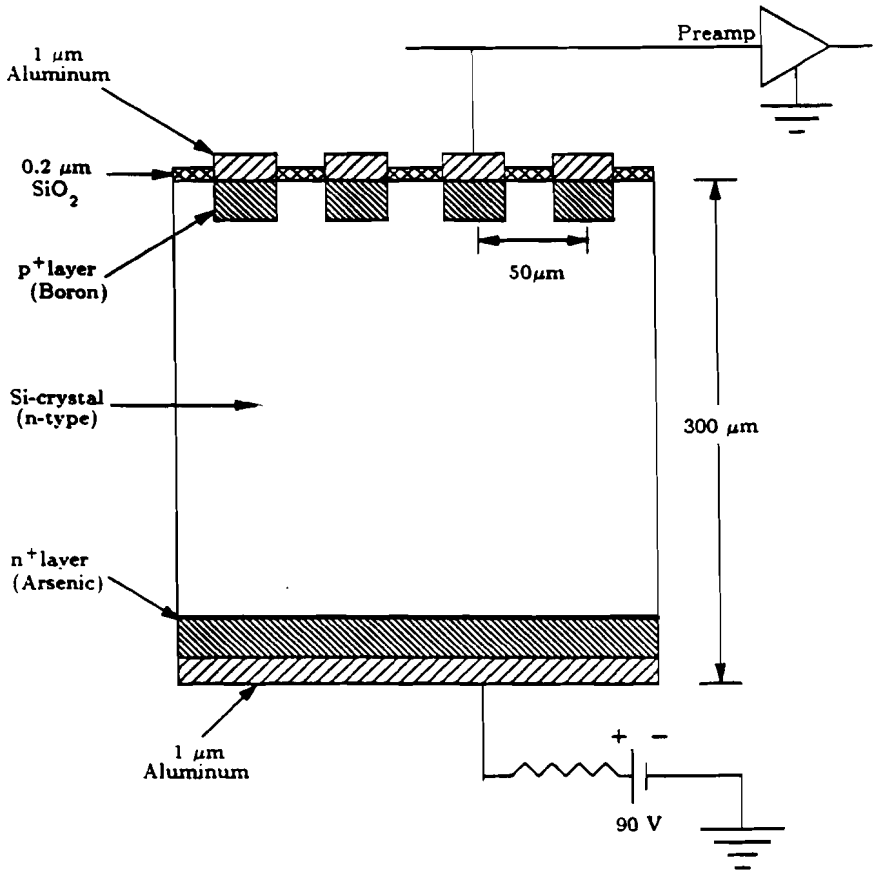

Figure 4.2: Cross Section of an SMD plane

ion pair in argon. In addition, the high density of the silicon gives rise to copious electron-hole pair production. A minimum ionizing particle passing through a 300 μm silicon detector typically produces 24,000 of these pairs, compared to about 3 ion pairs produced in the same thickness of argon-ethane (a standard drift chamber gas). The electric field in the wafer causes the electrons to drift to the n-type arsenic, while the holes move towards the p-type boron. The holes, which have a drift time of $\sim$10 ns, are collected at the aluminum strip, forming the signal which indicates the passage of a particle. The electrons are not used.

The E769 SMD's

E769 used a total of 13 SMD's: two upstream of the target, and 11 downstream, as shown in Figure 4.4. The planes were arranged into two doublets, one upstream and

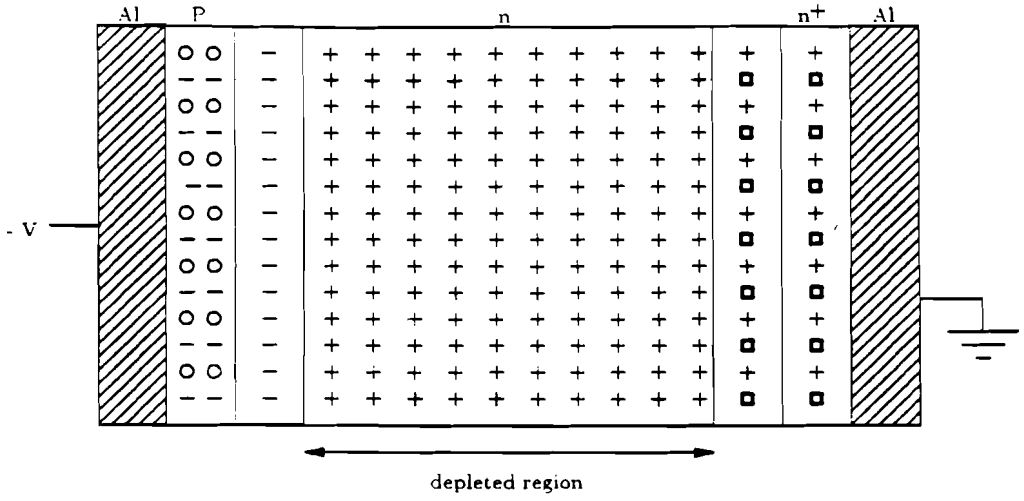

Figure 4.3: A Single SMD strip

one downstream, measuring X and Y coordinates, and three triplets which measured X, Y and V coordinates (V is at 20.5° to the vertical). Table 4.1 summarizes the characteristics of the planes.

The 25 μm pitch planes were, in fact, made up of both 25 μm and 50 μm strips. The central 384 strips were 25 μm pitch, with 152 50 μm pitch strips on either side. The angular acceptance of the SMD's was about 100 mrad.

Silicon planes have the admirable feature of being very efficient (typically 90–95%) while having low noise rates. Table 4.1 gives the efficiencies, noise rates, and percentage of hits which are singles (related to the amount of cross-talk) for the various planes. There were, unfortunately, two problems with the new systems (SMDA and SMDB). First, as mentioned in Sec. 3.5, these planes were very noisy due to inadequate grounding. To combat this the bias voltages were turned down, resulting in the lower efficiencies shown. Second, the z-alignment constants for the downstream (SMDB) planes were incorrectly calculated. This was propagated through the reconstruction code, and so the efficiency of these planes for reconstructed tracks was lower than the true plane efficiency. These numbers are shown in brackets in Table 4.1, although they only represent average values. (Tracks which had very small angles are affected less by shifts in z than high-angle tracks.) Fortunately, the pattern recognition program did not use these planes; they were only used as confirming hits and to "reduce" the errors on the track parameters. It was again fortunate that such a tight

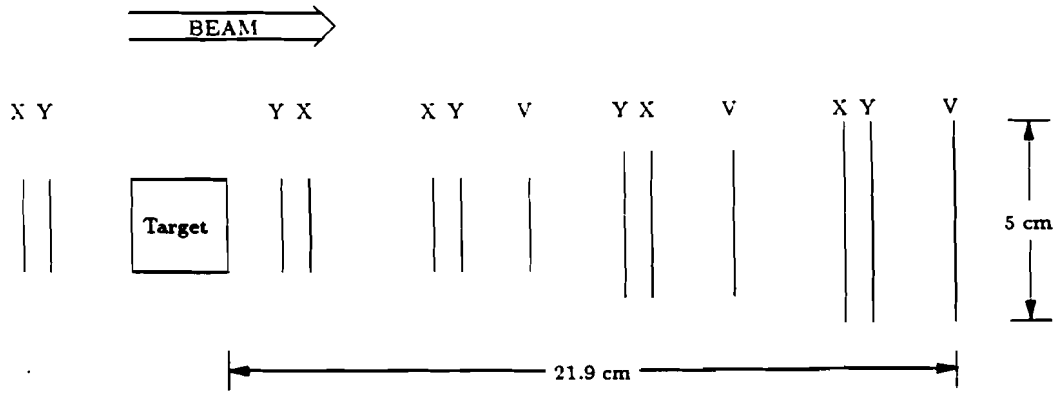

Figure 4.4: The E769 SMD systems

SMD assembly	A	B	1	2	3
Area (cm×cm)	2.5 × 2.5	2.5 × 2.5	2.6 × 2.6	5.0 × 5.0	5.0 × 5.0
Pitch (μm)	25/50	25/50	50	50	50
Instrumented strips	384	688	512	768	1000
Coordinates measured	X,Y	Y,X	X,Y,V	Y,X,V	X,Y,V
Avg. efficiency	60%	55(90)%	89.5%	89.5%	92.0%
No. noise hits	0.6	2.0	1.0	1.9	2.2
% single hits	79.4	75.0	85.4	85.0	75.9

Table 4.1: E769 SMD Characteristics

cut was put on the conditions for the inclusion of a hit from these planes in a track that they could not affect the track parameters too drastically. However, indications show that with correct alignment our background levels could be reduced by a factor of 2. In the following rough calculations we will assume for simplicity that the tracks contained no hits from the new SMDB planes.

Resolution

The intrinsic resolution on the measurement of the position at which a particle passes through a silicon detector or PWC of strip (wire) spacing d is given by $\sigma_{intrinsic} = d/\sqrt{12}$. This gives a minimum possible transverse resolution on hit positions of $\sim$ 14 μm. Other effects such as cross-talk, inefficiencies, delta-rays, etc. can increase

this value. Its measured value was found to be ~ 16 μm.

The reconstruction code parameterized tracks by five numbers: two intercepts (x_0, y_0), two slopes ($s_x \equiv p_x/p_z$, $s_y \equiv p_y/p_z$), and a momentum p. The resolution on a reconstructed track's intercepts was governed not only by the intrinsic resolution of the three planes, but by the multiple scattering introduced largely by the planes themselves, and also by the angular resolution. That is, $\sigma_i^2 = \sigma_{fit}^2 + \sigma_{multiple}^2$, where σ_{fit}^2 is the error on the intercepts from the (least-squares) fit to the hits, and $\sigma_{multiple} = 50$ μm$/p$(GeV) is the error introduced by multiple scattering. For a system of N equally spaced planes with separation d (first plane at $z = 0$), all with the same intrinsic resolution $\sigma_{intrinsic}$, we have

$$\sigma_{fit}^2 = \frac{4N-2}{N(N+1)}\sigma_{intrinsic}^2,$$

so $\sigma_{fit}^2 = 15$ μm for three planes. Note that multiple scattering only becomes a problem for tracks with momenta below 5 GeV. Hence for most tracks $\sigma_i \simeq 15$ μm.

Of more interest than the single track transverse resolution, however, are the longitudinal and transverse resolutions on vertices. To estimate the longitudinal resolution, consider a two track vertex, with the x-intercepts of the tracks given by x_{0i}, and the slopes given by s_{xi}. For simplicity, we will only deal with the track in 2 dimensions. The point of intersection of the two lines is given by:

$$z = \frac{x_{02} - x_{01}}{s_{x1} - s_{x2}},$$

and hence the resolution on the z position is given by:

$$\sigma_z^2 = \frac{1}{(s_{x1} - s_{x2})^2}(V_{x_{01},x_{01}} + 2V_{x_{01},s_{x1}} + V_{s_{x1},s_{x1}} + V_{x_{02},x_{02}} + 2V_{x_{02},s_{x2}} + V_{s_{x2},s_{x2}}),$$

where the V's are the covariance matrices for tracks 1 and 2. The resolution on the tracks' slopes was found to be $\sigma_{s_x} \approx 0.12 + \frac{3.3}{p(GeV)}$ mrad. For N equally spaced planes as above, the off-diagonal elements of the covariance matrix for the track are:

$$V_{x_{01},s_{x1}} = \frac{-6\sigma_{intrinsic}^2}{dN(N+1)},$$

and so for $N = 3$ is $-\sigma_{intrinsic}^2/2d$. For E769's silicon system, $d \sim 10$ cm, and z is between -5 cm and 0 cm. Putting in a typical opening angle of 50 mrad and setting $z = -5$ cm. we find $\sigma_z \simeq 560$ μm, with the dominant contribution coming from $V_{x_{01},x_{01}}$. Since this calculation only used the xz view of the track, we have another measure of z from the yz view, which will reduce the total error by about $\sqrt{2}$, so

$\sigma_z \simeq 390$ μm. The typical two-track longitudinal error was measured to be 420 μm. For n tracks one expects the error to go like $\sigma_n(z) = \sigma_n(z)/\sqrt{n-1}$, which is borne out by the data.

The distance a charmed particle travels in the lab frame is often on the order of several millimeters; thus the SMD system provides a means of measuring both the production vertex and the decay vertex. This proved to be crucial for the analysis.

4.1.2 The Drift Chambers and PWC's

The tracking downstream of the interaction region and momentum analysis were accomplished with the aid of 35 drift chambers, divided into four stations (D1, D2, D3, and D4), and two PWC's. As shown in Figure 4.1, D1 and the PWC's were located just upstream of the first magnet, M1. Along with the SMD system, they provided a measurement of a track's initial trajectory. D2 was located between M1 and the second magnet, M2. It provided a track segment which was matched up with the segment from D1. Once the track segments were matched up, the angle the track was bent through was calculated, giving the track's momentum. Tracks which were energetic enough not to be bent out of the spectrometer by the magnets passed through D3 and D4, which were located downstream of M2. These tracks had an even more accurate momentum measurement.

The chambers were grouped into assemblies, each of which contained three or four planes. D1 contained two assemblies with planes which measured X, X', U, and V coordinates (where X' is offset from X by 1/2 the wire spacing, and U and V are at $\pm 20.5°$ to the vertical). D2 and D3 contained four assemblies with X,U, and V planes, while D4 contained a single X,U,V triplet of planes. Hence each assembly could completely determine the (x,y) coordinates of any charged track where it intersected that assembly. The main pattern recognition used information from D1 and the silicon microstrip planes. Since the silicon provided the only Y-view information, two additional PWC's which provided extra Y-view measurments were added. This helped reduce the number of false tracks at an early stage of the reconstruction, which increased the speed and accuracy of the analysis. Table 4.2 summarizes the Drift Chamber characteristics.

Each chamber consisted of a sense plane, which was made up of alternating sense wires and field shaping wires, sandwiched between two cathode planes. The cathode wires were held at a large negative voltage relative to the sense wires ($\simeq -2.3$ kV),

DC Station	1	2	3	4
Dimensions (cm × cm)	160 × 120	230 × 200	330 × 200	550 × 300
Cell size (cm)	0.476	0.953	1.588	31.75
No. of planes	8	12	12	3
Resolution (μm)	350	300	300	800
Avg. Efficiency (%)	90.3	89.9	82.5	65.5

Table 4.2: E769 Drift Chamber Characteristics

while the field shaping wires were at a slightly less negative voltage ($\simeq -2.0$ kV). The chambers were filled with a 50–50 mixture of argon-ethane, with an additional 1.5% ethanol which helped quench gas ionization, and slowed chamber aging.

When a charged particle traverses the gas, the gas becomes ionized, and the electrons drift towards the sense wire. In the E769 configuration, the drift velocity was fairly constant across a drift chamber cell, and was typically ~ 50 μm/ns, except for near the edges of the cell and near the sense wire. When an electron gets very near the sense wire, a charge avalanche occurs, causing much more charge to be collected than the original number of electrons liberated. This gain was roughly 2×10^5.

The charge collected on the sense wires was sent to Lecroy DC201 and Nanomaker N-277C amplifier-discriminator cards. These were in turn read out by the CAMAC-based Lecroy 4290 TDC system operating in common stop mode, which did the time digitization. For a detailed description of the digitizing logic, see [Men 86].

During the E691 run, which used a photon beam, the central parts of the chambers were damaged due to the high pair rate in this region. In E769, since the beam was charged, ionization of the gas in the cell(s) through which the beam passed occurred constantly. This led to a space charge buildup, as the ionization from the previous beam particle had not yet been quenched before the next particle's passage. These two effects led to dead regions in the center of each chamber, called DC holes. These regions' efficiencies were parameterized as inverted asymmetric gaussians (they were asymmetric because our beam centre did not precisely coincide with the region damaged in E691). These holes tend to reduce the reconstruction efficiency of charm events with high x_F, since such events are more forward, and thus it is more likely that one of the tracks from the decay will go into the hole region and be lost. The widths of the holes were: 0.35 cm (D1), 0.73 cm (D2), 2.85 cm (D3), and 7.6 cm (D4).

4.1.3 The Magnets and Momentum Determination

The TPS contained two large aperture magnets which provided a total transverse momentum kick of 530 MeV, which facilitated track reconstruction and allowed momenta to be determined. The more upstream magnet, M1, had an angular acceptance of ±240 mrad horizontally, and ±120 mrad vertically, while the magnet further downstream, M2, had acceptances of ±120 mrad and ±60 mrad. The magnets were roughly the same size, but because M2 was much further downstream its angular acceptance was much lower.

The fields in the magnets were in the $-y$ direction. From the equation for the force on a particle of charge q moving in a magnetic field, we get:

$$d\vec{p} = qd\vec{l} \times \vec{B}.$$

where $d\vec{p}$ is the momentum change, and $d\vec{l}$ is the path traversed. For E769, particles' trajectories were very close to being along the z-axis, so we take $d\vec{l} = d\vec{z}$. Hence:

$$d\vec{p} = qdl \cdot B_y \hat{x}$$

or,

$$\Delta p_t = q \int B_y \cdot dl.$$

M1 ran with a current of 2500 amps, which corresponded to an $\int B \cdot dl$ of 0.71 T-m, i.e. (with $q = 0.2998$ GeV/T-m) a p_t kick of 213 MeV. M2 ran at a current of 1800 amps, which corresponded to an $\int B \cdot dl$ of 1.07 T-m, or a p_t kick of 321 MeV. The magnetic field had been accurately mapped out in a previous experiment (E516); however, an overall fudge-factor was added to make sure that the masses of particles came out right. This factor was tuned to ensure that the measured K_s mass was within 0.1 MeV of its accepted value.

To estimate the momentum resolution, we note that the angle through which a particle's trajectory is bent by a magnet is given by $\theta = p_t/p$, where p_t is the kick given by the magnet. Hence, $\Delta p/p = \Delta\theta/\theta$. To estimate $\Delta\theta$, we consider a series of N equally spaced planes with total length l (so that the interplane spacing is $l/(N-1)$) and an intrinsic resolution of σ_0. From a standard least-squares fit, we find that $\sigma(\theta) = \sigma_0/l\sqrt{12/N}\sqrt{(N-1)/(N+1)}$. Since measuring the bend angle involves

measuring the track angle both upstream and downstream of the magnet, there is a contribution to $\Delta\theta$ from both sets of chambers. Thus $\Delta\theta = \sqrt{\sigma^2(\theta_u) + \sigma^2(\theta_d)}$, giving

$$\frac{\Delta p}{p} = \frac{\Delta\theta p}{p_t} \simeq \frac{p}{p_T}\sqrt{12(\frac{\sigma_{u0}^2}{N_u l_u^2}(\frac{N_u - 1}{N_u + 1})^2 + \frac{\sigma_{d0}^2}{N_d l_d^2}(\frac{N_d - 1}{N_d + 1})^2)}.$$

We estimate this resolution due to M2, since the case of M1 is more difficult as one must include the SMD's. The value of p_t for M2 is 321 MeV (as stated above), $l = 118.5$ cm, and $N = 12$ for both D2 and D3, giving $\Delta p/p \approx 0.1p\%$, with p in GeV. In fact, the momentum resolution from the tracking for particles which passed through one magnet (i.e. M1 only) was measured to be $0.1\%p(\mathrm{GeV})$, while the resolution for particles which passed through both M1 and M2 was $0.05\%p(\mathrm{GeV})$. In addition to this term, there was a contribution from multiple scattering. Recall that the average multiple scattering angle goes as $\Delta\theta_{ms} \sim 1/p$, which leads to a constant term in the momentum resolution. This term was found to be 0.5%, so the full expressions for the momentum resolutions for one and two magnet tracks were:

$$\frac{\Delta p}{p} = \sqrt{(0.1\%p(GeV))^2 + (0.5\%)^2} \qquad \text{(one magnet)}$$
$$\frac{\Delta p}{p} = \sqrt{(0.05\%p(GeV))^2 + (0.5\%)^2} \qquad \text{(two magnet)}.$$

Again, we see that the term due to multiple scattering is unimportant for tracks with momenta larger than 5 GeV.

To estimate the mass resolution, we consider a particle of mass M undergoing a two-body decay into particles of mass m_1 and m_2, with momenta p_1 and p_2, and opening angle θ in the lab frame. For high energy particles $p \simeq E$, and we have $M^2 \simeq m_1^2 + m_2^2 + 2p_1p_2(1 - \cos\theta)$. Further, since the opening angle is small, we can approximate $1 - \cos\theta$ by $\theta^2/2$, and $M^2 \simeq m_1^2 + m_2^2 + p_1p_2\theta^2$. Hence we have:

$$\frac{\sigma(M)}{M} = \frac{1}{2}\sqrt{(\frac{\sigma(p_1)}{p_1})^2 + (\frac{\sigma(p_2)}{p_2})^2 + 4(\frac{\sigma(\theta)}{\theta})^2}.$$

The momentum terms typically dominate the mass resolution. The measured resolution for $D^0 \rightarrow K^-\pi^+$ decays was 11 MeV.

4.2 Particle Identification

The ability to distinguish whether a given track was produced by a pion, kaon, or proton provided a very powerful cut with which to select true charm decays over

background events. This was accomplished with the aid of two threshold Čerenkov counters, described below.

4.2.1 The Čerenkov Counters

A particle traversing a medium with a refractive index of n will emit Čerenkov light if the velocity is greater than the velocity of light in the medium, which is c/n. Translating this to momentum, and setting $c = 1$, we find that a particle of mass m emits Čerenkov light only above a threshold momentum of

$$p_{th} = \frac{m}{n(1 - \frac{1}{n^2})^{\frac{1}{2}}}.$$

In our case, $n \approx 1$, so this becomes $p_{th} = m/\sqrt{2(n-1)}$.

The two counters used in E769 were filled with different gas mixtures, which meant that a particle's momentum threshold was different in the two. The most upstream counter (C1) was filled with nitrogen, which had $n - 1 = 2.9 \times 10^{-4}$. The momentum thresholds in C1 were thus 6 GeV for pions, 20 GeV for kaons, and 38 GeV for protons. The downstream counter (C2) was filled with a mixture of 80% helium and 20% nitrogen, which had $n - 1 = 8.6 \times 10^{-5}$. The thresholds in C2 were 9 GeV for pions, 36 GeV for kaons, and 69 GeV for protons. By checking which of the counters detected light, it is possible to distinguish between particles types. For example, pions can be distinguished from kaons and protons if their momentum is between 6 and 20 GeV; pions, protons, and kaons can all be distinguished if their momentum is between 20 and 36 GeV; and protons can are distinguishable from pions and kaons for momenta between 36 and 69 GeV. Table 4.3 shows the state of the two Čerenkov counters for each particle type in various momentum ranges, where C indicates Čerenkov light was emitted by the particle, and $\overline{C}$ indicates it was not.

Even though electrons and muons are indistinguishable from pions using these techniques, most electrons and muons come from decays of kaons and pions. As such, their momentum spectrum is peaked at very low values and falls quite rapidly, so the contamination at momenta greater than 6 GeV is small.

The Čerenkov light was collected by arrays of spherical mirrors, which reflected the light into light collecting mirrored structures called Winston cones. At the base of these were RCA 8854 photomultiplier tubes (PMT's), whose outputs were sent to Lecroy 2249 ADC's for digitization. C1 used 28 mirrrors, arranged as shown in Figure 4.5a, and because of space constraints used two mirrors to direct the light into

Momentum (GeV)	pion	kaon	proton	ϵ or μ
0–6	$\overline{C}_1\overline{C}_2$	$\overline{C}_1\overline{C}_2$	$\overline{C}_1\overline{C}_2$	C_1C_2
6–9	$C_1\overline{C}_2$	$\overline{C}_1\overline{C}_2$	$\overline{C}_1\overline{C}_2$	C_1C_2
9–20	C_1C_2	$\overline{C}_1\overline{C}_2$	$\overline{C}_1\overline{C}_2$	C_1C_2
20–36	C_1C_2	$C_1\overline{C}_2$	$\overline{C}_1\overline{C}_2$	C_1C_2
36–38	C_1C_2	C_1C_2	$\overline{C}_1\overline{C}_2$	C_1C_2
38–69	C_1C_2	C_1C_2	$C_1\overline{C}_2$	C_1C_2
69+	C_1C_2	C_1C_2	C_1C_2	C_1C_2

Table 4.3: Čerenkov Counter States vs. Particle Momentum (From [Men 89])

the Winston cone, as shown in Figure 4.6. C2 used 32 mirrors, arranged as shown in Figure 4.5b. The mirrors ranged in size from 15 cm × 25 cm to 95 cm × 50 cm.

The code which generated the actual particle identification probabilities first looked at all tracks found by the reconstruction code, and generated the expected amount of light collected by each mirror for the different mass hypotheses. It then checked the mirrors, and assigned probabilities for each of the hypotheses based on the outcome. Occasionally, light from two nearby particles was collected by the same mirror, which greatly complicated the process. If a particle's momentum was not in a range which allows identification, or if there was too much overlap from nearby tracks to disentangle the light from each individual particle, the algorithm assigned *a priori* values for the probabilities. These numbers (independent of momentum for simplicity) were based on the known fraction of tracks in typical events which were pions, kaons, etc. The *a priori* probabilities for a particle to be of a given type were: electron (0.02), muon (0.01), pion (0.81), kaon (0.12), and proton (0.04).

4.3 Calorimetry

The TPS included both electromagnetic and hadronic calorimeters. In E769 these were only used in the trigger, and so will be described fairly briefly.

4.3.1 The Electromagnetic Calorimeter

The electromagnetic calorimeter, known as the SLIC (for Segmented Liquid Ionization Calorimeter), consisted of 60 layers of 0.03 cm thick lead alternating with 1.27 cm

C1 Mirror Array

13	9		2			10		14
11	7	5	3	1	4	6	8	12
25	21	19	17	15	18	20	22	26
27	23		16			24		28

C2 Mirror Array

15	11		2				12			16
13	9	7	5	3	1	4	6	8	10	14
29	25	23	21	19	17	20	22	24	26	30
31	27		18				28			32

Figure 4.5: The Čerenkov Mirrors

thick layers of liquid scintillator. It represented about 20 radiation lengths of material and 2 interaction lengths. The scintillator layers were alternately in U, V, and Y views. and were divided into 3.175 cm wide strips. The angular acceptance was $\sim \pm 66$ mrad in the vertical direction, and $\sim \pm 133$ mrad in the horizontal. The fractional energy resolution was found to be $\Delta E/E \simeq 21\%/\sqrt{E}$, where E is measured in GeV. For more details on the SLIC, see [Sum 84].

4.3.2 The Hadronic Calorimeter

Downstream of the SLIC was the Hadrometer — a hadronic calorimeter made up of 18 layers of 2.54 cm thick steel alternating with 0.95 cm thick layers of plastic scintillator. The scintillator layers consisted of 14.48 cm wide strips which read measured X and Y views alternately. There were 6 interaction lengths in the hadrometer, which meant there were a total of 8 between the two calorimeters. Thus there was little leakage of the showers out of the back of the detector. The energy resolution of the

Chapter 5

The Data Acquisition System and Trigger

One of the principle upgrades to the E691 detector was an improved Data Acquisition (DA) system, motivated by the fact that the charm yield from experiments with hadron beams is a factor of 10 lower than from those with photon beams.

At E691 energies (90–180 GeV) the total hadronic γp cross section is about 100 μb and the charm cross section is 0.6 μb. This means that with a trigger simply requiring the presence of hadrons in the final state, a charm yield of 1 per 160 events can be obtained. For a 250 GeV pion beam the total inelastic cross-section is about 20 mb, but every event has hadrons in the final state. The charm cross section is about 15 μb (see Sec. 9), so the charm yield is only 1 per 1300 events, down by a factor of $\sim$ 10 from the photon beam yield. E691 has a total charm sample of $\sim 10^4$ events [Men 89], so, all other factors being equal, E769 expected $\sim 10^3$ charm events.

As stated earlier, the E769 beam rate was typically 10^6/s, implying an interaction rate of $\sim 2 \times 10^4$/s, or 4×10^5/spill. The E691 DA system could handle 100 events/s, or 2×10^3/spill, so the amount of charm in the final sample would have been severely limited by the DA speed. The total number of charm events written to tape can be increased by either developing a new trigger which enhances the fraction of charm in accepted events, or building a faster DA system. The experiment chose the latter: a new DA system was designed to handle 3–4 times the data rate of the old system. So, even though the charm yield is down by a factor of $\sim$ 10 for hadroproduction over photoproduction, by taking four times as many events we hoped to come within a factor of two of E691's sample size. Since the highest statistic hadroproduction experiment at the time had only several hundred events, the projected 5,000 events would be a major breakthrough.

5.1 The Data Acquisition System

In every DA system there are three basic components: front end digitizing, event building, and event storage. Also, in many large, modern DA systems the trigger has become an inseparable component, often being implemented in several stages between the digitizing and final output. The two most important characteristics of any DA system are the throughput (speed at which data can be taken) and the dead time (fraction of time the system is unable to accept events due to the processing of a previous event). The design goal for the E769 DA system was to achieve a throughput of 300 events/s (1.2 Mb/s), with a dead time of 30%. This section describes the system implemented, which had a throughput of 450 events/s (1.8 Mb/s) at a dead time of 25%.

A short description of the E691 DA system will also be given for comparison with the new system, since it was representative of DA technology in 1985.

As has been pointed out in Chapter 4, the additions made to the existing detector were minimal. From a DA standpoint, the new components added only $\sim$ 1,000 new channels to the existing 20,000. The actual digitizing modules were largely the same as used for E691. These front end systems were all Camac based, and consisted of Lecroy 2280 ADC's for the calorimeters, Lecroy 2249 ADC's for the Čerenkov counters, Nanomaker Nanoscanners for the SMD system, and Lecroy 4299 TDC's for the Drift Chambers, as well as assorted latches and scalers. Table 5.1 shows the main systems, as well as the digitizing time for each, showing that one would have to replace most of the major digitizing systems to get any significant gain in throughput. Due to time constraints the collaboration decided to forego this, and concentrate instead on speeding up the rest of the data flow. The main technique used was to parallelize the system, as will be explained below.

Detector group	Digitizing module	# channels	Dig. Time	Readout time
Calorimeters	Lecroy 2280 system	546	400μs	600μs
SMD's	Nanoscanners	9,000	300μs	200μs
Drift Chambers	Lecroy 4299 system	6,000	650μs	1200μs

Table 5.1: Digitizing/Readout times for various E769 front-end modules

Figure 5.1 shows the data flow in the E691 DA system. After a trigger occurred (t=0) the front-end modules started digitizing the event. When this was finished

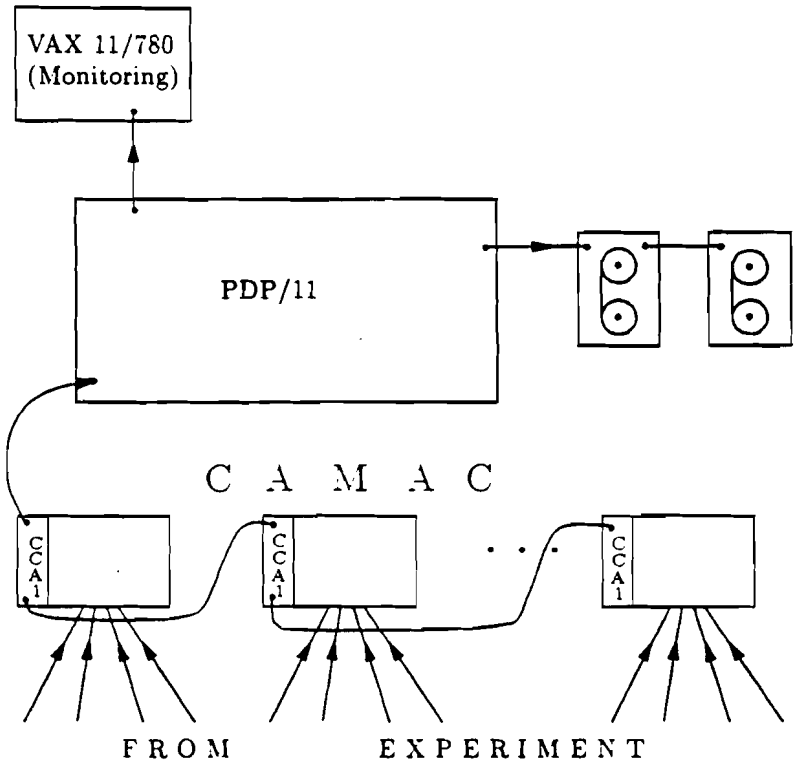

Figure 5.1: The E691 Data Acquisition System

(t=600 μs) the crates were read out one by one through A2 controllers connected to a PDP-11 via a Jorway 411 Camac Branch Highway driver. No extra event building was necessary as the PDP assembled the event as it was being read in. Once the whole event was in place (t=3 ms), it was written to magnetic tape. Then the whole system was reset and readied for the next event. Clearly, the link in this chain which most severely limits the data throughput is the slow serial readout of the six Camac crates. At a data rate of 100 events/s, an event arrives approximately every 10 ms, so if the processing of one event renders the DA inactive for 3 ms, the dead time is 30%.

Figure 5.2 shows the E769 data flow. It begins in the same manner as the old system, with the addition of a new crate to help even out the system's readout time. However, once the event had been digitized it was no longer read out over one serial data path. The readout was parallellized into seven paths, allowing each crate to be read out simultaneously, reducing the readout time by roughly a factor of 5. This was accomplished by means of two special electronic modules, one which resides in

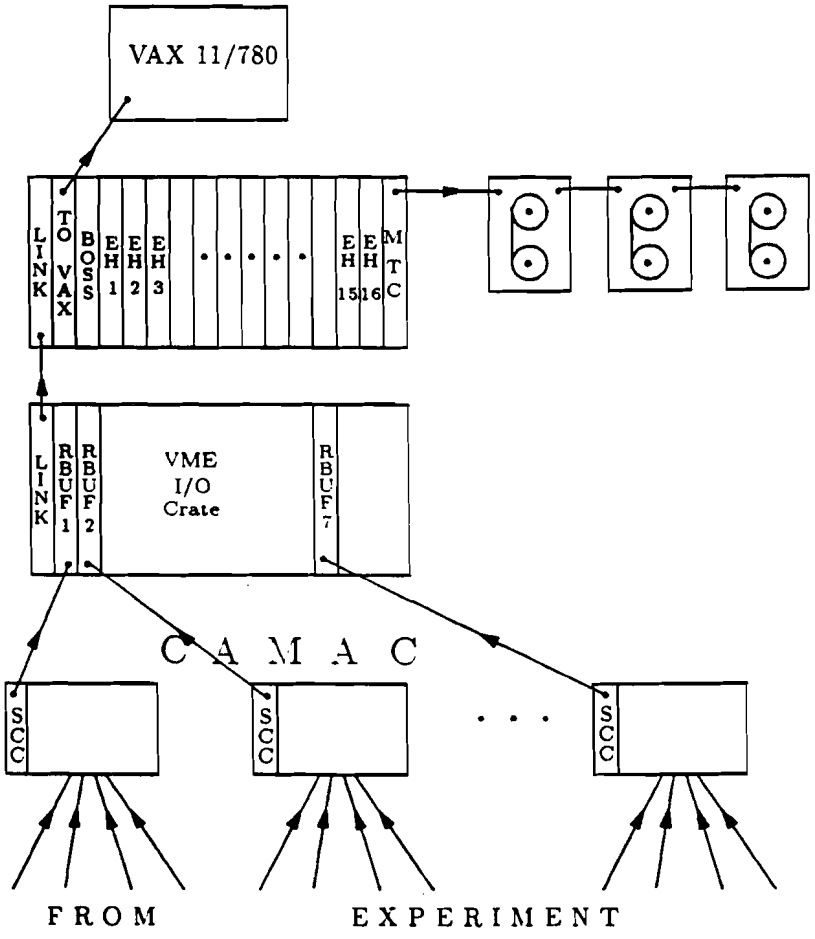

Figure 5.2: The E769 Data Acquisition System

Camac, and one which resides in VMEbus. They were designed and built by the E769 DA group, the Fermilab Physics Department, and the Fermilab Electronics Group. The new Camac-resident module was called the Smart Crate Controller, or SCC. The SCC is a Motorola 68000 based auxillary Camac crate controller, which works in conjunction with the old A2 controllers. Instead of one central computer reading out all the crates via the Camac Branch Highway, the new DA used seven local controllers, each with a microprocessor containing the instructions on how to read out the modules in its crate.

The SCC's have a front panel RS-232 port which was connected to a Vax 11/780, which had high level control of the DA system. The instructions on how to read out each crate (readout lists) were downloaded to the SCC's at the start of every run. Provision was made to have 32 different possible readout lists, corresponding to 32

different trigger types. The SCC's were programmed in 68000 assembly code via a macro package called CALEX, written by the Fermilab Computing Department. It allowed anyone familiar with the basics of Camac to write readout lists for the SCC's without knowing assembler. A 6-pin connector on the front panel was used to input 32-bits of trigger information and a strobe which initiated the readout sequence. After a strobe was detected, the other 5 lines were decoded into a trigger word, and the readout list corresponding to that trigger was executed. The data being read from the digitizing modules were not stored in the SCC itself, but was immediately sent out a front panel port to an RBUF (see below). A further advantage of the SCC's was their ability to operate at bus cycle speeds of both 1 μs, which is the Camac standard, and 600 ns. It was found that all of our main digitizing systems could be read out in 600 ns cycles. This is to be compared with the typical 1.5–2 μs needed to read out a 16-bit word via the Branch Highway. With the factor of 5 in speed due to parallellizing the data paths, and the factor of 2 due to the increased readout speed of the modules, a factor of about 10 was gained in the readout time over the older systems.

Each SCC's data port was connected to a dedicated, dual-port, double-buffered memory module called a Readout Buffer, or RBUF. These are simple VMEbus modules which have two separate 32K chunks of memory. Their purpose was to store data arriving from the SCC's, which were later read out by an ACP (see below) module via VME. Having two blocks of memory allowed one event to be flowing into one of the blocks, while the previous event was being read out from the other.

The heart of the DA system was a microprocesser developed by the Advanced Computer Project (ACP) group at Fermilab called the ACP. It is a single width VME module consisting of a Motorola 68020 and 2 Mb of memory. The principle VME crate of the DA system contained 17 of these ACP's, as well as a VME Resource Module (VRM) which handled the bus arbitration and related tasks, and a Branch Bus Controller and Branch Bus-VME interface, which linked the VME environment to a Vax 11/780 via a DR11W. It also contained Ciprico magnetic tape controller (MTC) which handled the tape writing and a Bus-extender module which linked the main VME crate to the VME I/O crate which contained the RBUF's. The ACP's were divided into two classes, consisting of one Boss ACP, which was responsible for managing all the other VME modules, and 16 Event Handlers (EH's), which actually did the work. At any given time, the Boss designated two of the Event Handlers as Grabbers, the other 14 were Munchers. The two Grabbers built events from the

seven event fragments in the RBUF's and placed them in a large (1.4 Mb) circular input buffer in their on-board memory, while the Munchers formatted and processed events previously grabbed and placed them in output buffers. The Boss periodically polled the Event Handlers to determine the amount of available space in each EH's input and output buffers, and, if necessary, assigned two new EH's as Grabbers and switched the old Grabbers to Munchers. The Boss also handled the flow of events onto magnetic tape and to an online event pool located on the Vax. It assembled a list of memory locations of processed events in output buffers, and sent this to the MTC. The tape controller had the ability to scatter-gather the data written, so assembling all the events into one block was not necessary. The events were written to one of three STC 2925, 100 ips, 6250 bpi tape drives. At a typical data rate of 1.5 Mb/s, the DA system collected 30 Mb in a 20 second spill (out of a 60 second cycle). Since the drives could only write 0.6 Mb/s, almost 2/3 of the events were stored in the EH's input buffers (total capacity of 22.4 Mb), which were then processed and written to tape during the 40 seconds of interspill.

The user interface to the system, which provided the highest level of control, was the System Controller program which ran on the Vax 11/780. Through this program one had the ability to start and end runs, pause the DA, and monitor the system's performance. It was also the interface to the online event pool used to monitor the detector, and reported any errors found by the Boss in the hardware.

The reliability of the DA system is of paramount importance in any experiment. One very useful feature of the E769 system was that the SCC's had the ability to send pre-programmed data out the front panel port under the 68000's control. This proved to be very useful in finding low-rate errors in the system. Once these were fixed, no data errors were found in over 10^9 bytes sent through the system.

5.2 The Trigger

E769 used several different triggers which can be divided into three main classes: physics triggers, calibration triggers, and non-beam triggers. The non-beam triggers were used between spills to monitor detectors, get ADC pedestal values, etc. Special runs using the calibration triggers, such as beam-track only events, muon events, etc., were used to measure efficiencies for trigger components, to align detectors, and so on. The physics triggers were of two basic types: minimum-bias interaction (INT) triggers, and large transverse energy (E_t) triggers.

About 7% of all events were taken with the INT trigger. It was the simplest trigger — it demanded that the beam particle pass through the TRD paddle counters, the Beam Spot counter, and the hole in the Halo Counter (see Sec. 3.3). It also required, in coincidence with these signals, a signal from the Interaction scintillator which was at least as large as the average signal from three minimum ionizing particles passing through the counter.

The remainder of the events were E_t triggers of one type or another. The transverse energy of an event was calculated approximately using the calorimeters. A weighted sum of the signals from each of the calorimeters' modules was made using a network of resisitors. (The resistors' values went like $\sin\theta$, where θ was the angle between the z-axis and a line connecting the center of the module to the target.) The summed signal was fed to two separate discriminators. The first discriminator's threshold corresponded to E_t value of approximately 5.5 GeV (called the E_t threshold), while the second's threshold corresponded to an E_t of about 9.0 GeV (called the E_{tB} threshold).

The main triggers all required that the event pass one of the E_t thresholds, as well as satsify all the requirements for the INT trigger. For negative beam data, the triggers were as follows:

- E_t: Event passes E_t threshold (these are prescaled)
- E_{tK}: Event passes E_t threshold, and is identified as a kaon by the DISC (no prescaler)
- E_{tB}: Event passes E_{tB} threshold (these are prescaled).

The regular E_t events were prescaled in order to enrich the sample of kaon-induced events written to tape.

For positive beam data, there was an additional requirement on the E_t and E_{tB} triggers (not on E_{tK}), which was that no other beam particle arrive within 150 ns before or after the triggering beam particle (though multiple particles in the same bucket were allowed — we did not have the ability to veto these). This was done to ensure that the TRD functioned correctly. The drift time in the TRD's wire chambers was fairly long, requiring a 100 ns gate width on the charge collection. If another particle traversed the detector in this time, extra hits may have developed, which would have decreased the detector's ability to separate pions from protons. If the

incident particle was identified as a kaon, the TRD was not required, and so no such requirement was needed. This requirement was known as the beam killer.

Chapter 6

Data Reconstruction

Once all the data are on tape in raw event format, it is necessary to turn these events into actual particle 4-momenta, trajectories, particle type probabilities, etc. This was done in a four-stage reconstruction program.

6.1 The Reconstruction

The first stage, called PASS0, simply ran through several thousand events to determine ADC pedestals, generate useful distributions such as TRD plane count histograms, etc. Also, at the conclusion of PASS1 and PASS2 (see below), it made a summary file containing such statistics as: average number of tracks, average number of vertices, plane efficiencies, and so on, which were useful for locating time periods when the detector was not functioning correctly.

The second stage, called PASS1, performed all the pattern recognition. First, track segments were found in the region upstream of the first magnet using hit information from the SMD's, D1, and the PWC's. These were swum through the magnets and linked to hits in D2, D3, and D4, which also provided the momentum measurement. After this was done, a search was made for remaining tracks in the drift chambers only (for example from $K_s \rightarrow \pi^+\pi^-$, which typically decay downstream of the SMD's).

The third stage, called PASS2, contained the Čerenkov analysis, which generated particle probabilities for all tracks, the calorimeter reconstruction, which located and fitted showers, and the vertexing, which found possible vertex combinations among the tracks. The vertex algorithm first formed a two-track vertex which passed a χ^2 cut, and then added in any tracks which kept the χ^2/DOF below 2.5. Another two-track vertex was searched for among the remaining tracks, and the process was continued until no more vertices were found. The average number of vertices in an

event was 1.5.

Finally, the event was output in a compressed Data Summary Tape (DST) form (although some data was reconstructed to the PASS2 stage, and DSTed later). This provided a compression of about 4 from the raw data.

The entire process took approximately 20 seconds on a 1 MIP machine (such as a Vax 11/780). About 1/2 the data was reconstructed on several ACP farms consisting of a total of between 50–200 processors, corresponding to 35–140 MIPs worth of computing power. See Sec. 5 for details on the ACP computer. The other half of the data was reconstructed on four Silicon Graphics 240-D compute servers, which represented a total of 240 MIPs of computing power. It took about one year to reconstruct the entire data sample of 370 million events.

Chapter 7

The Monte Carlo

An absolutely essential part of extracting real physics from the immensely complex detectors used in HEP experiments is a good Monte Carlo (MC). This is a computer simulation of the detector, along with some sort of simulation of the physical processes involved in the production and/or decay of the particles being studied. Because the detectors used have less than perfect efficiency and acceptance, the events in which a charm decay can be reconstructed represent a small portion of the actual number of events which contain charm quarks. The MC provides the means to extrapolate back from the measured quantities to the actual physical quantities.

The E769 MC was divided into two separate programs: the Generator and the Digitizer. The Generator can be divided into two logical components. The first contains the code to generate charm events, which includes simulating a hard interaction that produces a $c\bar{c}$ pair, hadronization of these quarks and other beam fragments into hadrons, and the decay of unstable particles. The second contains a simulation of the detector's response to the passage of the generated particles. These two aspects are discussed below.

The Digitizer converted the output of the Generator into the same format as a Raw Data tape. It also contained the code which generated noise hits and cross talk in the detector, and took into account the Drift Chamber, SMD, and PWC plane efficiencies.

7.1 Event Generation

The event generation process had three basic phases — the selection of the charm quark pair's kinematic properties, the modelling of the underlying event, and the fragmentation and subsequent decay of the quarks and beam fragments from the

previous phases.

For the first phase, the reaction at the parton level was simulated. At this level, the mechanism for producing charm is either $g + g \rightarrow c\bar{c}$ or $q + \bar{q} \rightarrow c\bar{c}$ (see Chapter 2). Nason, Dawson, and Ellis have found that the differential cross section *shapes* ($d\sigma/dx_F, d\sigma/dp_t^2$) do not change much when $\mathcal{O}(\alpha_s{}^3)$ diagrams are included [Nas 89]. We decided to generate events taking into account only second order processes, since this was much simpler to implement.

Figure 2.1 schematically shows the charm production process. Recall that x and y are the interacting parton's momentum fractions, $G_{p_i/A}(x)$ is incident particle A's parton distribution function for parton type p_i (similarly for target particle B), and $\hat{\sigma}(\hat{s})$ is the short-distance cross section for charm production at an energy $\hat{s} = \tau s$, where $\tau = xy$ and $\sqrt{s}$ is the overall centre of mass energy. (See Chapter 2 for details.)

To calculate $\hat{\sigma}_{gg\rightarrow c\bar{c}}(\hat{s})$ (and also $\hat{\sigma}_{q\bar{q}\rightarrow c\bar{c}}(\hat{s})$) we start from the second order matrix elements (averaged over initial state colours and spins, summed over final state colours and spins) [Bab 78]:

$$\begin{aligned}\langle|\mathcal{M}_{gg}|^2\rangle &= -\frac{3}{4\hat{s}^2}(\hat{t}-m_c^2)^2 - \frac{3(\hat{t}+m_c^2)}{4\hat{s}} - \frac{17}{24} + \\ &\quad \frac{1}{6}(4m_c^2+\hat{s}+\frac{m_c^4}{\hat{s}})(\frac{1}{m_c^2-\hat{t}}+\frac{1}{m_c^2-\hat{u}}) - \\ &\quad \frac{2m_c^4}{3}(\frac{1}{(m_c^2-\hat{t})^2}+\frac{1}{(m_c^2-\hat{u})^2})\end{aligned}$$

$$\langle|\mathcal{M}_{q\bar{q}}|^2\rangle = \frac{2g^4}{9\hat{s}^2}(12m_c^4 - 8m_c^2(\hat{t}+\hat{u}) + 2(\hat{t}^2+\hat{u}^2)).$$

Figure 7.1 shows the gg and $q-\bar{q}$ matrix elements for a parton-parton center of mass energy of $\hat{s} = 25$ GeV^2.

Using the relation:

$$\hat{\sigma}(\hat{s}) = \int_{\hat{t}_{min}}^{\hat{t}_{max}} \frac{d\hat{t}}{16\pi\hat{s}^2}\langle|\mathcal{M}|^2\rangle,$$

putting in the limits on $\hat{t}$:

$$\begin{aligned}\hat{t}_{min} &= m_c^2 - \frac{\hat{s}}{2} - \frac{1}{2}\sqrt{\hat{s}(\hat{s}-4m_c^2)} \\ \hat{t}_{max} &= m_c^2 - \frac{\hat{s}}{2} + \frac{1}{2}\sqrt{\hat{s}(\hat{s}-4m_c^2)},\end{aligned}$$

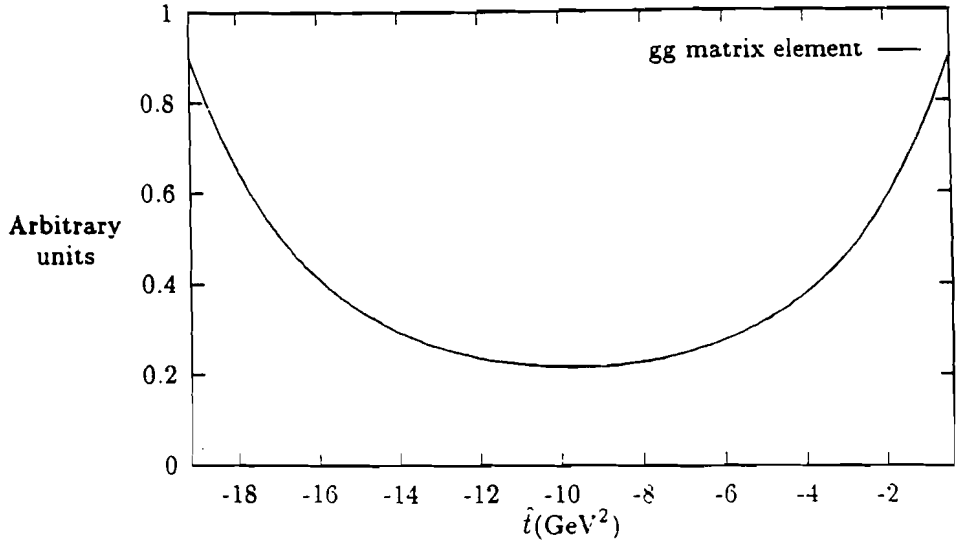

(a)

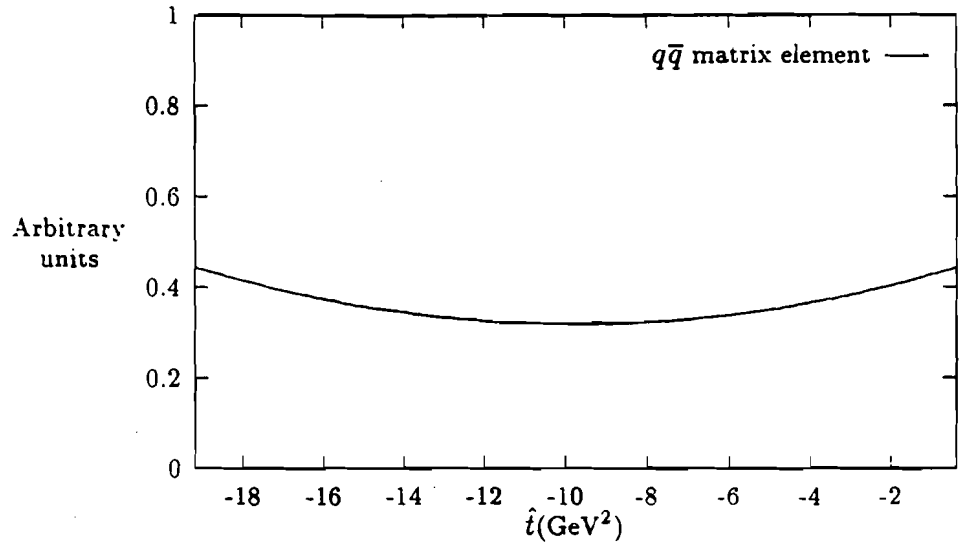

(b)

Figure 7.1: Gluon-gluon (a) and quark-antiquark (b) matrix elements vs. $\hat{t}$ for $\hat{s} = 25$ GeV^2

and defining $\rho = 4m_c^2/\hat{s}$, we get:

$$\hat{\sigma}_{gg\to c\bar{c}}(\hat{s}) = \frac{\pi\alpha_s{}^2}{3\hat{s}}\left((1+\rho+\frac{\rho^2}{16})\ln(\frac{1+\sqrt{1-\rho}}{1-\sqrt{1-\rho}}) - \frac{1}{4}(7+\frac{31}{4}\rho)\sqrt{1-\rho}\right) \quad (7.1)$$

$$\hat{\sigma}_{q\bar{q}\to c\bar{c}}(\hat{s}) = \frac{8\pi\alpha_s{}^2}{27\hat{s}}(1+\frac{\rho}{2})\sqrt{1-\rho}. \quad (7.2)$$

It is important to refrain from simplifying the matrix elements by leaving out the heavy quark mass. If we set $m_c = 0$ the calculations are much simpler, but the resulting differential cross section $d\sigma/dp_t^2$ diverges as $p_t \to 0$. Hence some sort of arbitrary p_t cutoff would be required. This is not the case if one includes the mass terms, since even for $p_t = 0$ we still have $\hat{t} \neq 0$, and the cross section remains finite.

To generate an event, a slightly different form of Eqn. 2.4 is used. Differentiating it with respect to τ gives:

$$\frac{d\sigma_{gg\to c\bar{c}}(s)}{d\tau} = \frac{d\mathcal{L}}{d\tau}\hat{\sigma}_{gg\to c\bar{c}}(\hat{s}=\tau s). \quad (7.3)$$

The values of this function, and all the corresponding quark-antiquark cross sections, were calculated at a large number of points in the range $[\tau_{min}, 1]$ and stored. For each event, a particular value of τ (or $\hat{s}$) was chosen according to sum of these distributions. Then the interacting parton types were chosen based on the relative sizes of the various cross sections at this $\hat{s}$. Next, $\hat{t}$ was thrown according to the distribution of the appropriate matrix element. The parton-parton subsystem was then completely specified. All that remained was to throw the momentum fractions of the interacting partons according to $G_{p_i/A}(x)G_{p_j/B}(\hat{t}/x)/x$.

At this point the underlying event was modelled. At first, we tried to consider that any interaction took place only between the beam particle and a single nucleon; the fact that the nucleon was part of a nucleus was not taken into account. It was found, however, that this technique produced events which had charged particle multiplicities which were about 15% lower than data events. Instead, we used Fritiof [And 87], a program from the Lund Monte Carlo Group, which was designed specifically to model hadron-nucleus collisions, which basically allowed multiple soft interactions to take place inside the nucleus.

To generate an event, $\hat{s}$, $\hat{t}$, and x were thrown as described above. The momentum fractions carried by the interacting partons were removed from the incident and target hadrons, and then Fritiof was used to simulate the underlying interaction. It was found that this technique reproduced the data's multiplicity and p_{t715} distributions very well.

To model the fragmentation of the generated quarks into hadrons we used the Lund Monte Carlo, which implements a string-based fragmentation approach [And 83]. It also simulates the decays of unstable particles, using a phase-space decay distribution for most. The output of these routines was a list of particles, called the Lund List, which contained the 4-momenta of all the particles present in the fragmentation-decay chain of the initial quarks. An interaction (x, y, z) point was then chosen based on our beam and target characteristics, and decay times were thrown for the unstable particles (with lifetimes according to the PDG[PDG 90]). The trajectories for all particles in the event were determined by this stage. These particles were then passed through the detector simulation, described below.

7.2 Detector Simulation

The detector simulation is a collection of routines which simulate the interactions of a particle travelling through the spectrometer with the various detectors. For each detector the physical size, number of radiation lengths, number of interaction lengths, etc. were programmed into the MC. The particles were then passed through simulations of each detector in turn. Multiple scattering of charged particles was taken into account here, as was the possibility of secondary interactions with detector materials. Charged particles were swum through the magnets. The emmission of Čerenkov light in C1 and C2 was modelled by randomly emitting photons along the particles' path according to the known intensity law. These photons' paths were then traced using the inputted mirror and winston cone positions, and the total number of incident photons in each phototube was determined. Electromagnetically showering particles' (e, γ, π^0) interactions with the SLIC were simulated using a trimmed-down version of the EGS Monte Carlo. (It was simplified due to speed and memory considerations. As well, we did not require the accuracy of a full EGS simulation.) The showering of hadrons in both the SLIC and the Hadrometer was modelled using a simple average parameterization of the shower depth and width.

After all of this, a table called the Truth Table was constructed, which included the positions of all the charged particles at each silicon, drift chamber, and PWC plane, the amount of light in each Čerenkov phototube, the energy deposited in each calorimeter module, and the full Lund List information described above. This Truth Table was then passed to the Digitizer program, which translated the information into the raw data format produced by the actual detector. This allowed the MC generated

events to be passed through the exact same analysis chain that the real data went through, in order to extract reconstruction efficiencies, etc. The Digitizer code also modelled the effect of detector inefficiencies, hot and dead channels, cross-talk, and noise. The size and form of all these effects were determined from the data.

An event's characteristics can be described by a small set of parameters, and there are many choices for this set. Fixed target charm experiments and theories usually use the x_F and p_t^2 of the charm quark (or D meson) to parameterize the actual charm particle's production properties. To characterize the rest of the event we use the total transverse momentum of all tracks, called p_{t715} (see below). The Monte Carlo was tuned to match the data's distribution of these parameters. Figure 7.2 shows the data (data points) and the Monte Carlo (histogram) distributions of these variables for $D^+ \rightarrow K^-\pi^+\pi^+$ events. The average charged track multiplicity matched the data to within 7%.

7.3 The Trigger Monte Carlo

The correction for the trigger's efficiency was also performed in the Monte Carlo. The analysis presented here used events which passed either the E_t or E_{tB} trigger. These triggers required the event to pass the interaction trigger criterion, and to have a total transverse energy which surpassed one of two thresholds. Sec. 5.2 describes these triggers.

A threshold curve for the interaction requirement was made, which parameterized the efficiency vs. *nsmdtrk*, the number of tracks which had support in the silicon system. Since the interaction trigger was based on a scintillation counter, which produces a signal proportional to the number of charged tracks passing through it, this parameterization tracked the efficiency most accurately . Table 7.1 shows the efficiencies for various track multiplicities. Note that for reconstructed charm events, which have high multiplicities (typically 10), this part of the trigger is fully efficient.

	nsmdtrk									
	2	3	4	5	6	7	8	9	10	11
effic.	0.647	0.713	0.878	0.953	0.979	0.987	0.987	0.990	0.990	1.0

Table 7.1: The Interaction Trigger efficiency by track multiplicity

The E_t trigger was more difficult to model. The transverse energy of each event

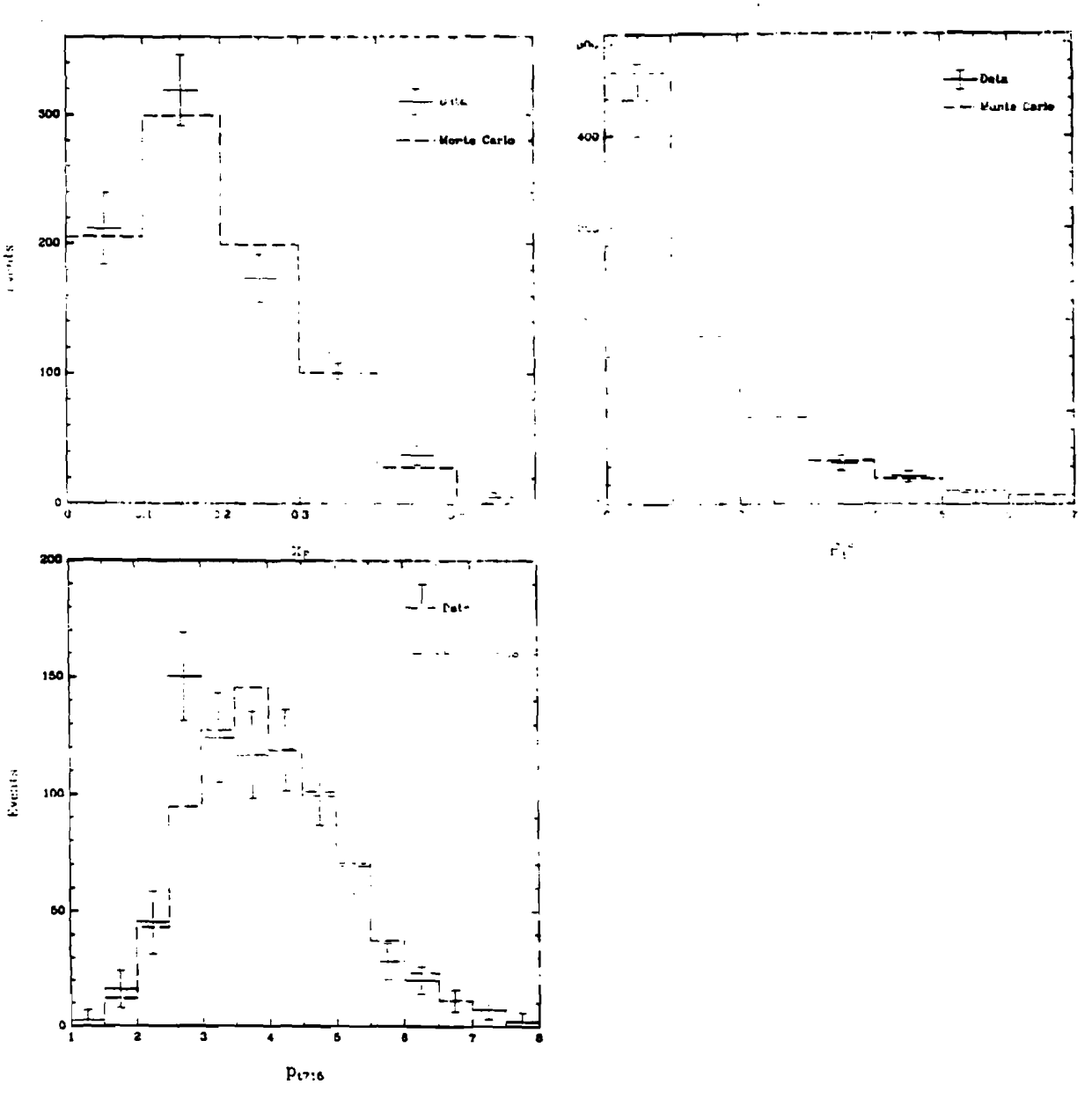

Figure 7.2 Comparison of Data and Monte Carlo

was estimated by performing a weighted sum of the energy deposited in each of the calorimeter modules (see Sec. 5.2). However, the gates defining the signal integration time were different for the SLIC and the Hadrometer. At the high beam rates of the positive data, there was a large probability of two beam particles arriving during the calorimeter gates. Hence, once one particle had traversed the detector and started the readout sequence, a second particle may have arrived and deposited some fraction of its energy within the window remaining. Modelling this out-of-time energy was extremely difficult because it required detailed knowledge of the time evolution of the collected signal and of the time distribution of beam particles, which was not available.

To circumvent these problems, we parameterized the E_t trigger efficiency in terms of a variable called p_{t715}. p_{t715} is defined as the sum of the transverse momentum of all reconstructed tracks which passed through both magnets. It has the great advantage of being insensitive to out-of-time energy. Since the timing is wrong for all the hits left by a second particle's tracks, the reconstruction will see them as random noise which doesn't form any recognizable patterns.

Figure 7.3 shows the trigger efficiency $\varepsilon_{E_t}(p_{t715})$ for the E_t trigger during the negative data run. It is measured relative to interaction-only events. Superimposed is the trigger-corrected reconstructed D^+ distribution. From this plot we can determine that the E_t trigger was 80 ± 5 % efficient for charm which was reconstructable.

For each Monte Carlo event, p_{t715} was calculated, and the probability $p_{trig} = \varepsilon_{E_t}(p_{t715})\varepsilon_{INT}(nsmdtrk)$ determined. The event is randomly accepted with probability p_{trig}, or rejected, with probability $1 - p_{trig}$.

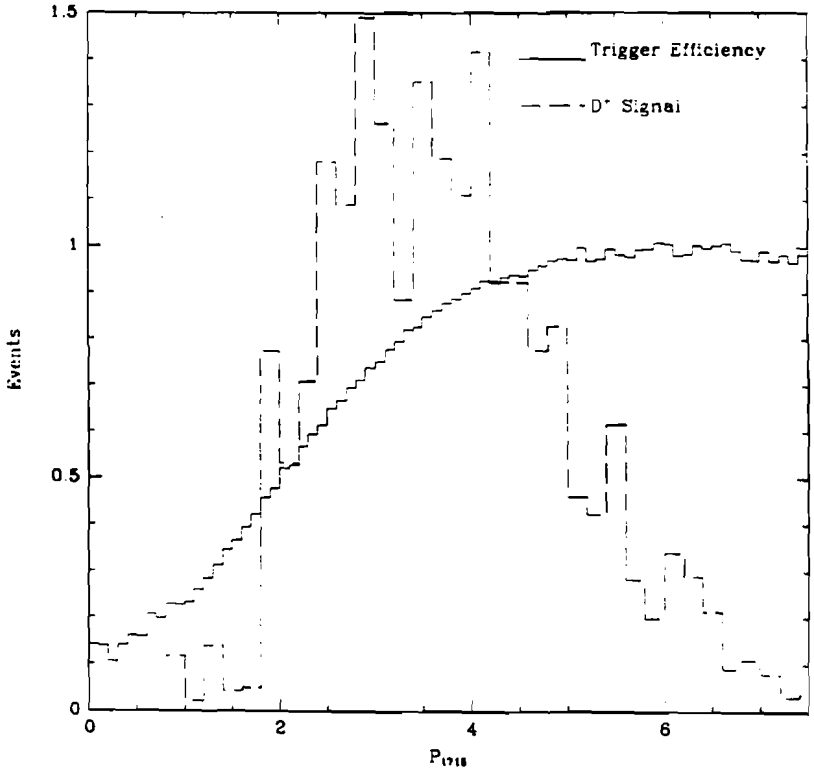

Figure 7.3: The E_t trigger efficiency, and the trigger-corrected D^+ distribution, as a function of p_{t715}.

Chapter 8

Extraction of the D Signals

This chapter details the selection criteria used to extract the $D^+ \rightarrow K^-\pi^+\pi^+$ and $D^0 \rightarrow K^-\pi^+$ (and charge conjugate) signals, which were subsequently used to determine the A-dependence and total cross section of charm production. Both these signals were extracted from the pair-stripped data (described below). This data was then passed through substrips tuned for each mode which were used to further reduce the data sample. However, since the cuts used in these strips were subsets of the final analysis cuts, they had no effect on the final signal — they simply provided a convenient intermediate sample size. For this reason, a discussion of these substrips will be omitted.

8.1 The Pair Strip

To reduce the reconstructed data sample of 370 M events to a manageable size, it was passed though a stripping program called the pair strip, which was run on the Silicon Graphics machines.

All charm events have at least three vertices: the primary interaction point (primary vertex), and at least two charm decay vertices (secondary vertices). It was through the exploitation of this property that the rejection of a large fraction of the background was achieved. Although there are always at least two decay vertices, due to the limited acceptance of the spectrometer, typically all of the products from only one of the decays enter the detector. Hence we search for events with two well separated vertices; these events possibly contain reconstructable charm decays. Since this property is common to all the charm decay modes studied, a strip based on this criterion provided a useful data reduction for such modes. After this pair strip, each individual mode had its own strip, which further reduced the data set.

The pair strip algorithm first found all two-track pairs from the set of all tracks which had hits in the silicon system and went through at least one magnet. For each such pair, it then checked if either track was in the primary vertex. (The vertex found by the PASS2 vertexing algorithm which had the highest mulitplicity was chosen as the primary. This was found to be superior to choosing the most upstream vertex, because false two-track vertices were often generated by the algorithm, and including these reduced the charm reconstruction efficiency.) If either (or both) track(s) were included in the original primary vertex, the vertex was refitted with the track(s) excluded. Any combinations with the z-location of the newly fitted vertex ($ZPRI$) ≤ -6.0 cm were discarded, since these represented events which interacted upstream of the target. Next, the two track combination was fit to a vertex, and the following cuts were applied: The z-position of the fit ($ZSEC$) must be ≥ -6.0 cm, the error on the z-position (σ_{ZSEC}) must be $\leq$ 1800 μm, and the chi-square per degree of freedom (χ^2/DOF) must be ≤ 5. Vertex pairs which did not pass all of these cuts were discarded.

Once all the vertex quality criteria were met, the significance of the vertex separation was calculated. Since the spectrometer's acceptance is $\pm$100 mrad, the reconstructed tracks' trajectories were very nearly parallel to the z axis. That is, Δx and Δy are negligible, and the separation of the vertices is approximately the z-separation $\Delta z \equiv ZSEC - ZPRI$. Also, since the longitudinal error on the vertex position is typically $300 - 500$ μm for the secondary vertex, while the transverse resolution is ~ 10 μm, the z-error dominates the error on the vertex position. A cut was made on the value of $SDZ \equiv \Delta z/\sigma_z$, where $\sigma_z = \sqrt{\sigma^2_{ZPRI} + \sigma^2_{ZSEC}}$ and σ_{ZPRI} is the z-error on the primary vertex, etc. The pair strip required an $SDZ \geq 6$. Figure 8.1(a) shows a drawing of the SDZ cut.

We also required that the impact parameters of the secondary vertex's tracks to the secondary vertex were less than the impact parameters to the primary, as defined by the RAT cut. This variable, defined as $RAT \equiv \prod_i b_i^{sec}/b_i^{pri}$ (where i labels the tracks, and b^{sec} and b^{pri} are the impact parameters to the secondary and primary vertices), was formed, and required to be ≤ 0.06. A schematic of the RAT cut is shown in Figure 8.1(c).

Finally, the p_t^2 of the two tracks with respect to the direction defined by the sum of their momentum ($PT2DK$) was required to be ≥ 0.1. This cut is described in more detail below.

Events which had at least one track pair combination which satisfied all of the

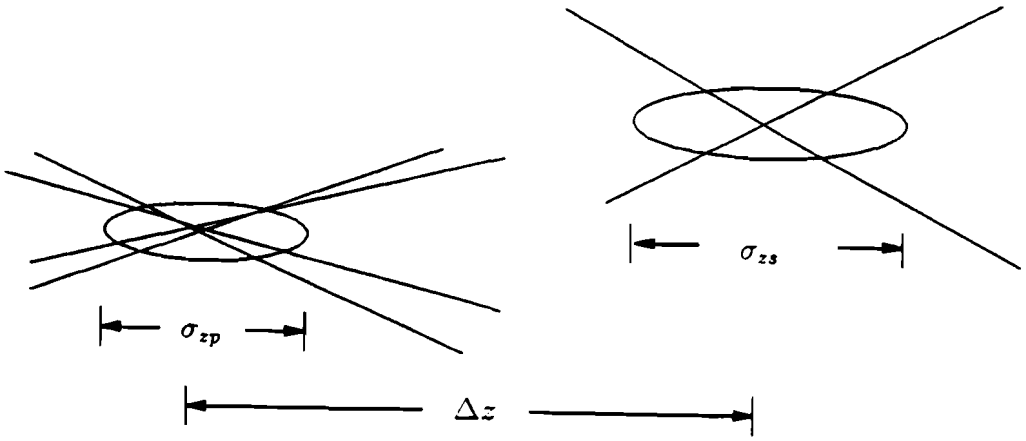

$$SDZ = \Delta z/(\sigma_{zp}^2 + \sigma_{zs}^2)^{\frac{1}{2}}$$

(a)

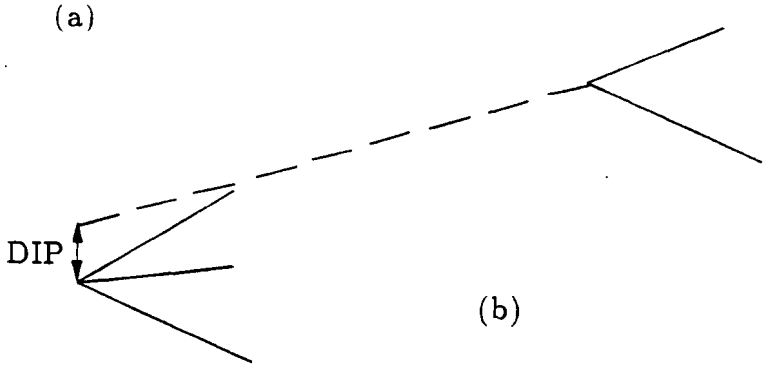

(b)

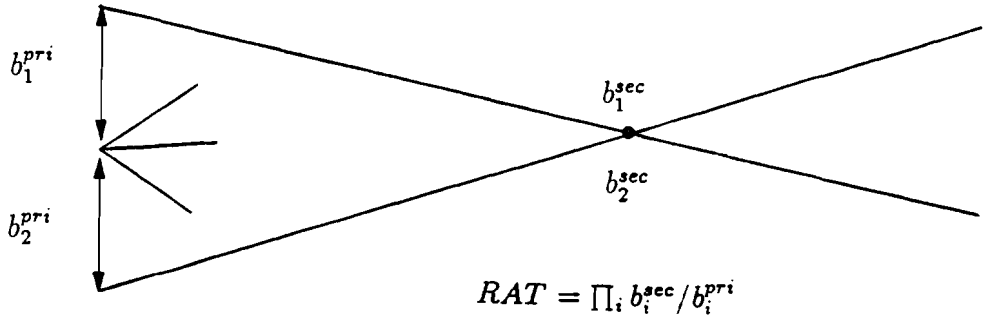

$$RAT = \prod_i b_i^{sec}/b_i^{pri}$$

(c)

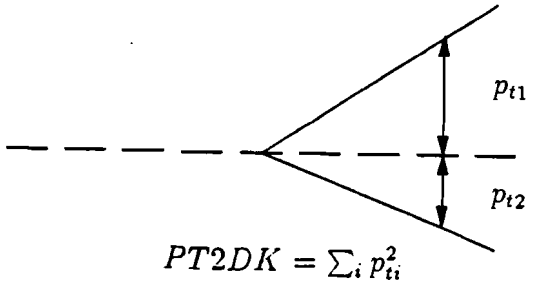

$$PT2DK = \sum_i p_{ti}^2$$

(d)

Figure 8.1: The Principle Analysis Cuts

above cuts were accepted by the strip: all others were rejected. The pair strip cuts were chosen to be fully efficient with respect to the final analysis cuts, while maximizing the strip's rejection factor. Table 8.1 summarizes the cuts in the pair strip. These cuts reduced the data by a factor of 15 (so the data sample was reduced to 25 M events), while having an efficiency with respect to the final analysis cuts of 98% (as determined by Monte Carlo studies).

Cut	Required Value
ZPRI	≥ -6.0
ZSEC	≥ -6.0
σ_{ZSEC}	≤ 1800 μm
χ^2_{SEC}/DOF	≤ 5
SDZ	≥ 6
RAT	≤ 0.06
$PT2DK$	≥ 0.1

Table 8.1: The Pair Strip Cuts

8.2 The D^+ Signal

The cuts used to bring out the $D^+ \rightarrow K^-\pi^+\pi^+$ signal were very similar to those used in the pair strip. As per the pair strip, the vertex with the highest multiplicity found by PASS2 was chosen to be the primary. Then, all 3-track combinations with total charge equal to ± 1 were examined. These tracks were required to pass through at least one magnet, be reconstructed through the SMD region, and have momentum greater than 3 GeV. The track with the odd charge was assumed to be a kaon and the two same-sign tracks were assumed to be pions. The invariant mass of the 3-track combination was calculated, and required to be within ± 200 MeV of the D^+ mass. If the combination passed this cut, a vertexing algorithm was run on the 3-track secondary vertex candidate. The χ^2/DOF of this vertex was required to be ≤ 5.

If any of the secondary vertex's tracks were also in the original primary vertex, they were excluded from the primary, and this vertex was re-fit. The re-fit primary vertex was required to have a z-coordinate inside the target, and to have a $\chi^2/DOF \leq 5$.

The quality of the vertex separation, SDZ, was required to be ≥ 12.

A RAT cut (with a definition analagous to that in the pair strip) was applied to the secondary vertex's three tracks. RAT was required to be ≤ 0.006.

Two cuts which rely on the fact that the D^+ decay vertex has exactly three tracks were the DIP and ISO cuts. To form the DIP of the decay vertex, the 3-momenta of the three decay tracks were summed, giving the 3-momentum of the (supposed) parent particle. Using this momentum vector, and the positions of the secondary and primary vertices, the impact parameter of the parent particle to the primary vertex (called DIP for D *I*mpact *P*arameter) was calculated. If the vertex was formed by a true 3-body decay, or a secondary interaction which had three products, this should point back to the primary vertex, so this DIP was required to be $\leq 80\ \mu m$. If the vertex was from a decay containing four or more products, or from a secondary interaction which didn't produce just three charged tracks, the tracks' momenta would usually not sum to the true momentum of the parent, and the point-back would typically fail. Figure 8.1(b) shows the DIP cut.

To further reduce the background from secondary interactions, the secondary vertex was required to be isolated. That is, no other track in the event was allowed to pass within 60 μm of it. Hence even secondary interactions which produce, for example, three high momentum particles and one low momentum particle, which could possibly pass the DIP cut, will not pass this isolation (ISO) cut.

At this stage, an analysis of the remaining background showed that the dominant contribution to high-mass secondary vertex candidates came from track combinations in which two of the tracks were nearly collinear, but had very different momenta. In decays of pseudoscalar charmed mesons, since they decay isotropically in their rest frame, and since there is on the order of 1 GeV of p_t in the decay products, very few events will have two nearly collinear tracks. To remove these background events, the p_t^2 of the decay *with respect to the parent particle's direction* was calculated. That is, the direction specified by the sum of the three secondary tracks' momenta was determined, and then the sum of p_t^2 of each track with respect to this direction was formed. This value, called $PT2DK$, was required to be ≥ 0.5. Figure 8.1(d) shows a drawing of the $PT2DK$ cut.

The background level for events with the p_t^2 of the charm candidate ≤ 1.0 was much higher than that for events with $p_t^2 \geq 1$. About half of the charm signal has $p_t^2 \geq 1$, whereas 85% of the background was below this value. To further reduce the background in the low p_t^2 region, a Čerenkov cut was applied to the kaon candidate. This reduced the background by 70%, while only reducing the signal by 30%. The probability of a track being a kaon ($KPROB$) was required to be ≥ 0.13.

The values for all the cuts were set by maximizing the significance $S/\sqrt{B}$, where

S is the signal size from Monte Carlo data, and B is the number of background events (which came from a representative data sample). This provides an unbiased method of setting cuts, which is essential in preventing the enhancement of a statistical fluctuation in the data.

Table 8.2 summarizes the $D^+ \rightarrow K^-\pi^+\pi^+$ analysis cuts.

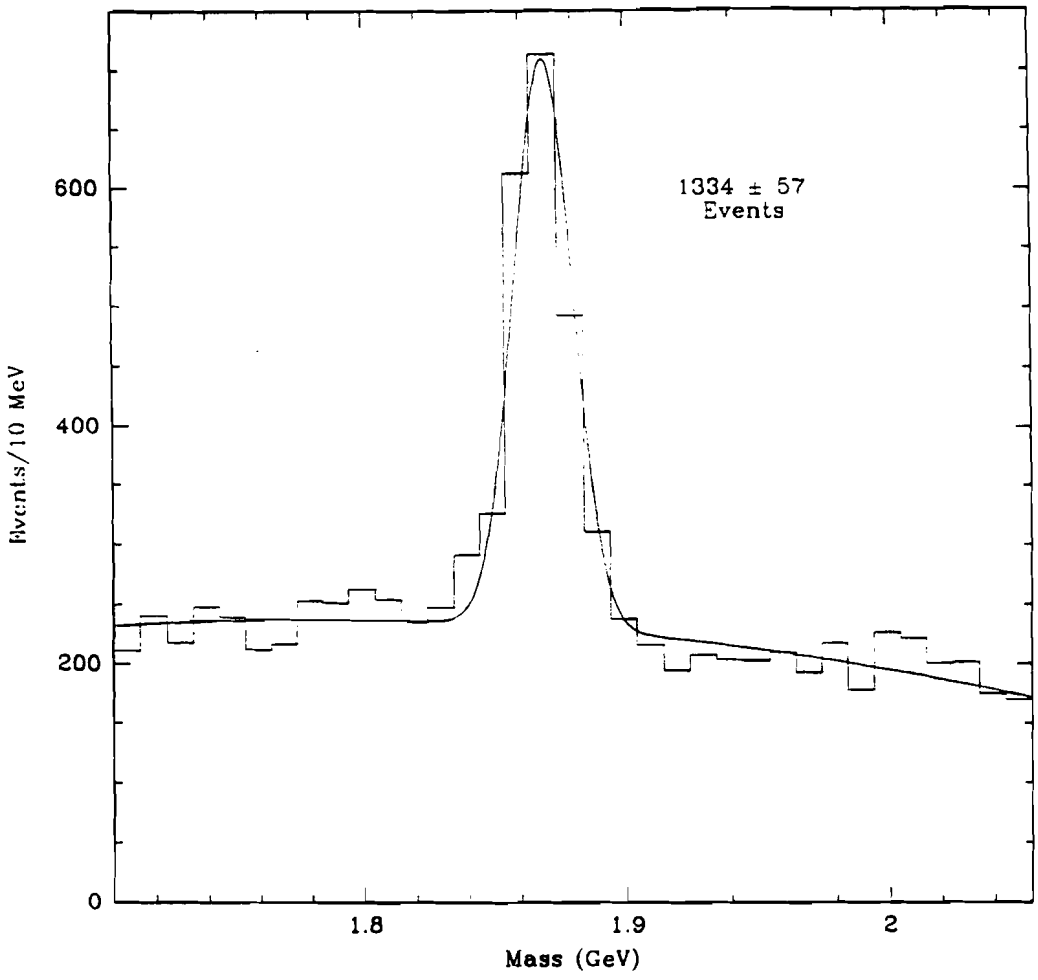

Figure 8.2: $D^+ \rightarrow K^-\pi^+\pi^+$ Signal

Figure 8.2 shows the fit to the entire signal, which consisted of 1334 ± 57 events. The fit used a quadratic background plus a gaussian signal. It was found that a linear background produced poor fits and overestimated the signal size. In this fit, the mass of the signal was fixed to the D^+ mass (1.869 GeV) — all other variables were allowed to float. The χ^2 for the fit was 1.8, and the signal width was 11.0 ± 0.5 MeV. The fits to the Monte Carlo events gave a width of 10.0 ± 0.1 MeV, in reasonable agreement

Cut	$p_t^2 < 1.0$	$p_t^2 \geq 1.0$
$ZPRI$	$-6.0 \leq ZPRI \leq -1.0$	$-6.0 \leq ZPRI \leq -1.0$
χ^2_{SEC}/DOF	≤ 5	≤ 5
SDZ	≥ 12	≥ 12
DIP	$\leq 80\ \mu m$	$\leq 80\ \mu m$
RAT	≤ 0.006	≤ 0.006
ISO	$\geq 60\ \mu m$	$\geq 60\ \mu m$
$PT2DK$	≥ 0.5	≥ 0.5
$KPROB$	≥ 0.13	–

Table 8.2: D^+ Analysis Cuts

with the data.

8.3 The D^0 Signal

The $D^0 \rightarrow K^-\pi^+$ analysis used all the same types of cuts as the $D^+ \rightarrow K^-\pi^+\pi^+$ analysis; we refer the reader to Table 8.3 for the values. As in the case of $D^+ \rightarrow K^-\pi^+\pi^+$, the background was much higher for events with the p_t^2 of the D^0 less than 1.0, so the cuts were tighter in this region. There was, however, one additional cut employed, which was similar to the $PT2DK$ cut. The cosine of the angle between either of the decay products in the D^0's rest frame and the D^0 direction of motion (COS) was required to have an absolute value less than 0.75. This helped to eliminate more of the background due to events with two nearly-collinear tracks that the $PT2DK$ cut did not discard.

Figure 8.3 shows the $D^0 \rightarrow K^-\pi^+$ signal, which consisted of 949 ± 54 events. In this case, it was found that a linear background and a gaussian signal fit the data adequately, so a quadratic term was not added to the background. The fit shown had the the mass fixed to 1.865 GeV while the other parameters were allowed to float. The fitted width was 11.6 ± 0.7 MeV, and the χ^2 of the fit was 0.6. The Monte Carlo signal had a width of 10.9 ± 0.1, again in reasonable agreement with the data.

Cut	$p_t^2 < 1.0$	$p_t^2 \geq 1.0$
$ZPRI$	$-6.0 \leq ZPRI \leq -1.0$	$-6.0 \leq ZPRI \leq -1.0$
χ^2_{SEC}/DOF	≤ 5	≤ 5
SDZ	≥ 8	≥ 8
DIP	$\leq 60\ \mu m$	$\leq 60\ \mu m$
RAT	≤ 0.07	≤ 0.05
ISO	$\geq 40\ \mu m$	–
$PT2DK$	≥ 0.9	≥ 0.5
$KPROB$	≥ 0.15	≥ 0.15
COS	$-0.75 \leq COS \leq 0.75$	$-0.75 \leq COS \leq 0.75$

Table 8.3: D^0 Analysis Cuts

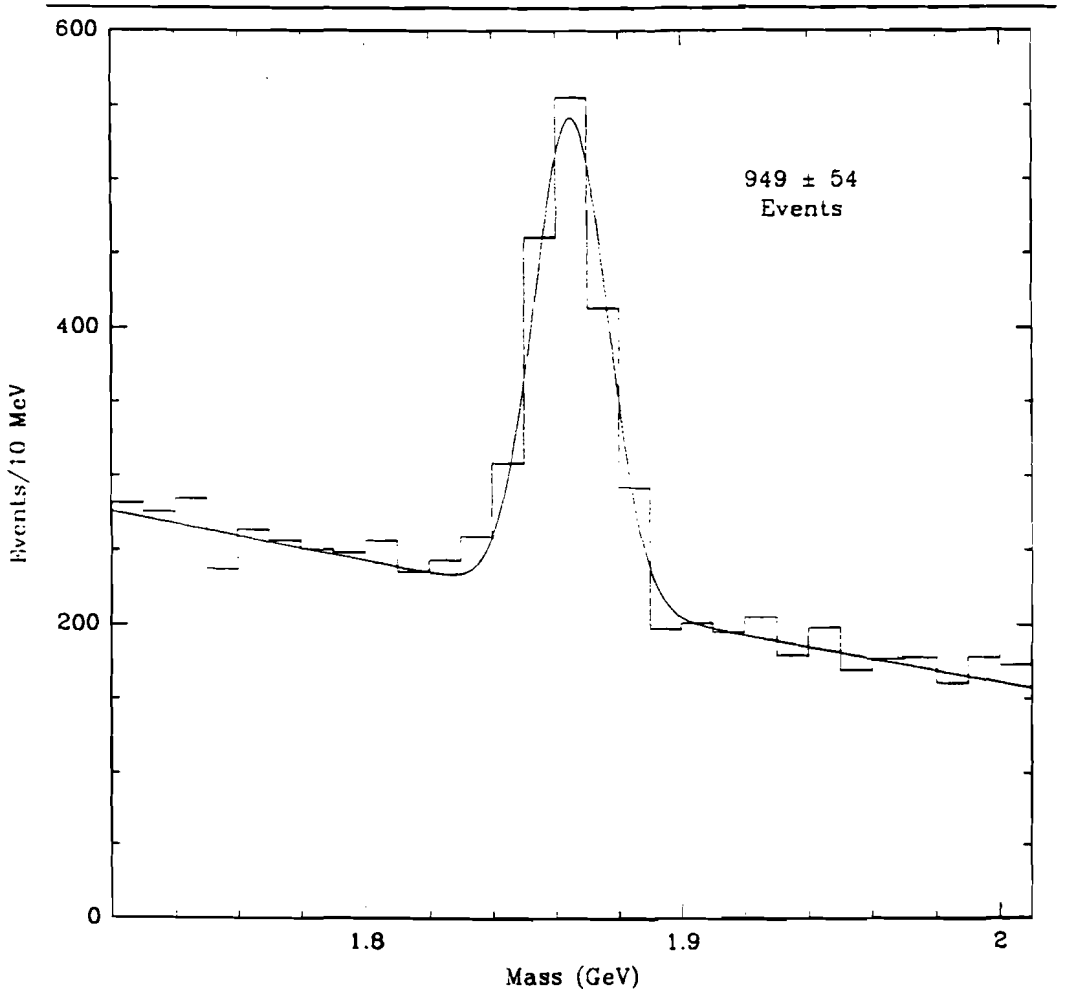

Figure 8.3: $D^0 \rightarrow K^-\pi^+$ Signal

Chapter 9

The A-Dependence and Total Charm Cross Section

9.1 The Cross Sections by Target

Once the D^+ and D^0 signals have been extracted, we can calculate the corresponding cross sections for pions incident on the various target materials.

A detailed derivation of the formula used for calculating the cross sections is given in Appendix A. The result is that the $\pi \rightarrow D^+$ *per nucleus* cross section is given by (see Eqn.A.12):

$$\sigma^{N}_{\pi^- \rightarrow D^+}(i) = \frac{1}{\mathrm{BR}(D^+ \rightarrow K^-\pi^+\pi^+)} \frac{A_i}{\rho_i N_A t_i} \frac{F}{R_\pi T_\pi(i)} \frac{n_{\pi^- \rightarrow D^+ \rightarrow K\pi\pi}(i)}{\epsilon_{\pi'}(i) Norm(\pi', \pi)}, \tag{9.1}$$

where:

- i indexes the four target types (namely Be, Al, Cu, and W);
- A_i is the average atomic mass number of target i;
- ρ_i is the density of target i;
- N_A is Avogadro's number;
- t_i is the thickness of target i in cm;
- R_π = fraction of pion beam at the tagging point which reaches the most upstream target foil (some is lost in upstream interactions);
- $T_\pi(i)$ is the amount of beam which is transmitted from the most upstream foil of the target to target region i;

- BR($D^+ \to K^-\pi^+\pi^+$) is the $D^+ \to K^-\pi^+\pi^+$ branching ratio:
- π' denotes beam particles which were tagged as pions:
- $Norm(\pi', \pi)$ is the total number of true pions in the sample of incident particles tagged as pions (π''s) while the experiment was live:
- F is a correction factor which accounts for the contamination of the tagged pion signal by kaons and protons:
- $n_{\pi'-D^+_{-K\pi\pi}}(i)$ is the $D^+ \to K^-\pi^+\pi^+$ signal from each of the target materials from the π' sample:
- $\epsilon_{\pi'}(i)$ is the trigger + reconstruction efficiency for events from target i. It is determined from the Monte Carlo.

A similar formula holds for D^0's.

Appendix A contains a detailed discussion of these terms, but we briefly summarize some of the main points here. First, the contamination of the identified pion sample is about 5% for the negative beam, and 0.6% for the positive beam. This means we are very insensitive to effects due to the contamination having a different cross section. We estimate that $F = 1.06 \pm 0.03$ for the negative beam, and $F = 1.01 \pm 0.005$ for the positive beam. Second, the efficiencies $\epsilon_{\pi'}(i)$ contain effects due both to the triggers and the analysis cuts. The trigger efficiencies are discussed in Sec. 5.2 and Sec. A.3.

Figures 9.1 and 9.2 show the fitted $D^+ \to K^-\pi^+\pi^+$ and $D^0 \to K^-\pi^+$ signals for each of the four target materials. As discussed in Chapter 8, the D^+ signals were fit using a gaussian signal and a quadratic background, while the D^0 signal fits used a linear background. Because these plots have small signal sizes, both the mass and the width were fixed in the fits. The widths for each target were set to the values given by fits to Monte Carlo signals. The signals include all events with $x_F \geq 0$ (the acceptance falls to zero very rapidly below $x_F = 0$).

Unfortunately, at the time of this writing, the normalisation for the positive data was uncertain by about 30%. For this reason, we do not present cross section numbers for the positive data here. This analysis is ongoing, and it is expected that these measurements will be available within a few months.

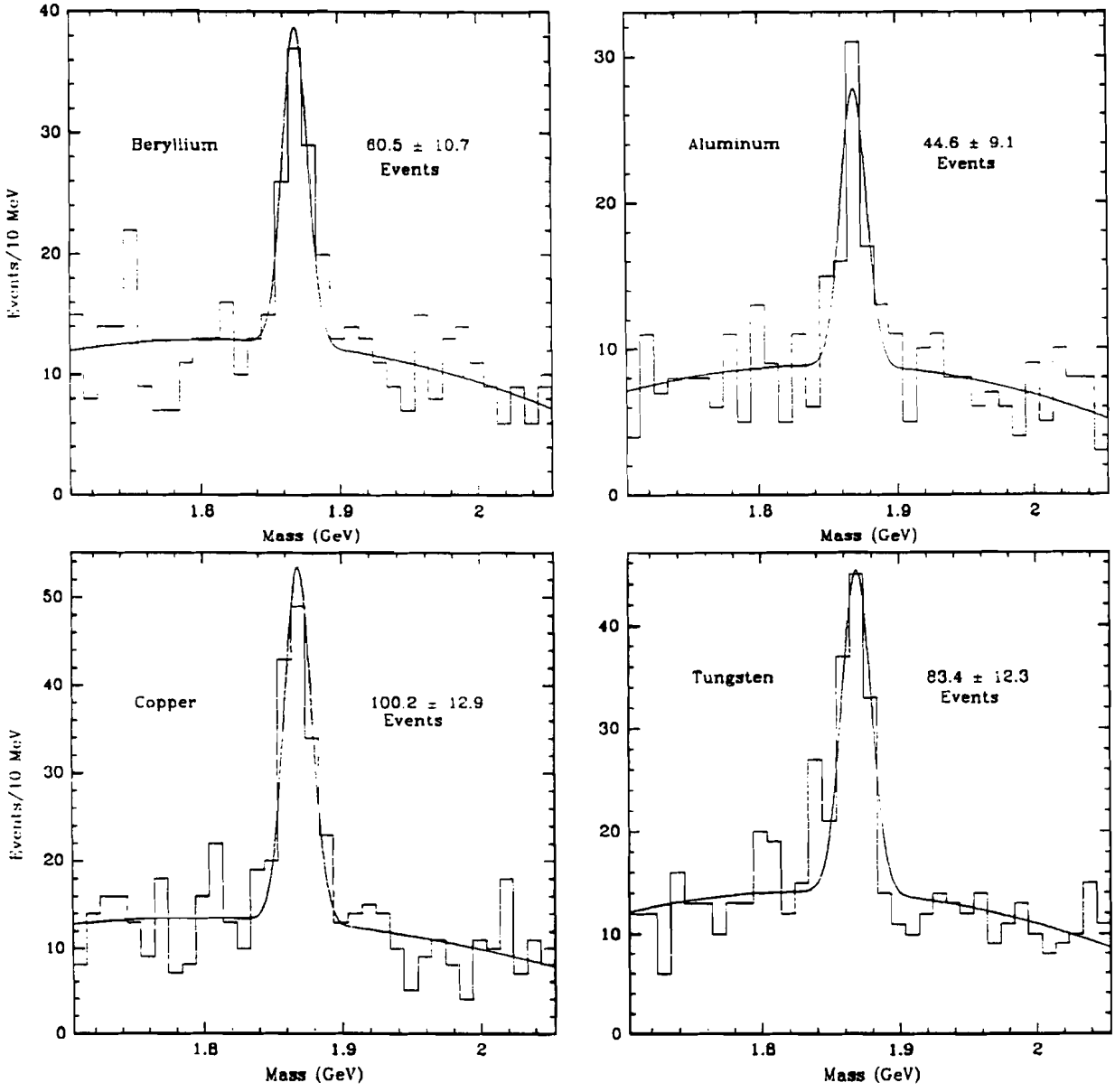

Figure 9.1: The D^+ Signals from the negative pion beam

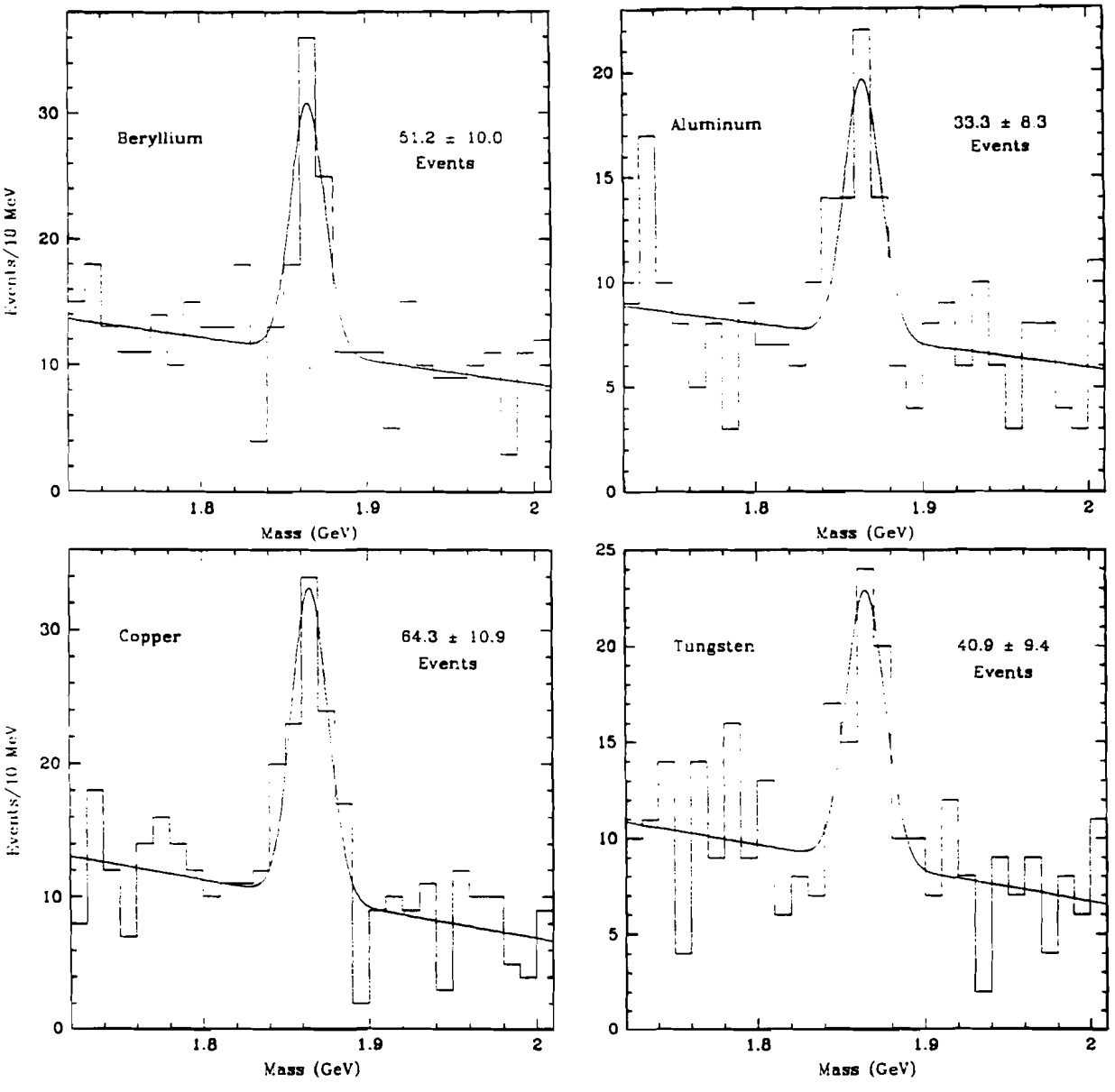

Figure 9.2: The D^0 Signals from the negative pion beam

Target	D^+ Signal	D^0 Signal
Be	60.5 ± 10.7	51.2 ± 10.0
Al	44.6 ± 9.1	33.3 ± 8.3
Cu	100.2 ± 12.9	64.3 ± 10.9
W	83.4 ± 12.3	40.9 ± 9.4

Table 9.1: The D^+ and D^0 signals from the various targets.

9.1.1 Systematic Errors

An examination of Eqn.9.1 leads to the following sources of systematic error on the cross section for each target material:

- the target thicknesses, t_i;
- the transmission coefficients, $T_\pi(i)$;
- the beam lost in upstream interactions, R_π;
- the beam normalisation, $Norm(\pi', \pi)$;
- the reconstruction + trigger efficiencies, $\epsilon_{\pi'}(i)$, determined from the Monte Carlo;
- the branching ratios, BR($D^+ \rightarrow K^-\pi^+\pi^+$) and BR($D^0 \rightarrow K^-\pi^+$).

The errors in the measurements of the target thicknesses are given in Table 3.1: they correspond to cross section errors of: 0.9% (Be), 0.4% (Al), 0.4% (Cu), and 2% (W).

Since only about 1.5% of the beam is lost between the upstream and downstream ends of the target, the error on the transmission coefficients is very small; it was determined to be 0.1%.

About 1% of the beam was lost in upstream interactions. The estimated error in determining this number was ±50%, giving a net error of 0.5%.

The error in the beam normalisation was determined by calculating it under the following conditions:

- with all the variables set to their nominal values;
- with the pion beam fraction set to its maximum and minimum possible values;

- with the kaon beam fraction set to its maximum and minimum possible values:
- with the anti-proton beam fraction set to its maximum and minimum possible values:
- with the DISC kaon tagging probability set to its maximum and minimum values.

The mean of these values was chosen as the normalisation, with the standard deviation as the error. The error was found to be 2%. Also included in the normalisation was the effect of multiple beam particles occupying the same bucket. This was a 3% effect, with an estimated error of 1%.

The main source of systematic error was in the reconstruction + trigger efficiencies. Even though the agreement between the Monte Carlo and data was good (see Figure 7.2), it was not perfect. To compensate for this, three weighting functions were introduced. As discussed in Chapter 7, an event can be characterized by three variables — the x_F and p_t^2 of the D, and the p_{t^*15} of the event. The reconstruction and trigger efficiencies depend primarily on these values. Both the data and the Monte Carlo signals were fit in bins of x_F, p_t^2, and p_{t^*15}, and then the data distributions were divided by the appropriate MC distributions, and fit by fourth order polynomials to get the weighting functions. Three individual functions, as opposed to one full three-dimensional function, were used, because it was found that the three functions were independent (within errors). For example, it was found that the p_t^2 weighting function was the same (within errors) whether or not the x_F and p_{t^*15} weighting functions were included in its determination. These functions were then applied to the MC events and the overall reconstruction + trigger efficiencies were determined for each target. Because of the limited statistics in the data, these weighting functions had a range of possible shapes. The error due to this variation was determined by comparing the efficiency with and without the weighting functions. This produced a mean variation in the efficiencies of 17%. However, a flat weight (i.e. no weighting) overestimated the possible shift in the functions' shapes. A flat line fit to the data/MC histograms was typically almost 2 standard deviations away from the data points, indicating that 17% is an overestimate of the error. We have estimated this systematic error to be 10%. This error is limited by the data statistics.

The efficiencies are also sensitive to the silicon, drift chamber, and PWC plane efficiencies input into the MC digitizer. The values for these quantities which were

used were the average values for the negative running period. The MC matched these to within 1%. Studies which varied these efficiencies indicate that the error due to this was less than 2%. We set this error to be 2%.

Finally, it was found that a correction to the MC Čerenkov counter efficiencies was necessary. A study [Jed 91] was made comparing the reconstruction efficiency for kaons from phi mesons to that predicted by the Monte Carlo. A correction factor was determined as a function of the kaon momentum, and applied as a weight to the Monte Carlo events. This correction resulted in a 17% change in the efficiency, with an estimated error of 5%.

Table 9.2 lists the eight efficiencies (one per target), and the estimated errors, which include all the above effects as well as those due to Monte Carlo statistics. The individual errors were combined in quadrature. The values are for events with $x_F \geq 0$.

Target	D^+ Effic. (%)	D^0 Effic. (%)
Be	4.37 ± 0.51	2.62 ± 0.31
Al	4.51 ± 0.53	2.41 ± 0.28
Cu	3.99 ± 0.47	1.94 ± 0.23
W	3.60 ± 0.42	1.61 ± 0.19

Table 9.2: The D^+ and D^0 efficiencies for the various targets.

The branching ratios used were the present world averages, as compiled by the Particle Data Group [PDG 90]. Their values are:

$$\begin{aligned} \mathrm{BR}(D^+ \to K^-\pi^+\pi^+) &= 7.7 \pm 1.0\% \\ \mathrm{BR}(D^0 \to K^-\pi^+) &= 3.71 \pm 0.25\%. \end{aligned}$$

9.1.2 The per-nucleus Cross Sections × BR

Table 9.3 summarizes the per-nucleus cross section times branching ratio for each target material. The first error is statistical, the second is systematic.

9.2 The Atomic Number Dependence

Once the per-nucleus cross sections are known, it is a fairly simple matter to determine the A-dependence of the charm cross section. We parameterize this A-dependence

Material	$\sigma^N_{D^+} \times$BR (μb)	$\sigma^N_{D^0} \times$BR (μb)
Be	$2.9 \pm 0.5 \pm 0.3$	$4.1 \pm 0.8 \pm 0.5$
Al	$8.7 \pm 1.8 \pm 1.0$	$12.2 \pm 3.0 \pm 1.4$
Cu	$26.1 \pm 3.4 \pm 3.1$	$34.4 \pm 5.9 \pm 4.1$
W	$64.4 \pm 9.6 \pm 7.6$	$70.5 \pm 16.3 \pm 8.3$

Table 9.3: The D^+ and D^0 Cross section × BR for the various targets.

by:

$$\sigma^N_{\pi^- D^+}(i) = \sigma_{\pi^- D^+} A_i^{\alpha_\pi}. \tag{9.2}$$

where $\sigma_{\pi^- D^+}$ is the D^+ cross section for a single nucleon.

Taking the log of both sides of this equation gives:

$$\log(\sigma^N_{\pi^- D^+}(i)) = \log(\sigma_{\pi^- D^+}) + \alpha_\pi \log A_i. \tag{9.3}$$

A similar equation holds for D^0's.

This equation shows that both the per-nucleon cross section and the A-dependence can be obtained by fitting a straight line to the points $(x_i, y_i) = (\log A_i, \log(\sigma^N_{\pi^- D^+}(i)))$.

Substituting for $\sigma^N_{\pi^- D^+}(i)$ from Eqn. 9.1 in the above equation gives:

$$\alpha_\pi \log A_i + \log\left(\frac{\sigma_{\pi^- D^+} \mathrm{BR}(D^+ \to K^- \pi^+ \pi^+) N_A R_\pi Norm(\pi', \pi)}{F}\right) = \log\left(\frac{n_{\pi' - D^+}(i) A_i}{\epsilon_{\pi'}(i) T_\pi(i) \rho_i t_i}\right).$$

This formula makes it clear that the slope, α_π, does not depend on the beam normalisation, the beam contamination, or the branching ratios. It also depends only on the target-to-target reconstruction efficiency differences, not on their absolute values. The per nucleon cross section, $\sigma_{\pi^- D^+}$, does depend on these values, however.

A linear least-squares fit was performed to the points (x_i, y_i) as above, with a similar fit for the D^0. It was necessary to use the full covariance matrix for the y_i's since there are correlations between terms due to the Monte Carlo efficiencies, the beam normalisation, etc.

The results for the A-dependences of the D^+ and D^0 signals are:

- D^+: $1.04 \pm 0.07 \pm 0.02$;
- D^0: $0.99 \pm 0.09 \pm 0.02$.

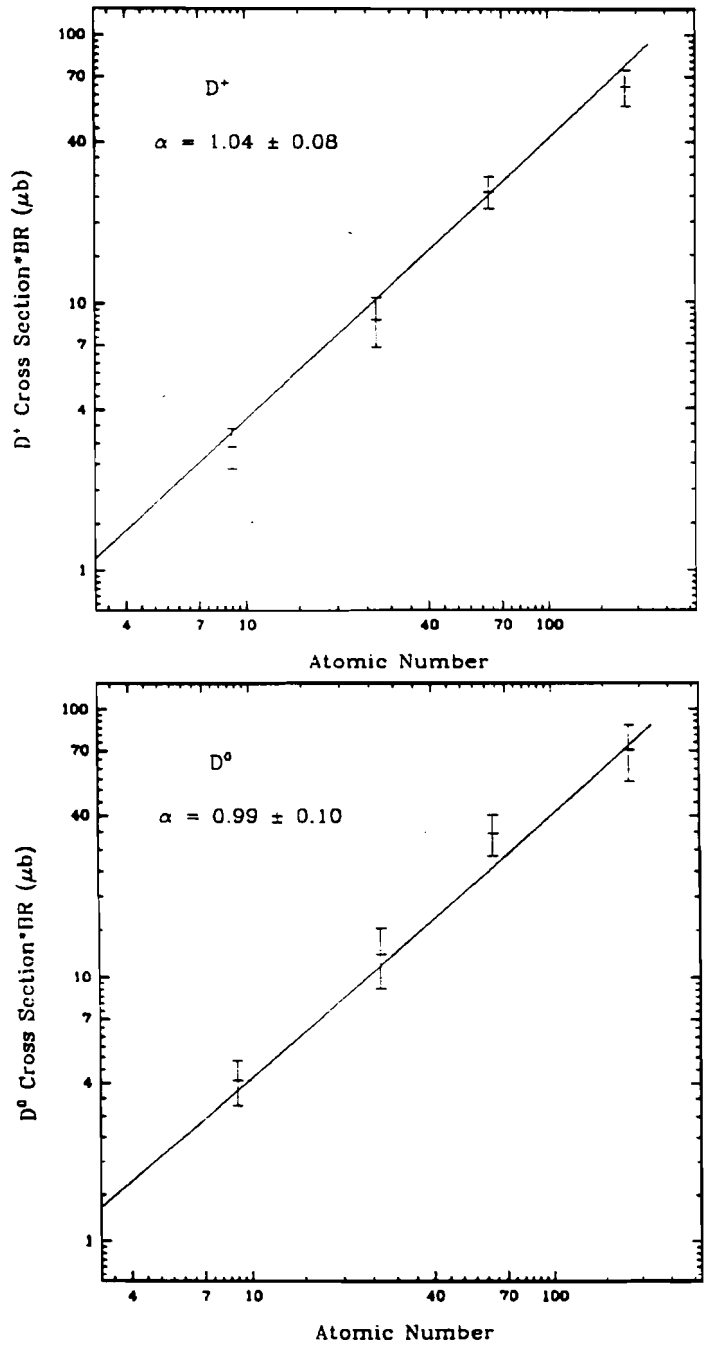

Figure 9.3: The A-dependences of D^+ (upper) and D^0 (lower) production

The A-depedence fits are shown in Figure 9.3. They had χ^2's of 0.73 and 0.78 respectively. The errors shown do not include errors common to all points, such as those due to the normalisation or the absolute reconstruction efficiencies.

Since the A-dependence is a property of the production of the charm quarks, and the process of the charm hadronizing into a D^+ or D^0 takes place much later, we expect to have the same exponent α_π for all types of charm mesons which share the same type of production process. We therefore combine the two measurements into one, with the result being:

$$\alpha_\pi = 1.02 \pm 0.06 \pm 0.02.$$

9.3 The Total Charm Cross Section

9.3.1 The D Meson Cross Section

The *per nucleon* D meson cross sections were obtained from the same fit which gave the A-dependence measurements. The values quoted are those obtained by using the combined A-dependence value given above.

The fitted value for the $\pi^- p \to D$ meson cross sections times branching ratios are:

$$\begin{aligned} \sigma(D^+/D^-) \times \mathrm{BR}(D^+ \to K^-\pi^+\pi^+) &= 0.33 \pm 0.08 \pm 0.04\ \mu\mathrm{b} \qquad (x_F \geq 0); \\ \sigma(D^0/\overline{D^0}) \times \mathrm{BR}(D^0 \to K^-\pi^+) &= 0.43 \pm 0.10 \pm 0.05\ \mu\mathrm{b} \qquad (x_F \geq 0). \end{aligned}$$

After removing the branching fractions, we combine the two measurements to get a D meson cross section (for events with $x_F \geq 0$). To aid in the recalculation of results as the accepted branching ratios change, we keep the error due to them separate. For all subsequent results, the errors quoted are, in order, statistical, systematic, and branching ratio.

Combining the two gives

$$\sigma(D/\overline{D}) = 15.8 \pm 3.7 \pm 1.9 \pm 0.9\ \mu\mathrm{b} \qquad (x_F \geq 0).$$

The error is dominated by the uncertainty in the exponent α_π. In the past, since no A-dependence measurements were available, experiments used an A^1 parameterization, with no error on the exponent. For comparison, our measured value with an $\alpha_\pi = 1.0 \pm 0.0$ is:

$$\sigma(D/\overline{D}) = 17.3 \pm 1.4 \pm 2.0 \pm 1.0\ \mu\mathrm{b} \qquad (x_F \geq 0).$$

9.3.2 The Total Open Charm Cross Section

To derive the total open charm cross section from the D^+/D^0 cross section, we must know the fraction of $c\bar{c}$ pairs which fragment such that at least one D^+ or D^0 is present in the final state. This was estimated using Jetset 6.3, the Lund Monte Carlo fragmentation routine. The input to Jetset must have initial colour strings set up between the various quarks/diquarks in the event. Simulations with differing configurations of these strings gave a mean value of 87% of the events containing one of the above D mesons. The spread in this value was 4%. Changing the Lund fragmentation parameters within their errors produced an insignificant change in this value.

Using this fragmentation fraction, and dividing by 2 since each event has two possible D's gives a total open charm cross section of:

$$\sigma_{c\bar{c}} = 9.1 \pm 2.1 \pm 1.1 \pm 0.5 \ \mu\text{b} \qquad (x_F \geq 0)$$

or, with $\alpha_\pi = 1.0$:

$$\sigma_{c\bar{c}} = 9.9 \pm 0.8 \pm 1.2 \pm 0.6 \ \mu\text{b} \qquad (x_F \geq 0).$$

This value was extended to include all x_F by using the Monte Carlo, which indicated that 60% of the pion cross section was above $x_F = 0$ (also see [Ell 87]).

The final result for the total open charm cross section for pion-nucleon collisions is then:

$$\sigma_{c\bar{c}} = 15.2 \pm 3.5 \pm 1.8 \pm 0.8 \ \mu\text{b}$$

or, with $\alpha_\pi = 1.0$:

$$\sigma_{c\bar{c}} = 16.5 \pm 1.3 \pm 1.9 \pm 1.0 \ \mu\text{b}.$$

9.3.3 The Charm Quark Mass

A fit to the charm quark mass was made using the third-order cross section results of Nason, Dawson, and Ellis (see Chapter 2 and [Nas 88]). The renormalisation scale was chosen to be $\mu^2 = 2m_c^2$, and the structure functions used were set 1 of Duke and Owens. With these choices, the charm quark mass was found to be 1.48 ± 0.15 GeV.

Figure 9.4 shows the measured values of the total open charm cross section from this experiment (the crossed point), LEBC-EHS, ACCMOR, and CCFRS (see Chapter 1 for references). The other experiments' values were adjusted to account for the

non-D part of the cross section (using the fragmentation fraction of 87% described above), as well as the fraction of the cross section below $x_F = 0$. All errors have been combined in quadrature. The two curves are the theoretical predictions for the cross sections with $m_c = 1.5$ GeV for different values of the renormalisation scale.

There is still a large uncertainty on the determination of the charm mass due to the variation with the renormalisation scale. For example, using our central value for the cross section, changing the renormalisation scale between $\mu^2 = m_c^2$ and $\mu^2 = 4m_c^2$ changes the value of the charm quark mass from 1.67 GeV to 1.28 GeV. Using this change as the theoretical error gives a charm quark mass of 1.48 ± 0.15(exper.) $\pm$ 0.2(theor.).

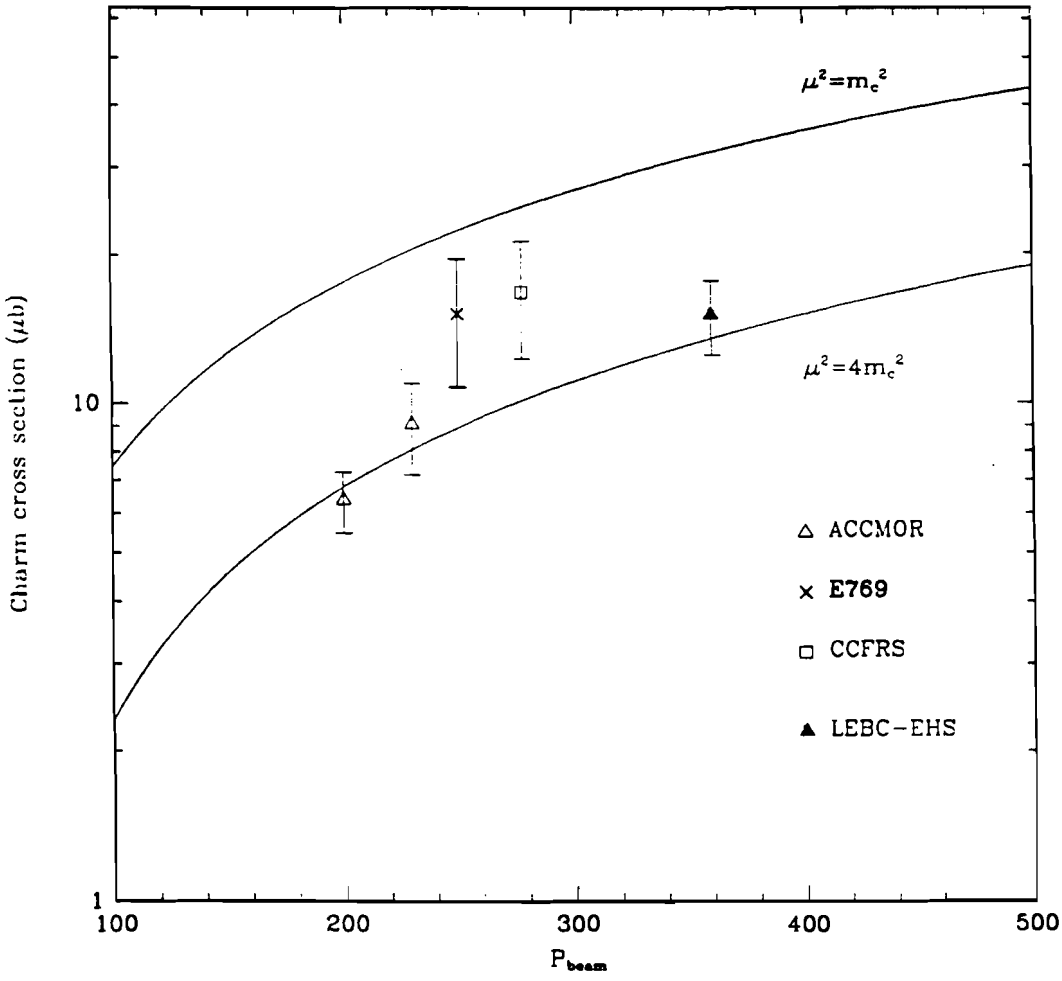

Figure 9.4: Theoretical Predictions for the Open Charm Cross Section, and Experimental Measurements. (The ACCMOR and CCFRS measurements assume $\alpha = 1$, with no error on α.)

Chapter 10

Conclusion

Measurements of the D^+ and D^0 cross sections in π^-N collisions were presented for four different target materials: beryllium, aluminum, copper, and tungsten. The $D^+ \rightarrow K^-\pi^+\pi^+$ and $D^0 \rightarrow K^-\pi^+$ decay modes were used to derive these results since these decays have large branching fractions, low multiplicity and no neutrals in the final state. Using these values, the dependence of the cross section on the atomic number of the target nucleus was determined to be $\alpha_\pi = 1.02 \pm 0.06 \pm 0.02$.

The recent calculation of the charm quark cross section by Nason, Dawson, and Ellis, which included third order effects, predicts a value three times larger than the second order result at a beam energy of 250 GeV. However, they found that the x_F and p_t^2 differential cross section shapes did not change appreciably. Hence, the most sensitive test of their calculations is a measurement of the total charm cross section. We have measured it to be $15.2 \pm 3.5 \pm 2.0$ μb. The theoretical prediction contains two free parameters: the charm quark mass (m_c), and the renormalisation scale (μ). If we vary the renormalisation scale within the bounds $\mu^2 = m_c^2$ to $\mu^2 = 4m_c^2$, the charm quark mass is found to be 1.48 ± 0.15(exper.) $\pm$ 0.2(theor.) GeV. However, within this range of values for μ the cross section prediction changes by a factor of two. This indicates that higher order terms could make a significant contribution. A fourth order calculation of the cross section will be needed if a more stringent test of QCD is to be made using the total charm cross section.

Furthermore, there is still the open question of whether the charm quark cross section factorizes, or if higher twist effects are significant. The possible contribution of these effects, and the uncertainty in the cross section due to higher order terms, are both much smaller for b-quark production. A beauty experiment with a sample size comparable to those of current charm experiments would provide an incisive test of perturbative QCD.

Appendix A

Determining the Cross Section

A.1 General Formula Development

In the following development, we use the terms *true* or *actual* to refer to the actual number of a given beam particle or produced charm particle present during the running period, whether or not it was detected by the experiment. True quantities will be denoted by upper-case variables. Experimentally measured quantities will generally be denoted by lower case variables.

Quantities which refer to one of the four different target types (Be, Al, Cu, and W) are indexed by i. In the analysis, all the foils of a given type are grouped together and considered to be a single target region.

The basic cross section formula for the producion of particle type x from incident pions is:

$$\sigma^N_{\pi\to x}(i) = \frac{N_{\pi\to x}(i)}{N_\pi(i)} \frac{A_i}{\rho_i N_A t_i}, \tag{A.1}$$

where:

- $\sigma^N_{\pi\to x}(i)$ is the *per nucleus* cross section for producing x's from target region i;
- $N_{\pi\to x}(i)$ is the *true* number of events with particle x from target i;
- $N_\pi(i)$ is the *true* number of pions present at target i;
- A_i is the atomic weight of target i;
- ρ_i is the density of target i;
- N_A is Avogadro's number;

- t_i is the thickness of target i in cm.

Since the particles we actually measure are D's, we work with the specific case of $x = D^+$, in the decay mode $D^+ \rightarrow K^-\pi^+\pi^+$. Eqn. A.1 becomes:

$$\sigma^N_{\pi\rightarrow D^+}(i)\mathrm{BR}(D^+ \rightarrow K^-\pi^+\pi^+) = \frac{N_{\substack{\pi\rightarrow D^+ \\ \rightarrow K\pi\pi}}(i)}{N_\pi(i)} \frac{A_i}{\rho_i N_A t_i}, \tag{A.2}$$

where:

- $\sigma^N_{\pi\rightarrow D^+}(i)$ is the *per nucleus* D^+ cross section for target i;
- $N_{\substack{\pi\rightarrow D^+ \\ \rightarrow K\pi\pi}}(i)$ is the *true* number of $D^+ \rightarrow K^-\pi^+\pi^+$ events from target i;
- $\mathrm{BR}(D^+ \rightarrow K^-\pi^+\pi^+)$ is the $D^+ \rightarrow K^-\pi^+\pi^+$ branching ratio.

We can rewrite this equation in a more useful form:

$$N_{\substack{\pi\rightarrow D^+ \\ \rightarrow K\pi\pi}}(i) = N_\pi(i)\frac{\rho_i N_A t_i}{A_i}\mathrm{BR}(D^+ \rightarrow K^-\pi^+\pi^+)\sigma^N_{\pi\rightarrow D^+}(i). \tag{A.3}$$

Since we need to know the number of pions and kaons incident on each target region, we define the following transmission coefficents:

$$T_x(i) \qquad \text{by} \qquad N_x(i) = N_x(0)T_x(i),$$

where:

- $N_x(0)$ is the number of incident x's at the upstream end of the target;
- $T_x(i)$ is easily calculated from the target parameters and the total cross section for the incident particle x. It is different for π's, K's, and p's since they all have different total cross sections:

$$\begin{aligned} \sigma^p_{inel} &\simeq 32\ mb \\ \sigma^{\pi^+}_{inel} &\simeq 21\ mb \\ \sigma^{K^+}_{inel} &\simeq 17\ mb \end{aligned}$$

Also,

$$N_x(0) = N_x R_x,$$

where:

- N_x is the true number of beam particles of type x which reach the beam tagging detectors (see Chapter 3);
- R_x is the fraction of beam of type x at the beam tagging point which reaches the target (some is lost in upstream interactions).

We cannot measure the true number of pions; instead we measure the number tagged by our beam tagging devices. Let us define a π' particle as having passed the pion identification cuts. Then the true number of pions, kaons, and protons in the π' sample is:

$$N_\pi^{true}(\pi') = N_{\pi'} P(\pi', \pi)$$

$$N_K^{true}(\pi') = N_{\pi'} P(\pi', K)$$

$$N_p^{true}(\pi') = N_{\pi'} P(\pi', p)$$

where:

- $N_{\pi'}$ is the number of particles that were tagged as pions;
- $P(\pi', \pi)$ is the probability that a particle tagged as a pion really was a pion;
- $P(\pi', K)$ is the probability that a particle tagged as a pion was really a kaon;
- $P(\pi', p)$ is the probability that a particle tagged as a pion was really a proton.

We can write the actual number of $D^+ \to K^-\pi^+\pi^+$ events from π' beam particles as follows:

$$\begin{aligned} N_{\substack{\pi' \to D^+ \\ \to K\pi\pi}}(i) &= N_{\substack{\pi \to D^+ \\ \to K\pi\pi}}(\pi', i) + N_{\substack{K \to D^+ \\ \to K\pi\pi}}(\pi', i) + N_{\substack{p \to D^+ \\ \to K\pi\pi}}(\pi', i) \\ &= \frac{\rho_i N_A t_i}{A_i} \mathrm{BR}(D^+ \to K^-\pi^+\pi^+) \{ N_\pi^{true}(\pi') R_\pi T_\pi(i) \sigma^N_{\pi \to D^+}(i) \quad \text{(A.4)} \\ &+ N_K^{true}(\pi') R_K T_K(i) \sigma^N_{K \to D^+}(i) + N_p^{true}(\pi') R_p T_p(i) \sigma^N_{p \to D^+}(i) \}, \end{aligned}$$

where:

- $N_{\substack{\pi \to D^+ \\ \to K\pi\pi}}(\pi', i)$ is the true number of $\pi \to D^+$ events in the π' sample, and so on for the true number of $K \to D^+$ events etc.

Now we note that the above is true for each *spill.* and that we must sum over all the spills in the run. To denote this, we use the superscript s for quantities which change from spill to spill. We thus rewrite Eqn.(A.4) as:

$$\begin{aligned} N^s_{\substack{\pi'-D^+ \\ -K\pi\pi}}(i) &= N^s_{\substack{\pi-D^+ \\ -K\pi\pi}}(\pi',i) + N^s_{\substack{K-D^+ \\ -K\pi\pi}}(\pi',i) + N^s_{\substack{p-D^+ \\ -K\pi\pi}}(\pi',i) \qquad \text{(A.5)} \\ &= \frac{\rho_i N_A t_i}{A_i}\mathrm{BR}(D^+\to K^-\pi^+\pi^+)N^s_{\pi'}\left\{P^s(\pi',\pi)R_\pi T_\pi(i)\sigma^N_{\pi-D^+}(i)\right. \\ &+ \left. P^s(\pi',K)R_K T_K(i)\sigma^N_{K-D^+}(i) + P^s(\pi',p)R_p T_p(i)\sigma^N_{p-D^+}(i)\right\}. \end{aligned}$$

Before proceeding, we note that the contamination of the identified pion sample by kaons and protons (given by $P^s(\pi',K)$ and $P^s(\pi',p)$) is very small. For the negative data, the kaon contamination is 3.4%, and the $\bar{p}$ contamination is 1.6%. For the positive data the kaon contamination is 0.05% and the proton contamination is 0.6%. (See Sec. A.2 for details on this.) The transmission and beam loss coefficients T are:

	Target region			
	1	2	3	4
T_π	0.999	0.996	0.993	0.991
T_K	0.999	0.997	0.994	0.992
T_p	0.998	0.994	0.989	0.986

while the R's are all $\simeq 0.99$.

To simplify the derivation, we note that the QCD prediction for the ratio of the proton to pion charm cross section is 1.1 [Nas 88], and the ratio for the kaon to pion charm cross section is 1.2 [Jed 91]. The proton and pion D cross sections have been measured by NA27 at a beam energy of 360 GeV, and found to be $15.5^{+8.2}_{-4.6}$ μb and 15.8 ± 2.7 μb respectively. The kaon to pion D_s cross section has been measured by E769 to be 1.2 ± 0.7 [Jed 91]. We therefore use a value of $1.1\sigma^N_{\pi\to D^+}(i)$ for $\sigma^N_{K\to D^+}(i)$ and $\sigma^N_{p\to D^+}(i)$, with errors of $\pm 0.5\sigma^N_{\pi\to D^+}(i)$. We justify this by noting that since the contamination of the pion sample is only 5%, even a difference in cross sections of 50% results in a 2.5% error on the result. Since this error is quite small compared to the statistical error, as well as to other systematic errors, a more detailed treatment of the correction is not warranted.

The effect of the contamination is absorbed into the factor F, given by:

$$\begin{aligned} F &= 1.06 \pm 0.03 \quad , \text{ Negative Data} \\ F &= 1.010 \pm 0.005 \quad , \text{ Postive Data.} \end{aligned}$$

With this definition, Eqn. A.5 simplifies to:

$$N^s_{\substack{\pi'-D^+ \\ -K\pi\pi}}(i) = \frac{\rho_i N_A t_i}{A_i}\mathrm{BR}(D^+\to K^-\pi^+\pi^+)FN^s_{\pi'}P^s(\pi',\pi)R_\pi T_\pi(i)\sigma^N_{\pi-D^+}(i), \quad \text{(A.6)}$$

with the appropriate F depending on whether the spill is in the negative or positive running period.

To proceed, we need the relationship for each spill between the true number of events tagged as pions, $N^s_{\substack{\pi'-D^+\\-K\pi\pi}}(i)$, and the reconstructed number, $n^s_{\substack{\pi'-D^+\\-K\pi\pi}}(i)$, . This is given by:

$$n^s_{\substack{\pi'-D^+\\-K\pi\pi}}(i) = N^s_{\substack{\pi'-D^+\\-K\pi\pi}}(i) LT^s \epsilon^s_{\pi'}(i), \tag{A.7}$$

where:

- $n^s_{\substack{\pi'-D^+\\-K\pi\pi}}(i)$ is the number of reconstructed $D^+ \rightarrow K^-\pi^+\pi^+$ events which came from beam particles tagged as pions:
- LT^s is the fraction of time the experiment was live during the spill:
- $\epsilon^s_{\pi'}(i)$ is the reconstruction + trigger efficiency for $D^+ \rightarrow K^-\pi^+\pi^+$ events from target i which were tagged as pions. Note that $\epsilon^s_{\pi'}(i)$ contains all the trigger effects, such as all prescale factors, the effect of the killer bit, and the actual trigger efficiency.

Combining Eqn.(A.7) with Eqn.(A.6) gives:

$$n^s_{\substack{\pi'-D^+\\-K\pi\pi}}(i) = \tag{A.8}$$
$$\frac{\rho_i N_A t_i}{A_i} \mathrm{BR}(D^+ \rightarrow K^-\pi^+\pi^+) F N^s_{\pi'} LT^s \epsilon^s_{\pi'}(i) P^s(\pi', \pi) R_\pi T_\pi(i) \sigma^N_{\pi-D^+}(i).$$

To proceed with the derivation, we split the efficiency term into three parts:

$$\epsilon^s_{\pi'}(i) = \varepsilon_{int}(ntrk) \varepsilon^s_{trg_{\pi'}}(p_{t715}) \varepsilon_{rec}(i). \tag{A.9}$$

The expressions in the brackets denote on which variable each efficiency depends. The first term is the interaction trigger efficiency, which depends solely on the number of charged tracks passing through the interaction scintillator. This efficiency was parameterized independently of spill number, as it was found that the trigger threshold did not change over the course of the experiment. The second term is the E_t trigger efficiency (measured relative to events which passed the interaction criterion). This term did change from spill to spill, as both the trigger prescalers and the trigger threshold were varied from run to run. The final term is the *reconstruction only* part, which is solely a function of the kinematics of the event. For more information on the triggers, see Sec. 5.2.

The spill dependent efficiency ($\varepsilon^s_{trg_{\pi'}}(p_{t715})$) was actually made up of the true trigger efficiencies for two independent sets of trigger logic which were used. Every trigger passed through either of two logic paths. One, which we will call E_{tK}, was the trigger for beam particles with positive DISC tags. The other, which we call simply E_t, was for non DISC-tagged beam particles which passed the E_{tSTD} or E_{tB} triggers. (The first is called E_{tK} simply because the DISC was designed primarily to tag kaons.) However, there were runs in which it was set to tag pions or protons. In a run where the DISC was set to tag pions, all tagged pions would satisfy the E_{tK} trigger. Hence we have tagged pion events which come from both the E_t (the majority) and E_{tK} (very few) triggers. To summarize:

$$\begin{aligned} \varepsilon^s_{trg_{\pi'}}(p_{t715}) &= \varepsilon^s_{E_t}(p_{t715}) \quad , \ (NODISC_\pi) \\ \varepsilon^s_{trg_{\pi'}}(p_{t715}) &= \varepsilon^s_{E_{tK}}(p_{t715}) \quad , \ (DISC_\pi), \end{aligned}$$

where $DISC_x$ means the DISC was set to tag particle type x, and $NODISC_x$ means it was set to tag something other than x.

To simplify the analysis, we remove all spills in which the DISC was set to tag pions. These only amount to $< 4\%$ of the pion sample, so the extra work of including them was avoided. We now sum over spills (explicitly showing what the DISC is set to tag) to get:

$$\begin{aligned} n^{\pi'-D^+}_{-K\pi\pi}(i) &= \sum_{\substack{spills \\ NODISC_\pi}} n^{s\ \pi'-D^+}_{-K\pi\pi}(i) \\ &= \frac{\rho_i N_A t_i}{A_i} \mathrm{BR}(D^+ \to K^-\pi^+\pi^+) F \varepsilon_{int}(ntrk) \varepsilon_{rec}(i) \\ &\quad \left\{ \sum_{\substack{spills \\ NODISC_\pi}} (N^s_{\pi'} LT^s P^s(\pi',\pi) \varepsilon^s_{trg_{\pi'}}(p_{t715})) R_\pi T_\pi(i) \sigma^N_{\pi \to D^+}(i) \right\}. \end{aligned} \tag{A.10}$$

The problem with using the above equation is that it is not possible (or desirable) to have trigger efficiency curves for every spill. We thus replace $\varepsilon^s_{trg_{\pi'}}(p_{t715})$ with $\varepsilon_{trg_{\pi'}}(p_{t715})$, where $\varepsilon_{trg_{\pi'}}(p_{t715})$ is defined such that:

$$\sum_{\substack{spills \\ NODISC_\pi}} (N^s_{\pi'} LT^s P^s(\pi',\pi) \varepsilon^s_{trg_{\pi'}}(p_{t715})) = \varepsilon_{trg_{\pi'}}(p_{t715}) \sum_{\substack{spills \\ NODISC_\pi}} (N^s_{\pi'} LT^s P^s(\pi',\pi)).$$

That is, we must generate an efficiency curve $\varepsilon_{trg_{\pi'}}(p_{t715})$, which is determined from the spills where the DISC was not tagging pions, and *weighted according to* $N^s_{\pi'} LT^s P^s(\pi',\pi)$. The details of this are discussed in Sec. (A.3). Note that leaving out the spills in

which the DISC was tagging pions saves us from having to generate another curve for pions which came in on the E_{tK} trigger.

We now recombine the trigger and reconstruction efficiencies into one overall Monte Carlo efficiency: $\epsilon_{\pi'}(i) = \varepsilon_{int}(ntrk)\varepsilon_{trg_{\pi'}}(p_{t715})\varepsilon_{rec}(i)$. The procedure used to determine this efficiency is discussed in Sec. A.3.

Eqn.(A.10) now becomes:

$$n_{\substack{\pi'-D^+ \\ -K\pi\pi}}(i) = \frac{\rho_i N_A t_i}{A_i}\mathrm{BR}(D^+ \to K^-\pi^+\pi^+)F\epsilon_{\pi'}(i) \left\{ \sum_{\substack{spills \\ NODISC_\pi}} N^s_{\pi'} P^s(\pi',\pi) R_\pi T_\pi(i) \sigma^N_{\pi-D^+}(i) \right\}. \tag{A.11}$$

Let us call:

$$\begin{aligned} Norm(\pi',\pi) &= \sum_{\substack{spills \\ NODISC_\pi}} N^s_{\pi'} LT^s P^s(\pi',\pi) \\ Norm(\pi',K) &= \sum_{\substack{spills \\ NODISC_\pi}} N^s_{\pi'} LT^s P^s(\pi',K) \\ Norm(\pi',p) &= \sum_{\substack{spills \\ NODISC_\pi}} N^s_{\pi'} LT^s P^s(\pi',p), \end{aligned}$$

so that Eqn.(A.11) becomes:

$$n_{\substack{\pi'-D^+ \\ -K\pi\pi}}(i) = \frac{\rho_i N_A t_i}{A_i}\mathrm{BR}(D^+ \to K^-\pi^+\pi^+)F\epsilon_{\pi'}(i)Norm(\pi',\pi)R_\pi T_\pi(i)\sigma^N_{\pi-D^+}(i).$$

Isolating the cross section now gives:

$$\sigma^N_{\pi\to D^+}(i) = \frac{1}{\mathrm{BR}(D^+ \to K^-\pi^+\pi^+)} \frac{A_i}{\rho_i N_A t_i} \frac{F}{R_\pi T_\pi(i)} \frac{n_{\substack{\pi'-D^+ \\ -K\pi\pi}}(i)}{\epsilon_{\pi'}(i) Norm(\pi',\pi)}. \tag{A.12}$$

A.2 Determining the Norm values

In this section we detail how the Norm values were actually determined. The description follows [Jed 89]. Define f_{π^-}, f_{K^-}, and f_{p^-} to be the *a priori* fractions of pions, kaons and protons in the negative beam, and $\varepsilon^s_{DISC_\pi}, \varepsilon^s_{DISC_K}, \varepsilon^s_{DISC_p}$ to be the DISC tagging efficiencies for each particle type in a given spill. The fraction of pions, kaons, and protons in the non-DISC tagged part of the beam is then:

$$f'_{\pi^-} = \frac{(1-\varepsilon^s_{DISC_\pi})f_{\pi^-}}{S^-}$$

$$f'_{K^-} = \frac{(1-\varepsilon^s_{DISC_K})f_{K^-}}{S^-}$$
$$f'_{p^-} = \frac{(1-\varepsilon^s_{DISC_p})f_{p^-}}{S^-},$$

where $S^- = 1 - \varepsilon^s_{DISC_\pi} f_{\pi^-} - \varepsilon^s_{DISC_K} f_{K^-} - \varepsilon^s_{DISC_p} f_{p^-}$.

Similar relations hold for the positive beam.

There were two basic scalers used in the normalisation, namely:

- $TRDGB$, which counted the number of usable beam particles.
- $FOLD4$, which counted the number of TRDGB which also had positive DISC tags.

For convenience we define $\overline{FOLD4}$ as $TRDGB - FOLD4$, i.e. the number of non-DISC tagged beam particles.

A.2.1 The Pion Normalisation

We wish to calculate the three quantities:

$$Norm(\pi', \pi) = \sum_{\substack{spills \\ NODISC_\pi}} N^s_{\pi'} LT^s P^s(\pi', \pi)$$
$$Norm(\pi', K) = \sum_{\substack{spills \\ NODISC_\pi}} N^s_{\pi'} LT^s P^s(\pi', K)$$
$$Norm(\pi', p) = \sum_{\substack{spills \\ NODISC_\pi}} N^s_{\pi'} LT^s P^s(\pi', p)$$

Now, $N^s_{\pi'}$ is simply the number of non-DISC tagged beam particles in a given spill, i.e. $\overline{FOLD4}$ (recall we only consider spills in which the DISC is set to tag kaons). The livetime LT^s is obtained from two other scalers (called INT_PS and INT_PS2).

For negative beam, anything which is not tagged as a kaon is called a pion (since no TRD information was present). Hence the probability that a non-DISC tagged particle is in fact a pion ($P^s(\pi', \pi)$) is simply f'_{π^-} for negative beam (similarly for kaons and $\bar{p}$'s), and so for negative beam:

$$Norm(\pi', \pi) = \sum_{\substack{spills \\ NODISC_\pi}} \overline{FOLD4^s} LT^s f'_{\pi^-}$$
$$Norm(\pi', K) = \sum_{\substack{spills \\ NODISC_\pi}} \overline{FOLD4^s} LT^s f'_{K^-}$$
$$Norm(\pi', p) = \sum_{\substack{spills \\ NODISC_\pi}} \overline{FOLD4^s} LT^s f'_{p^-}.$$

The situation is more complicated for positive beam due to the presence of the TRD, and the large proton component of the beam. For positive beam, the number of particles tagged as pions is:

$$N^s_{\pi'} = \overline{FOLD4^s} LT^s f'_{\pi^+} \varepsilon^{TRD}_{\pi},$$

where ε^{TRD}_{π} is the TRD tagging efficiency for pions.

Let C^{TRD}_{π} be the contamination of the TRD-tagged pion signal by kaons and protons. This number was determined on a run-by-run basis from events on tape. However, because the total cross section is different for pions, kaons, and protons, the contamination in the *beam* is slightly different. We can show ([Jed 89]) that the fraction of the kaons and protons which contaminate the tagged pion beam is $0.97 C^{TRD}_{\pi} \varepsilon^{TRD}_{\pi}$. Thus for positive beam we have:

$$\begin{aligned}
Norm(\pi', K) &= \sum_{\substack{spills \\ NODISC_{\pi}}} \overline{FOLD4^s} LT^s 0.97 f'_{K^+} \varepsilon^{TRD}_{\pi} \\
Norm(\pi', p) &= \sum_{\substack{spills \\ NODISC_{\pi}}} \overline{FOLD4^s} LT^s 0.97 f'_{p^+} \varepsilon^{TRD}_{\pi} \\
Norm(\pi', \pi) &= \sum_{\substack{spills \\ NODISC_{\pi}}} \overline{FOLD4^s} LT^s \varepsilon^{TRD}_{\pi} (f'_{\pi^+} - 0.97(f'_{K^+} + f'_{p^+}) C^{TRD}_{\pi}).
\end{aligned}$$

After summing the appropriate scalers, the values of the contaminations $Norm(\pi', K)$ and $Norm(\pi', p)$ for negative data were found to be:

$$\begin{aligned}
Norm(\pi', K) &= 0.034 Norm(\pi', \pi) \\
Norm(\pi', p) &= 0.016 Norm(\pi', \pi),
\end{aligned}$$

and for positive data:

$$\begin{aligned}
Norm(\pi', K) &= 0.0005 Norm(\pi', \pi) \\
Norm(\pi', p) &= 0.006 Norm(\pi', \pi).
\end{aligned}$$

A.3 The Trigger Efficiency Curves

The E_t trigger efficiency curves were obtained by using Interaction trigger events from the entire data set. Recall that we need to generate:

$$\sum_{\substack{spills \\ NODISC_{\pi}}} N^s_{\pi'} LT^s P^s(\pi', \pi) \varepsilon^s_{trg_{\pi'}}(p_{t715}) = \varepsilon_{trg_{\pi'}}(p_{t715}) \sum_{\substack{spills \\ NODISC_{\pi}}} N^s_{\pi'} LT^s P^s(\pi', \pi).$$

For any given spill, the efficiency curve $\varepsilon^s_{trg_{\pi'}}(p_{t715})$ is obtained from two histograms:

- A: The p_{t^*15} distribution for Interaction events:
- B: The p_{t^*15} distribution for Interaction events which also passed the E_{tSTD} or E_{tB} triggers.

The efficiency curve is then given by dividing B/A.

To get the proper weighting between spills, we note that the number of interaction events on tape from any spill is proportional to $N^s_{\pi'} LT^s / PS_{int}$, where PS_{int} is the prescaler applied to interaction triggers. Also, for the runs we are interested in, the factor $P^s(\pi', \pi)$ varies from about .90 to .95, so we can approximate it as a constant, and take it out of the sum, leaving:

$$\sum_{\substack{\text{spills} \\ NODISC_\pi}} N^s_{\pi'} LT^s \varepsilon^s_{trg_{\pi'}}(p_{t^*15}) = \varepsilon_{trg_{\pi'}}(p_{t^*15}) \sum_{\substack{\text{spills} \\ NODISC_\pi}} N^s_{\pi'} LT^s. \tag{A.13}$$

Hence, if we make histograms A and B from all interaction events over the entire data set, but weight each event by the interaction prescale for that spill, and then divide the two as above, we get the required efficiency curve, $\varepsilon_{trg_{\pi'}}(p_{t^*15})$.

The interaction efficiency curve was generated from beam track runs. These were special runs whose trigger was simply that a beam particle passed through the detector. Events with an interaction were selected by demanding that an interaction vertex be found in the target region. The Interaction scintillator signal was digitized by an ADC. For each value of *nsmdtrk* (the number of tracks with support in the silicon system) the fraction of events with an ADC count above the standard threshold value was determined, thus giving an efficiency.

References

[Agu 84] M. Aguilar-Benitez *et al.* (LEBC-EHS collaboration), Physics Letters **135B**, 237, (1984).

[Agu 86] M. Aguilar-Benitez *et al.*, (LEBC-EHS collaboration), Zeitschrift für Physik **C31**, 491, (1986).

[Agu 88] M. Aguilar-Benitez *et al.*, (LEBC-EHS collaboration), Zeitschrift für Physik **C40**, 321, (1988).

[Aih 84] H. Aihara *et al.*, Phys. Rev. Lett. **53**, 2465, (1984).

[Alt 77] G. Altarelli and G. Parisi, Nuclear Physics **B126**, 298, (1977).

[Alb 84] H. Albrecht *et al.* (ARGUS collaboration), Physics Letters **146B**, 111, (1984).

[Amm 80] R. Ammar *et al.*, Physics Letters **183B**, 110, (1980).

[And 83] B. Anderson, G. Gustafson, G. Ingelman and T. Sjöstrand, Physics Reports **97**, 32, (1983).

[And 87] B. Anderson, G. Gustafson, and B. Nilsson-Almqvist, *A High Energy String Dynamics Model for Hadronic Interactions*, University of Lund, LU-TP-87-6, (1987).

[And 33] C. D. Anderson, Phys. Rev. **43**, 491, (1933).

[Ant 78] Y. M. Antipov *et al.*, Physics Letters **76B**, 235, (1978).

[App 86] J. Appel, P. Mantsch, M. Streetman, R. Robertson, Nucl. Inst. Meth. **A243**, 361, (1986).

[Ash 88] J. Ashman *et al.* (EM Collaboration), Physics Letters **B202**, 603, (1988).

[Aub 74] J. Aubert *et al.*, Phys. Rev. Lett. **33**, 1404, (1974).

[Aug 74] J. Augustin *et al.*, Phys. Rev. Lett. **33**, 1406, (1974).

[Bab 78] J. Babcock, D. Sivers, and S. Wolfram, Phys. Rev. **D18**, 162, (1978).

[Bad 83] J. Badier *et al.* (NA3 Collaboration). Zeitschrift für Physik **C20**. 101. (1983).

[Bar 79] D. P. Barber *et al.* (MARK J Collaboration). Phys. Rev. Lett. **43**, 830. (1979).

[Bar 87] V. Barger and R. Phillips, *Collider Physics*, Addison-Wesley, California (1987).

[Bar 88] S. Barlag *et al.* (ACCMOR Collaboration), Zeitschrift für Physik **C39**. 451. (1988).

[Bar 91] S. Barlag *et al.* (ACCMOR Collaboration). Zeitschrift für Physik **C49**. 555. (1991).

[Bar 79a] W. Bartel *et al.* (JADE Collaboration), Physics Letters **91B**. 142. (1979).

[Bar 83] D. S. Barton *et al.*. Phys. Rev. **D27**. 2580. (1983).

[Ben 73] M. Benot. J. Litt. R. Meunier. *A Manual for the CERN/NAL High-Resolution DISC Cerenkov Counter* (1973).

[Ber 88] E. Berger, *Heavy Flavor Production*, ANL-HEP-CP-88-26 (1988).

[Ber 79] C. Berger *et al.* (PLUTO Collaboration), Physics Letters **86B**. 418. (1979).

[Bjo 64] B. J. Bjorken and S. L. Glashow. Physics Letters **11**. 255. (1964).

[Bjo 69] B. J. Bjorken and E. A. Paschos, Phys. Rev. **185**, 1975. (1969).

[Bra 79] R. Brandelik *et al.* (TASSO Collaboration), Physics Letters **86B**, 243, (1979).

[Bro 87] S. Brodsky, J. Gunion, and D. Soper, Phys. Rev. **D36**, 2710, (1987).

[Bro 88] T. E. Browder, *A Study of $D^0 - \bar{D}^0$ Mixing*, Ph.D. Thesis, University of California, Santa Barbara, (1988).

[Bur 76] E. Burhop *et al.*, Physics Letters **65B**, 299, (1976).

[Cab 63] N. Cabbibo, Phys. Rev. Lett. **10**. 531, (1963).

[Car 79] A. S. Carroll *et al.*, Physics Letters **80B**. 319, (1979).

[Caz 75] E. G. Cazzioli *et al.*, Phys. Rev. Lett. **34**, 1125, (1975).

[Cha 32] J. Chadwick, Nature **129**, 312, (1932).

[Che 83] A. Chen *et al.*, Phys. Rev. Lett. **51**, 634, (1983).

[Che 84] T. Cheng and L. Li, *Gauge Theory of Elementary Particle Physics*, Clarendon Press, Oxford (1984).

[Clo 88] F. Close and R. Roberts, Physics Letters **213B**, 91, (1988).

[Clo 89] F. Close, J. Qiu, and R. Roberts. Phys. Rev. **D40**, 2820, (1989).

[Cob 87] H. Cobbaert *et al.* (WA78 collaboration), Physics Letters **191B**, 456, (1987).

[Cob 88] H. Cobbaert *et al.* (WA78 collaboration), Physics Letters **206B**, 546, (1988).

[Col 73] S. Coleman and D. J. Gross, Phys. Rev. Lett. **31**, 851, (1973).

[Col 84] J. C. Collins, D. E. Soper, and G. Sterman, Physics Letters **134B**, 263, (1984).

[Col 86] J. C. Collins, D. E. Soper, and G. Sterman, Nuclear Physics **B263**, 37, (1986).

[Cor 82] M. J. Corden *et al.*, Physics Letters **110B**, 415, (1982).

[Cow 53] C. L. Cowan and F. Reines, Phys. Rev. **92**, 830, (1953).

[Dan 62] G. Danby, J-M. Gaillard, K. Goulianos, L. M. Lederman, N. Mistry, M. Schwartz, and J. Steinberger, Phys. Rev. Lett. **9**, 36, (1962).

[Dri 79] D. Drijard *et al.*, Physics Letters **81B**, 250, (1979).

[Duf 85] M. E. Duffy *et al.*, Phys. Rev. Lett. **55**, 1816, (1985).

[Duf 86] M. E. Duffy *et al.*, Phys. Rev. Lett. **57**, 1522, (1986).

[Duk 84] D. W. Duke and J. F. Owens, Phys. Rev. **D30**, 49, (1984).

[Eic 84] Eichten, Hinchliffe, Lane, and Quigg, Rev. Mod Phys. **56**, 579, (1984).

[Ell 87] R. K. Ellis, C. Quigg , FERMILAB Report FN-445 (1989).

[Ell 89] R. K. Ellis, *The theory of heavy flavour production*, FERMILAB-Conf-89/168-T (1989).

[Ell 90] R. K. Ellis, Personal Communication.

[Fel 77] G. J. Feldman *et al.* Phys. Rev. Lett. **38**, 1313, (1977).

[Fey 72] R. P. Feynman, *Photon-Hadron Interactions*, Benjamin, New York, (1972).

[Fox 74] D. J. Fox *et al.* Phys. Rev. Lett. **33**, 1504, (1974).

[Fri 73] H. Fritzsch, M. Gell-Mann and H. Leutwyler, Physics Letters **47B**, 365, (1973).

[Gel 64] M. Gell-Mann, Physics Letters **8**, 214, (1964).

[Gla 70] S. L. Glashow, J. Iliopoulos and L. Maiani, Phys. Rev. **D2**, 1285, (1970).

[Gol 76] G. Goldhaber *et al.* Phys. Rev. Lett. **37**, 255, (1976).

[Gol 77] G. Goldhaber *et al.* Physics Letters **69B**, 503, (1977).

[Gro 73] D. Gross and F. Wilczek, Phys. Rev. Lett. **30**, 1343, (1973).

[Her 77] S. W. Herb *et al.* Phys. Rev. Lett. **39**, 252, (1977).

[Inn 77] W. R. Innes *et al.* Phys. Rev. Lett. **39**, 1240, (1977).

[Jac 75] J. D. Jackson, *Classical Electrodynamics*, John Wiley and Sons, New York, (1975).

[Jed 89] R. Jedicke, *Beam Identification*, E769 Internal Memo, (1989).

[Jed 91] R. Jedicke, *Flavour Dependence of Hadroproduced Charm-Strange Mesons*, Ph.D. Thesis, University of Toronto, (1991).

[Kem 80] J. Kemmer, *et al.*, Nucl. Inst. Meth. **169**, 499, (1980).

[Lat 47] C. M. G. Lattes, H. Muirhead, C. F. Powell, and G. P. Occhialini, Nature **159**, 694, (1947).

[Men 86] S. R. Menary, *A Study of the Transverse Momentum Distributions of Photoproduced Charged and Neutral D Mesons*, M.Sc. Thesis, University of Toronto. (1986).

[Men 89] S. R. Menary, *Observation of Excited Charmed Mesons*, Ph.D. Thesis, University of Toronto, (1989).

[Nas 88] P. Nason, S. Dawson, and R. K. Ellis. Nuclear Physics **B303**, 607, (1988).

[Nas 89] P. Nason, S. Dawson, and R. K. Ellis, Nuclear Physics **B327**, 49, (1989).

[Owe 84] J. F. Owens. Phys. Rev. **D30**, 943, (1984).

[Per 75] M. L. Perl *et al.*. Phys. Rev. Lett. **35**, 1489. (1975).

[Per 76] I. Peruzzi *et al.*. Phys. Rev. Lett. **37**, 569. (1976).

[PDG 90] Particle Data Group, Review of Particle Properties Physics Letters **239B**, 1, (1990).

[Raa 87] J. Raab. *Lifetime Measurements of the Three Charmed Pseudoscalar D-Mesons*, Ph.D. Thesis, University of California, Santa Barbara, (1987).

[Rit 83] J. L. Ritchie *et al.*, Physics Letters **126B**, 499. (1983).

[Rit 84] J. L. Ritchie *et al.*, Physics Letters **138B**, 213, (1984).

[Sli 90] K. Sliwa. (CDF Collaboration), *Proceedings of the XXVth Rencontre de Moriond*, Les Arcs, 1990, edited by J. Tran Thanh Vân (Editions Frontieres, France, 1990), pg. 459.

[SL 72] J. I. Friedman and H. W. Kendall, Ann. Rev. Nucl. Sci. **22**, 203, (1972)

[Str 37] J. C. Street and E. C. Stevenson, Phys. Rev. **52**, 1003, (1937).

[Sum 84] D. Summers, *A Study of the Decay $D^0 \to K^-\pi^+\pi^0$ in High Energy Photoproduction*, Ph.D. Thesis, University of California, Santa Barbara, (1984).

[Wei 73] S. Weinberg, Phys. Rev. Lett. **31**, 494, (1973).

[Wil 64] K. Wilson, *On Products of Quantum Field Operators at Short Distances* (Cornell report), 1964.

[Zwe 64] G. Zweig, CERN Report 8182/TH.401